UNIVERSITY OF CALIFORNIA

Santa Barbara

The MicroHammer: Investigating Cellular Response to Impact with a Microfluidic MEMS Device

A dissertation submitted in partial satisfaction

of the requirements for the degree

Doctor of Philosophy

in Mechanical Engineering

by

Luke H.C. Patterson

Committee in charge:

Professor Kimberly L. Foster, Chair

Professor Adele M. Doyle

Professor Kenneth S. Kosik

Professor Carl Meinhart

Professor Megan T. Valentine

September 2020

The dissertation of Luke H.C. Patterson is approved.

Adele M. Doyle

Kenneth S. Kosik

Carl D. Meinhart

Megan T. Valentine

Kimberly L. Foster, Committee Chair

August 2020

The μHammer: Investigating Cellular Response to Impact

with a Microfluidic MEMS Device

by

Luke H.C. Patterson

Acknowledgments

To fully acknowledge the people who have contributed to this work, it would take another document perhaps even longer than this one. In the interest of brevity, I will constrain my comments to a more reasonable length, but know that the depths of my gratitude extend far beyond what I can convey in this space.

First, I must thank Professor Kimberly Foster, who was willing to apply the breadth of her expertise in microelectromechanical systems to pursue innovation in the field of biomedical engineering in alignment with my own interests. From the first day I joined her research group, she has provided unwavering support and encouragement through the hills and valleys of my graduate studies and personal life. I would also like to thank the members of the Foster, Doyle, and Saleh lab groups for providing a sounding board for new ideas, a sanity check during times of stress, and most of all for making me look forward to coming to work each day. Professors Adele Doyle and Megan Valentine both went above and beyond to enrich my time at UCSB, encouraging the pursuit of excellence and providing the tools to achieve it. They were closely involved in the details of this project from its early days, playing an invaluable role in guiding the direction of this work as well as my development as a scientist. I would also like to thank Professors Carl Meinhart and Kenneth Kosik, who have both been a trustworthy source of guidance and information to help maximize the potential of this project.

My collaborators deserve special acknowledgment. Jennifer Walker elevated the foundational work of this project to new heights, providing the tenacity necessary to work with cells on a daily basis while developing new experimental protocols. My colleagues at Owl biomedical not only provided the expertise and resources that made this project possible, but also were gracious hosts and an overall pleasure to work with.

I would also like to thank the faculty, students, and staff of the Mechanical Engineering Department, particularly Laura Reynolds, Julie Dunson, Josh Johnson, and Dave Bothman, who patiently endured my endless questions and helped me navigate the daily challenges of my time at UCSB.

My friends, both in Santa Barbara and elsewhere, have helped to keep me grounded and have provided a sense of perspective, all while bringing a depth and richness to my daily life. My family, whether Patterson, Lockwood, Baik, Agahi, Appel, Hayward, or Formo have selflessly supported me from the very beginning. In particular, my parents were instrumental in developing my passions in both engineering and medicine, continually inspiring me to pursue innovation across both fields.

Finally, I would like to thank my wife, Casey, for walking alongside me throughout this journey. She believed in me even when I didn't believe in myself, and was a bottomless source of strength, love, and hope that enabled me to persevere through the end of this endeavor. In the words of John Polkinghorne, "hope is much more than a mood, it involves a commitment to action. Its moral character implies that what we hope for should be what we are prepared to work for and so bring about, as far as that power lies in us" [1]. In the end, I am grateful to each individual listed above as well as countless others who empowered my hope to restore health in the human body through engineering, and who ultimately made this work possible as I pursue that goal.

Vita of Luke H.C. Patterson

Research Interests

Biomedical device development, biomechanics, microelectromechanical systems, microfluidics, neurotechnology, traumatic brain injury

Education

University of California, Santa Barbara
Ph.D. in Mechanical Engineering, 2014 – 2020

- Graduate Emphasis in Bioengineering
- Graduate Division Doctoral Scholar's Fellowship
- Mechanical Engineering Department Merit Fellowship

Westmont College, Santa Barbara, CA
B.S. in Engineering Physics, 2010 – 2014

- Faculty Scholarship Award for highest cumulative GPA in graduating class
- Engineering and Physics Department Graduate of the Year

Selected Publications

Luke H.C. Patterson, Jennifer L. Walker, Mark A. Naivar, Evelyn Rodriguez-Mesa, Mehran R. Hoonejani, Kevin Shields, John S. Foster, Adele M. Doyle, Megan T. Valentine, Kimberly L. Foster, " Inertial flow focusing: a case study in optimizing cellular trajectory through a microfluidic MEMS device for timing-critical applications," *Biomed Microdevices*, vol. 22, no. 3, pp. 1-12, 2020, DOI: 10.1007/s10544-020-00508-1

Jennifer L. Walker, **Luke H.C. Patterson**, Evelyn Rodriguez-Mesa, Kevin Shields, John S. Foster, Megan T. Valentine, Adele M. Doyle, Kimberly L. Foster, "Controlled Single-Cell Compression With a High-Throughput MEMS Actuator," *J Microelectromech Syst*, Advance online publication, 2020, DOI: 10.1109/JMEMS.2020.3005514

Luke H.C. Patterson, Jennifer L. Walker, Evelyn Rodriguez-Mesa, Kevin Shields, John S. Foster, Megan T. Valentine, Adele M. Doyle, Kimberly L. Foster, "Investigating Cellular Response to Impact with a Microfluidic MEMS Device," *J Microelectromech Syst,* vol. 29, no. 1, pp. 14-24, 2019, DOI: 10.1109/JMEMS.2019.2948895

Luke H.C. Patterson, Michael A. Everest, Kenneth A. Kihlstrom, "Balanced polarimeter: A cost-effective approach for measuring the polarization of light," *Am J Phys*, vol 83, no. 1, pp. 91-94, 2015, DOI: 10.1119/1.4896747

Selected Conference Presentations

Luke H.C. Patterson, Jennifer L. Walker, Evelyn Rodriguez-Mesa, Kevin Shields, John S. Foster, Megan T. Valentine, Adele M. Doyle, Kimberly L. Foster, "Investigating Cellular Response to Impact with a High Throughput Microfluidic MEMS Device," Solid-State Sensors, Actuators, and Microsystems Workshop, Hilton Head, SC, USA, June 2018.

Professional Experience

University of California, Santa Barbara
Graduate Research Assistant, 2015 – 2020

TrueVision 3D Surgical, Santa Barbara, CA
Engineering Intern, 2013 – 2015

Westmont College, Santa Barbara, CA
Research Assistant, 2012

Teaching Experience

University of California, Santa Barbara
Teaching Assistant, 2014 – 2019
- Mechanical Engineering Laboratory
- Strength of Materials
- Tissue and Systems Bioengineering
- Introduction to Machine Shop

Westmont College, Santa Barbara, CA
Teaching Assistant, 2012 – 2014
- Electricity and Magnetism
- Mechanics
- Physical Science
- Computational Physics

Selected Service

Biotechnology Industry Showcase, Santa Barbara, CA
Co-organizer, 2019

Bridge to Doctorate Fellowship Program, Santa Barbara, CA
Peer Mentor, 2017 – 2018

VIBRANT Research Experiences for Undergraduates, Santa Barbara, CA
Research Mentor, 2016

Abstract

The MicroHammer: Investigating Cellular Response to Impact
with a Microfluidic MEMS Device

by

Luke H.C. Patterson

Although high strain and strain-rate impacts to the human body have been the subject of substantial research at both the systemic and tissue levels, little is known about the cell-level ramifications of such assaults. This is largely due to the lack of high throughput, dynamic compression devices capable of simulating such traumatic loading conditions on individual cells. Understanding the mechanical response to impact on the cellular level is important, since it can elucidate the fundamental mechanisms of damage following impact to vulnerable tissue like the brain and cartilage, providing a window into potential targets for therapy. To fill this gap, my collaborators and I have developed and characterized a high speed, high actuation force, magnetically driven MEMS chip to apply compression to biological cells with an unprecedented combination of strain (10% to 90%), strain rate (30,000 to 200,000 s^{-1}), and throughput (10,000 to 1,000,000 cells/experiment). To demonstrate the cell-impact capabilities of the μHammer, we applied biologically relevant strains and strain rates to human leukemic K562 cells and then monitored their viability for up to 8 days. We observed

significantly repressed proliferation of the hit cells compared to both unperturbed and sham-hit control cells, accompanied by minimal cell death. This indicates success in applying cellular damage without compromising the overall viability of the population.

Once we validated the μHammer's ability to impact cells, we sought to fully leverage the high-throughput capabilities of the device by optimizing the experimental conditions of the fluid and cells (or other particles) flowing through it. Parameters such as flow velocity and particle size are known to affect the trajectories of particles in microfluidic systems and have been studied extensively, but the effects of temperature and buffer viscosity are not as well understood. To explore the effects of these parameters on the performance of the μHammer, we first tracked the velocity of polystyrene beads through the device and then visualized the impact of these beads. Through these assays, we find that the timing of our device is sensitive to changes in the ratio of inertial forces to viscous forces that particles experience while traveling through the μHammer. This sensitivity provides a set of parameters that can serve as a robust framework for optimizing the performance of microfluidic devices under various experimental conditions. Using this framework, we achieved an effective throughput over 360 particles/s with the μHammer and proposed geometric redesigns which could further improve device performance in future experiments. In the end, the impact parameters applied by the μHammer to each of these particles align with those experienced by individual cells during traumatic impacts in the brain and cartilage, allowing us to conclude that this device is well-suited to study the subtle effects of impact on large populations of inherently heterogeneous cells.

Some of the content in the abstract and Chapters 1, 3, 4, 5, and 7 is adapted from: Luke H.C. Patterson et al., "Investigating Cellular Response to Impact with a Microfluidic MEMS Device," *J Microelectromech Syst,* vol. 29, no. 1, pp. 14-24, 2019, DOI: 10.1109/JMEMS.2019.2948895.

Some of the content in the abstract and Chapters 4, 6, and 7 is adapted by permission from: Springer Nature, *Biomed Microdevices*, "Inertial flow focusing: a case study in optimizing cellular trajectory through a microfluidic MEMS device for timing-critical applications," Luke H.C. Patterson et al.,

Table of Contents

Chapter 1. Introduction

From an engineering perspective, the human body is a wonderfully intricate machine, able to sense and respond to chemical and mechanical cues across a variety of different length scales. This is the case even down to the cellular level, since at their most basic level, cells are transducers – entities that receive signals from their environment and transform them into actions that alter the states of the cells and their surroundings. One fundamental signal sensed by all cells is mechanical force. Force input can lead to gene expression cascades and other responses such as protein synthesis, proliferation, and movement that alter the cellular state on a temporary or even permanent basis [2-5]. For example, gene expression cascades can become activated by transmembrane proteins such as integrins that transmit both external and internal forces, while mechanically-controlled ion channels can regulate the flow of ions across cell membranes [2, 6, 7]. On a functional level, the link between mechanical stimulation and the differentiation, expression, and proliferation of stem cells has been extensively documented, with inputs as subtle as substrate stiffness having a dramatic effect on stem cell behavior [8-10]. Mechanical stimulation is also sensed by differentiated cells such as osteocytes, serving as a determinant of the bone remodeling process which is vital to maintaining skeletal integrity over time [11, 12]. Overall, the effects of mechanical force have been explored on numerous cell types subjected to a variety of loading conditions including dynamic compression, cyclic tensile loading, and subsonic vibration [5, 13-19]. Yet although such experiments are common on cells in tissue and groups of cells embedded in synthetic matrices, they are rarely performed on individual cells *in vitro.* Batch processes that apply force to populations of cells, whether in 3D matrices or in monolayers [13-16, 20, 21], make

it difficult to precisely control the loading conditions applied to each cell and to isolate the force response from other contributing factors. This isolation is crucial to investigating how mechanical deformation alone affects both suspended and adherent cells, which once understood can shed light on the role of more complicated interactions between cells and their surroundings when subjected to force.

The experimental gap in single cell data is especially apparent in the realm of high strain and strain-rate compressions resulting from external impacts, a pernicious cause of injury to which the brain and the joints are particularly susceptible. Traumatic brain injury (TBI) is the leading cause of death and disability in children and young adults (Table 1.1), and is estimated to have resulted in permanent disability in over 5 million individuals in the United States [22, 23]. The incidence of traumatic joint injuries, on the other hand, is not well documented, but it is estimated that 10% to 15% of all cases of osteoarthritis (OA; the leading cause of disability in the United States) are caused by traumatic joint injuries [24-26]. Both brain and joint injuries can be sustained through either acute or repeated physical impacts resulting from traumatic events such as falls, high-impact sports, or traffic accidents. Additionally, TBI can also occur in response to pressure waves resulting from percussive blasts that result from explosions, most commonly encountered in the military. Following the initial mechanical shearing, stretching, and compression from a traumatic injury that results in material breakdown, a variety of physiological and biochemical responses take place on the order of milliseconds to months afterwards that can exacerbate the damage caused by the initial injury and lead to permanently compromised tissue performance [27]. Unfortunately, the pathways and mechanisms by which these detrimental effects occur on the microscale are not well understood [28, 29], since little research has been done in these systems involving dynamic

Table 1.1: Causes and ramifications of traumatic brain and joint injuries

	Traumatic Brain Injury	Traumatic Joint Injury
Loading types [23, 25, 26, 28]	- Acute or repeated physical impact through falls, traffic accidents, sports, and other traumatic events - Explosive blast loading in the military	- Mechanical loading over time through obesity and high-impact occupations - Acute physical impact through sports and other traumatic events
Clinical ramifications [28, 30-33]	- Concussion - Contusion - Diffuse Axonal Injury (DAI) - Cerebrovascular injury - Neurodegeneration - Chronic Traumatic Encephalopathy	- Ligament rupture - Intra-articular fracture - Cartilage degeneration - Chondropenia - Post-traumatic osteoarthritis
Societal impact [22, 23, 25, 26]	- TBI is the leading cause of death and disability in children and young adults in the US, and is a contributing factor to a third of all injury related deaths - 1% of US population suffers a TBI each year - 5-10% of TBI results in permanent disability	- OA is the most common cause of disability in the US, and is a leading cause of hospitalization - 10% of US population diagnosed with OA - 10-15% of OA caused by traumatic impacts
Functional impact [34-36]	- Dizziness / loss of balance - Seizures - Sensory / speech deficits - Memory / concentration problems	- Joint pain - Stiffness - Swelling - Loss of mobility
Immediate structural effects[a] (ms – s) [28, 30, 33]	- Blood-brain barrier breakdown - DAI - Microvascular injury / hemorrhage	- Collagen rupture - Matrix breakdown
Short-term cellular / tissue effects (s – hr) [23, 33, 37-40]	- Neuroinflammation - Oxidative stress - Cell death - Genomic response	- Inflammation - Increased enzymatic activity - Cell death - Genomic response
Long-term cellular / tissue effects (d – mo) [28, 33]	- Neuroplasticity - Vasospasm - Neurodegeneration	- Vascular invasion - Cartilage degeneration

[a]All effects are categorized by the approximate amount of time after impact that the onset of each particular effect occurs. Effects may remain and develop well beyond the timescale that they were initiated.

mechanical loading on the cellular level. This is particularly true of compressive loading, which plays a significant role in traumatic impacts but suffers from a dearth of studies exploring its effect on individual cells [41].

The experimental gap in dynamic cellular loading is due in large part to the lack of instruments capable of producing compressive micro-mechanical loads in a controlled manner. The existing device platforms that are capable of applying compressive forces to individual cells (*e.g.* AFM, magnetic tweezers, microplates) are each limited to some combination of low force magnitude (sub-μN), strain (< 10%), and strain rate (< 10 s^{-1}) [41-49]. Such parameters are useful for probing low force cellular processes and characteristics but fall short of replicating the loading conditions of external impacts transmitted to cells through tissue. Even more limiting is the low throughput of current devices (tens of cells per experiment), which makes gathering the data necessary for sensitive biological analysis of inherently heterogeneous cell populations difficult if not impossible [50].

To address these critical needs, my collaborators and I have developed a microfluidic MEMS device, the "μHammer," to subject individual cells to impact with an unprecedented combination of strain (10% to 90%), strain rate (30,000 to 200,000 s^{-1}), and throughput (over 360 cells/s). This device is composed of a single-crystal silicon microfluidic channel that transports cells to be impacted by an embedded nickel–iron (Ni–Fe) armature in microchip format. The Ni–Fe armature is magnetically driven by an external solenoid via an *in situ* Ni–Fe pole. The microfluidics MEMS device is bonded with a macroscale cartridge, which allows cells to be processed under sterile conditions and then removed after the loading event for immediate analysis or cultured *in vitro* for long term tracking. This set of capabilities will enable experiments that narrow the gap in our understanding of cell level responses to tissue-

level impact and pressure loading, ultimately enhancing our comprehension of traumatic injury pathways and facilitating the development of more sophisticated tools for diagnosis and therapy.

1.1 Outline

The overarching goal of this work is to introduce our microfluidic MEMS device, demonstrate its cell-impact capabilities, optimize its performance, and ultimately explore how it is uniquely suited to investigate the ramifications of traumatic impacts. In Chapter 2, I explore the literature related to traumatic brain and joint injuries on the tissue level to determine the loading conditions of these events, then use that information to deduce the impact parameters on the cellular level. Next, I present both the strengths and limitations of the devices typically used to apply dynamic compression to biological cells, demonstrating the need for a device specifically designed to study the effect of traumatic impacts.

In Chapter 3, I introduce the device my collaborators and I have developed to meet this need, the μHammer, and describe the design of its critical components. I discuss the evolution of these components from early designs to the current device generation, as well as the models, simulations, and behaviors that influenced device design. In Chapter 4, I begin by characterizing the actuation of the μHammer, then discuss the impact parameters it can generate in both present and future designs. I end the chapter by characterizing the timing of our device through simulations and experiments with polystyrene microbeads.

Chapter 5 demonstrates the μHammer's ability to apply biologically relevant strains and strain rates to a prototypical human cell line (leukemic K562 cells), presenting the results of several assays that monitor the viability of impacted cells across different timescales. In Chapter 6, I take a deeper look into the performance of our device under various experimental

conditions. Through this analysis, I explore how to optimize μHammer performance by manipulating the inertial focusing of particles travelling through it, then propose a number of potential geometric redesigns to further improve device throughput. The optimization techniques presented in this section are not just applicable to our device but can in fact be utilized by any microfluidic device that relies on consistent and predictable particle trajectories.

In Chapter 7, I explore how the impact parameters of the μHammer fit within the overall framework of forces applied to cells within the human body, with specific emphasis placed on traumatic impacts to the brain and joints. I conclude this document by introducing potential experiments for future work, including several experiments already underway investigating the cellular ramifications of TBI.

Chapter 2. Background

2.1 Loading conditions of traumatic brain and cartilage injuries

To date, the majority of research investigating the ramifications of traumatic impacts on the brain and cartilage has been performed on the tissue level [51, 52]. These studies have extensively documented the loading conditions applied to their respective tissue through both measurement and simulation of stress and other metrics of impact (see Table 2.1 for description of these measurements). Stress in the context of the brain is generally reported in terms of intracranial pressure (ICP), which in healthy individuals has a baseline steady-state value ranging from 0 to 1 kPa, with 3 kPa being the upper bound before corrective action is taken [53]. By contrast, articular cartilage (found in the joints between articulating bones) is subjected to orders of magnitude higher stresses on a daily basis, with normal physiologic stresses ranging from 0 to 20 MPa applied at a frequency of less than 1 Hz [33, 54]. Furthermore, articular cartilage regularly experiences compressive strains up to 30% during ambulation and other skeletal movements [55, 56], while the brain is generally insulated from such deformation. With the application of impact, however, the level of stress and strain increases dramatically in both the brain and articular cartilage (Table 2.2).

In the case of the brain, *in vivo* measurements of the dynamic ICP during controlled cortical impacts and weight drop impacts on live rats (applied strain 25% to 75%, applied strain rate 100 to 1,000 s^{-1}) show that the peak ICP in those cases is approximately 150 to 300 kPa, with rise times on the order of 10 ms [57-59]. Finite element model (FEM) simulations of these animal models predict a strain threshold of approximately 20% above which mechanical damage such as breakdown of the blood-brain barrier occurs [60]. While

Table 2.1: Common measurements used to describe loading conditions

Measurement	Definition	Variables	Equation	SI Units
Stress σ	Force per unit area	Force F Area A	$\sigma = \frac{F}{A}$	Pa
Strain ε	Change in length per initial length	Initial length l_i Final length l_f	$\varepsilon = \frac{l_i - l_f}{l_i}$	Dimensionless (fraction or %)
Stress rate $\dot{\sigma}$	Stress applied per unit time	Change in stress $d\sigma$ Change in time dt	$\dot{\sigma} = \frac{d\sigma}{dt}$	$Pa \cdot s^{-1}$
Strain rate $\dot{\varepsilon}$	Strain applied per unit time	Change in strain $d\varepsilon$ Change in time dt	$\dot{\varepsilon} = \frac{d\varepsilon}{dt}$	s^{-1}

the mechanical loading conditions experienced by the brain during impact have never been directly quantified in humans, other parameters such as acceleration have been measured that allow the intracranial forces to be deduced. Hernandez et al. report that, based on six degree-of-freedom measurements gathered from athletes combined with FEM modeling of the brain as a linear viscoelastic material, the peak strains for brain tissue were 49.8% for a loss of consciousness (LOC) event and an average of 16.4% for non-injury events [61]. This corresponds to a maximum intracranial pressure of 83.7 kPa for the LOC impact and a mean peak pressure of 32.5 kPa for the remaining hits. An earlier study by Zhang et al. produced similar results, reporting that impact forces to the brain lasted for 10 to 20 ms with rise times on the order of 5 to 10 ms based on the observed dissipation of force over time [62].

As previously mentioned, percussive blasts from explosions are another form of brain tissue loading that is a common cause of TBI in the military. While the loading from the translational and rotational acceleration of the brain in physical impacts differs in many respects from the pressure waves that travel through the brain following percussive blasts, they both result in compression, stretching, and shearing of their respective tissue that lead to

Table 2.2: Tissue-level traumatic impact parameters from literature

Device	Strain	Strain Rate	Stress	Stress Rate	Duration
TBI – Physical Impact	High	Med	Med	Med	Med - High
TBI – Percussive Blast	Med - High	Med - High	Med - High	Med - High	Low - Med
Cartilage Impact	Med - High	Med - High	High	Med - High	Med - High
Legend	Strain	Strain Rate	Stress	Stress Rate	Duration
Low	< 1%	< 10 s^{-1}	< 10^3 Pa	< 10^6 Pa/s	< 10^{-3} s
High	> 10%	> 10^3 s^{-1}	> 10^6 Pa	> 10^9 Pa/s	> 1 s

material breakdown [28, 53, 61, 63]. FEM simulations and animal models of blast-induced brain injuries demonstrate higher intracranial pressures (on the order of hundreds of kPa to MPa) and shorter durations of pressure loading (rise times on the order of μs and durations less than 2 ms) compared to physical impacts [17, 59, 63, 64]. The pressure waves generated by both types of impact are thus inherently dynamic, resulting in stress rates ranging from kPa/s to MPa/s, and even up GPa/s in the case of percussive blast events. Since the brain as a whole is viscoelastic in nature, the strain is predicted to evolve on a slower timescale than the stress, but still in a dynamic fashion with strain rates ranging from 10 to over 1,000 s^{-1} in FEM simulations [28, 63, 65, 66].

In the case of cartilage, pathological impact loading has been studied extensively *in vitro*. Since cartilage is a relatively accessible form of tissue, these studies have been performed on both animal and human models, typically in the form of cartilage (and occasionally bone) explants subjected to weight drop or some other form of dynamic controlled compression. The impact parameters in these models typically involve high strain (10% to 60%) and stress (1 to 100 MPa) magnitudes, with rise times on the order of 1 to 10 milliseconds [18, 54, 67]. This leads to high strain rates well over 1,000 s^{-1} and stress rates over GPa/s. These studies indicate that the loading threshold above which the structure of cartilage begins to breakdown is

approximately 20% to 30% applied strain and 20- to 30-MPa applied stress, and that the extent of damage may be increased by higher loading rates [33, 68, 69]. The strain threshold for cell death was even lower, occurring at approximately 10% strain [18, 67]. The stress threshold for cell death may also have been lower, with one study by Bartell et al. reporting a value of 2 MPa, although this was obtained at a significantly higher strain rate (4,000 s^{-1}) than comparative studies which may have contributed to this lower value [67]. *In vivo* studies investigating cartilage impact in live animals offer less control of the impact parameters but still apply similar peak stresses (up to 50 MPa) and stress rates (up to 500 MPa/s) [33, 70, 71]. Although the loading conditions of cartilage during traumatic impacts are complex due to the contribution of muscles and the surrounding tissue [70], mathematical models and other simulations predict that these loading conditions are a reasonable approximation of those experienced on the tissue level during real-life impacts [54, 72].

As these studies indicate, traumatic impact has been explored extensively on the tissue level leading to a comprehensive understanding of the macroscale loading parameters in both the brain and the joints (Table 2.2). The loading conditions applied to individual cells during these events, however, is less well understood. If we assume uniform, affine deformation and an average cell contact area on the order of 100 μm^2, we can predict that the compressive stresses measured on the tissue level during traumatic impacts will result in cellular loading forces on the order of μN to mN with similar loading rates. While there is a certainly a degree of correlation between the macroscale and the microscale (especially when comparing the relative severity of two impacts), it is not necessarily accurate to assume that deformation is homogeneous across length scales and that bulk loading conditions are equivalent to those on

the cellular level. Such an assumption is likely to break down, due in large part to the increasing amount of heterogeneity on the microscale level [73].

In order to determine how cells deform in response to macroscale forces applied to tissue, one must account for both regional heterogeneities [29, 74] as well as differences between the mechanical properties of the cell and the surrounding extra-cellular matrix [75]. A number of different multiscale models have measured the high strain and high strain rate deformation of cartilage tissue *in vitro,* with a resolution as fine as 40 μm [67, 68, 76]. These models indicate that the peak local compressive strain and strain rate values are up to six times higher on the micron scale than the peak values for bulk tissue on the millimeter scale. Although such microscale studies have not been performed on the brain, one would expect this variation in loading parameters to be amplified due to the increased heterogeneity of brain tissue across all length scales compared to cartilage tissue, leading to localized variations in deformation as predicted by microscale simulations [73, 77-79]. Such differences are amplified by the fact that most tissue-level simulations model the brain's various component tissues as linear viscoelastic materials, when in fact they can be nonlinear and can exhibit strain softening, with a strong dependence on strain rate [29, 49, 80]. Given these shortcomings in both length scale and material properties, it is likely that deformation and especially deformation rate are higher on the cellular level than reported on the tissue level. This allows us to deduce that the magnitudes of the loading parameters experienced by tissue on the macroscale represent the minima of those experienced by cells on the microscale. Thus, brain and cartilage impact loading results in high forces (μN to mN), strain rates (over 1,000 s^{-1}), and strain magnitudes (10% to over 50%) applied to cells over a short duration (μs to ms), a combination of loading

conditions which are difficult to reproduce in controlled environments with current technology, especially in regards to compression.

2.2 Loading conditions of cell compression devices

There are numerous challenges associated with reproducing the dynamic loading conditions experienced by cells during traumatic impacts, especially given the lack of a comprehensive understanding of how impact energy is transmitted through tissue to the microscale as discussed in the previous section [3, 29, 81]. Furthermore, though much of the stresses and strains experienced during impact are compressive, these forces are difficult to apply to individual cells in a controlled manner and thus most studies are confined to analysis of shear and tensile loading [3, 6, 82-85]. Therefore, based on the analysis in the previous section, a system for applying compressive forces of μN to mN over μs to ms duration is of much interest. The system must also be capable of applying controlled deformations on the order of μm with a rise time on the order of μs to ms, in order to apply high compressive strains (> 10%) and strain rates (> 1,000 s^{-1}) to biological cells with diameters typically around 10 μm.

The simplest and most common method of compressing cells involves the application of force to cells in synthetic 3D matrices or monolayer cell cultures through weights, microstamps, or even explosive blasts [13, 20, 21, 41, 86, 87]. These experiments are valuable since they mimic the *in vivo* loading conditions of cells in tissue by including cell-cell and cell-matrix interactions. However, they provide little control over the loading conditions applied to each individual cell, making it difficult to obtain precise and repeatable data. Furthermore, these experiments cannot effectively isolate the cellular response to mechanical force from other responses to the surrounding environment. Thus, experiments involving the

Table 2.3: Single-cell impact device parameters from literature

Device	Force	Strain	Strain Rate[a]	Throughput
Magnetic tweezers	Low - Med	Low - High	Low - Med	Low
AFM	Low - High	Low - High	Low	Low
Microplate	Med - High	Med - High	Low	Low
Micropipette aspiration	Low - Med	Med - High	Low	Low
Microfluidics	Med - High	Med - High	Med - High	Med - High
MEMS	Low - High	Low - High	Low	Low
Legend	Force	Strain	Strain Rate	Throughput
Low	$< 10^{-9}$ N	< 1%	< 10 s^{-1}	$< 10^2$ cells / experiment
High	$> 10^{-6}$ N	> 10%	$> 10^3$ s^{-1}	$> 10^4$ cells / experiment

[a]Strain rates reflect those reported in medium to high force / strain experiments with cells and may not reflect the full technical capabilities of the device itself.

application of force to individual cells are necessary to effectively investigate this phenomenon, which once understood can shed light on the role of more complicated interactions with the surrounding environment experienced by cells during batch loading and *in vivo*.

A number of different devices have been developed over the years that are capable of applying force to individual cells in a controlled manner. Optical tweezers are a common force application tool on the microscale capable of applying calibrated forces to micron-scale dielectric particles in the range of 50 to 100 pN [88]. Though they are useful for probing the force response of subcellular structures (i.e. focal adhesions, axonal extensions), they are not suited for probing whole cells. Magnetic tweezers have been shown to achieve higher forces in the range of tens of nN, however, uniaxial tension is the most common loading geometry (see Table 2.3 for comparison of various cell-impact devices) [46, 89, 90]. Atomic force microscopy (AFM), on the other hand, has been developed to apply precise compressive loads of ~10 to 100 nN [43, 44, 91-93] and is capable of deforming the cell locally or globally

depending on the tip geometry. Higher compression forces up to cell bursting (1 to 10 μN, ~70% strain) can be achieved by using very stiff AFM cantilevers modified with microbeads to expand the contact area or by utilizing microplate technologies with high-precision load cells, but to our knowledge these systems have not been utilized for high-speed loading at such high forces [45, 47, 48, 94, 95]. Each of these systems apply forces to cells in a controlled environment quite different from their biological milieus, with the cells typically being adhered to glass or other similarly stiff substrates. As such these platforms are more suited for adherent cells and make experiments with non-adherent cells difficult [96]. Micropipette aspiration, on the other hand, is a common technique capable of deforming both suspended and adherent cell types with high strain, but it is typically used to deform cell membranes rather than the whole cell and is only capable of low loading rates [97, 98].

Though some of these platforms come close to or are even capable of approximating the loading conditions that occur during traumatic impacts, they all require extensive preparations for each cell to be impacted and thus are constrained to small sample sizes in the tens of cells (with the exception of population-based methods which lack precise control over cellular loading conditions as discussed above). Since cells are by nature heterogenous with a wide variety of potential phenotypes, much larger sample sizes in the thousands are necessary in order to gain a robust picture of the average cellular response to impact [50]. The most promising form of technology used to overcome this limitation is microfluidics, which describes a class of devices that involve flow of liquid and suspended particles through channels with dimensions on the scale of microns. By pushing cells through constricted regions of a channel with a width less than the cell diameter, microfluidic devices can subject hundreds to thousands of cells to up to 50% strain at a strain rate over 100 s^{-1} [98, 99]. Even

higher throughput, strain magnitudes, and strain rates can be achieved with hydrodynamic mechanotyping devices that use interacting fluid flows to deform cells, albeit in the form of stretching rather than compression [100-102]. These microfluidic devices have been used with great success to interrogate the mechanical properties of cells. However, they are not as well-suited to explore the cellular response to impact since the strain rates and impact durations they apply to each cell are determined by that cell's mechanical properties, severely limiting control over the loading conditions. In order to take advantage of the high-throughput capabilities of microfluidics while also maintaining control over the impact parameters, microfluidic technology can be combined with a micro-electromechanical system (MEMS). MEMS devices are on the same length scale as microfluidic devices and are manufactured with similar processes. Thus, they are well-suited for integration with microfluidics. They involve intricately designed geometries that move in response to various inputs (electrical, thermal, or magnetic) in a controlled and predictable manner. As a result, they are capable of applying precise and adjustable mechanical loads to cells that largely mirror those experienced during traumatic impacts, although to date MEMS cell-impact devices have typically been limited to lower strain rates [42, 50, 103]. In the following chapters, I describe the design, characterization, and implementation of a high-throughput microfluidic MEMS device, the μHammer. This device can deliver well-defined mechanical compression with high strain magnitude, high strain rates, and short compression duration to individual cells. These impacted cells can easily be removed for off-chip analysis, allowing investigation of the effects of cellular mechanical injury induced by extreme impact events.

Chapter 3. Device Design

3.1 Introduction

As discussed in Chapter 2, microfluidic MEMS devices are well-suited to solve the problem of dynamically loading cells with physiologically relevant forces, since they utilize feature sizes on the same dimensions as cells while being capable of serial interrogation of large sample sizes [104]. Several reviews have been published in recent years identifying MEMS and microfluidics as being uniquely suited to address the needs of single-cell mechanical perturbations [42, 50]. By combining the tailored force ranges of MEMS with the high-throughput capabilities of microfluidics, large populations of cells can be impacted one at a time and then recovered after loading for a wide range of imaging and biological assays. This allows the same loading conditions to be applied to thousands of cells, building a sufficient sample size to enable sensitive biological analysis of inherently heterogeneous cell populations.

To harness this potential, my collaborators and I have developed and fabricated our own microfluidic MEMS device, the μHammer. The general design of this device is based on a chip created by Owl biomedical (USA) for high-throughput cell sorting [105, 106]. This allows the μHammer to interface with the MACSQuant® Tyto® system (designed by Owl biomedical; manufactured by Miltenyi Biotec, Germany), which contains the tools necessary to flow and track cells through the device with high throughput. The μHammer chip itself is approximately 1,000-μm long by 600-μm wide when viewed from above (Figure 3.1) and consists of three main components: the microfluidic channels and vias, the released μHammer impact assembly (impact face, Ni–Fe armature, and S-curve spring), and the magnetic

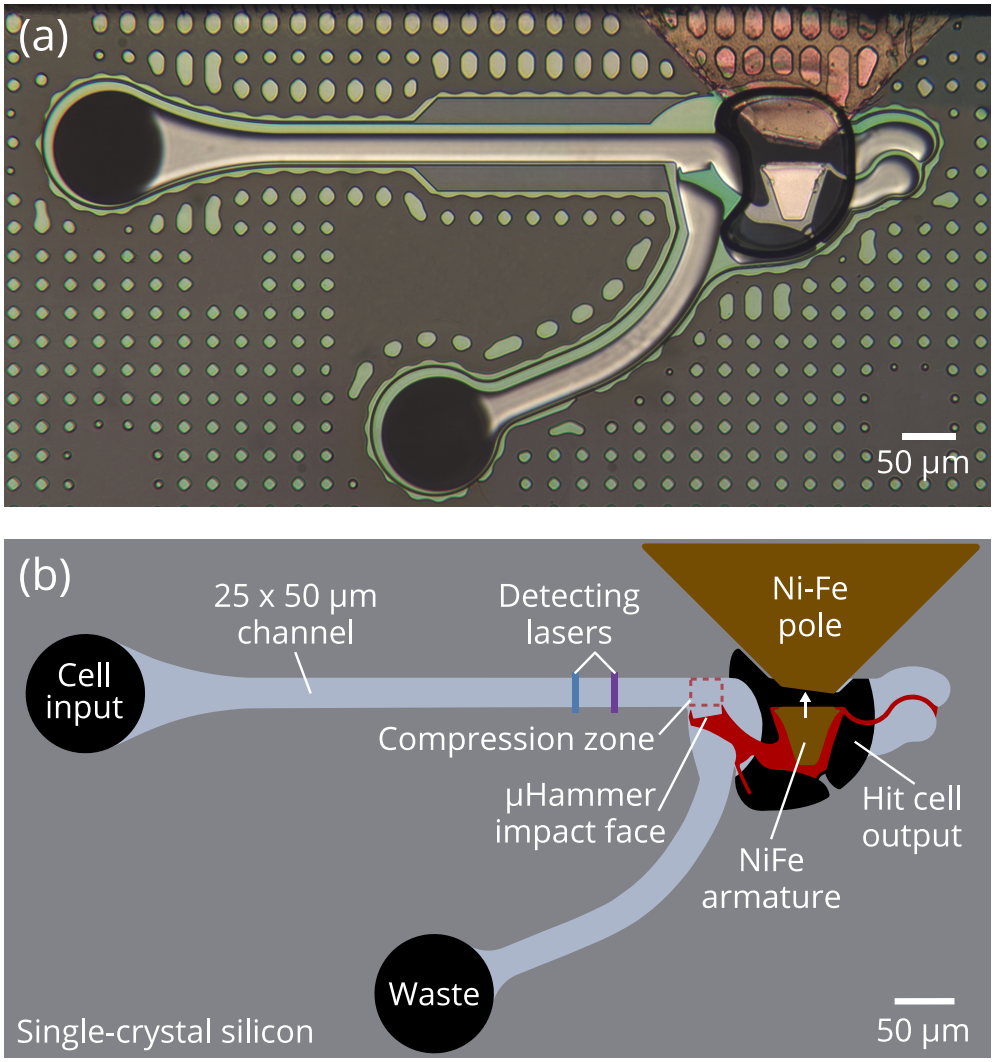

Figure 3.1: (a) Top-view micrograph of fabricated µHammer chip. Single crystal silicon in green, Ni–Fe magnetic pole and armature in tan, input and output vias in black. (b) Two-dimensional schematic of µHammer device with important features labeled. Arrow on Ni–Fe armature depicts direction of actuation. Dotted red box surrounds the µHammer compression zone where cells can be impacted by the µHammer face. Cell input, output, and waste vias all travel into the page to interface with a macroscale cartridge (described in Section 3.5). See Appendix A for scanning electron microscope images that provide an angled view of the µHammer chip.

assembly (external solenoid and Ni–Fe pole). In this chapter, I describe both the current iteration of the device (the second generation) as well as any significant changes from the first generation to help explain the features of the current design.

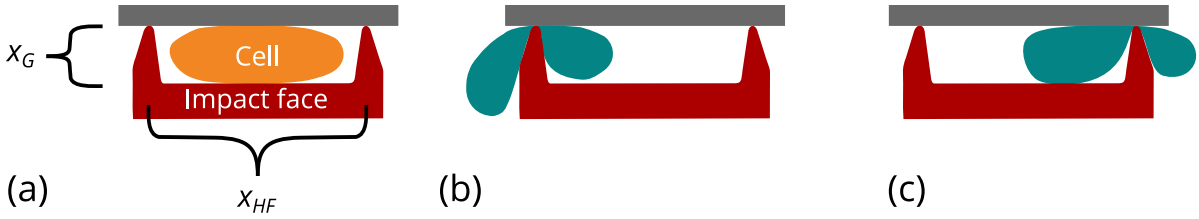

Figure 3.2: The current impact face design sets the final gap length x_G and prevents off-center impacts. (a) Centered impact of cell (in orange, labeled) compressed by μHammer impact face (in red, labeled) against top of channel wall (in grey). The final gap distance, x_G, is 7.5 μm and the impact face width between pincers, x_{HF}, is 28 μm. (b) Off-centered cell impact (in blue) from device closing too early. (c) Off-centered cell impact from device closing too late. Note how cells in panels b and c are locally compressed to a gap size of 0 μm by the pincers, likely bursting the cell membrane and potentially cutting the cell in half.

3.2 Design of μHammer channel and impact face

The dimensions of the channels (25-μm wide by 50-μm deep) were chosen to easily accommodate a large variety of cell types without obstructing flow. The current channel width was optimized for cells with an average diameter up to 20 μm, but can easily be changed in the future for larger or smaller cells.

In the first design generation, on the other hand, the channel was only 18-μm wide and was optimized for cells smaller than 15 μm. As a result, cells larger than 18 μm were forced to deform in order to flow through the channel. Furthermore, this first-generation channel width was prone to clogging. Non-deformable particles up to 20 μm would occasionally evade filtration and become wedged across the width of the channel, significantly diminishing flow through the device.

The μHammer impact face (Figure 3.2) extends from the Ni–Fe armature and is 28-μm wide by 50-μm deep to allow for the expansion of cells during compression in the plane transverse to the direction of motion. On each end of the impact face are 4-μm wide by 7.5-μm

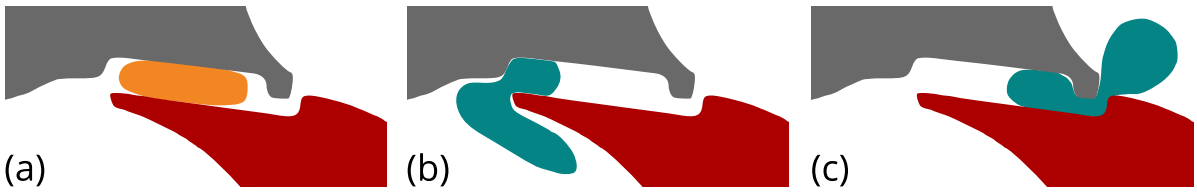

Figure 3.3: The first-generation impact face design allowed for non-ideal impacts. µHammer impact face depicted in red, and channel wall depicted in grey. Centered cell impact (in orange) depicted in (a), with off-centered impacts (in blue) depicted in (b) and (c). Note how cells in off-centered impacts experienced non-uniform impact but were compressed to a non-zero gap distance and thus likely survived.

long triangular "pincers," which bound the impact face to secure the cells in the compression zone during impact. The pincers burst cells that are not correctly aligned with the impact face during compression, which effectively eliminates them from the output sample and preserves the uniformity of impact parameters on the hit cells (Figures 3.2b and 3.2c). Additionally, they provide a hard stop for the µHammer's actuation, setting the final gap distance at 7.5 µm. This final gap can be adjusted by altering the pincers' height so that the desired amount of compression can be applied to each cell. Currently, we also have a device fabricated with 4-µm long pincers to apply even higher strain to cells.

In the first design generation, the impact face was not as wide (only 20 µm) and was not bounded by pincers. As a result, cells impacted outside the center of the impact face experienced non-uniform compression and likely survived (Figure 3.3), diminishing the consistency of loading conditions in the impacted cell population and adding noise to the resulting datasets.

3.3 Design of µHammer spring

To provide a pivot point for actuation and a restoring force to return the µHammer back to its original position, the µHammer armature is anchored by an S-curve spring (Figure 3.1,

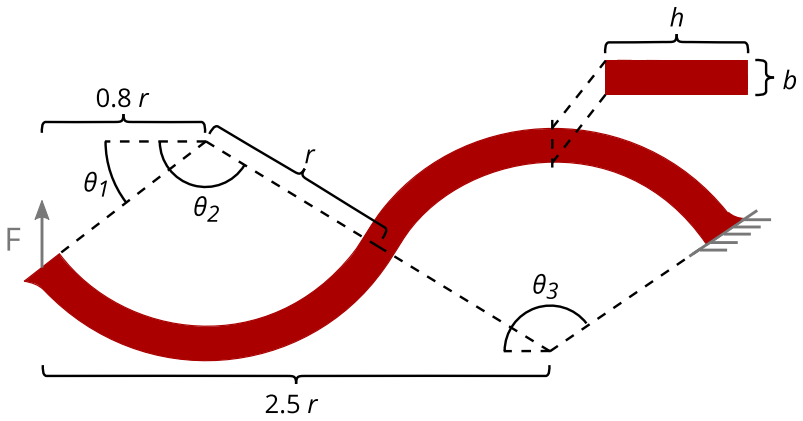

θ_1	θ_2	θ_3	r	h	b
0.664 rad	2.611 rad	2.559 rad	22.63 μm	50 μm	3.80 μm

Figure 3.4: S-curve spring schematic. Table lists geometric parameters used in the calculation of spring stiffness for the current design generation.

Figure 3.4 for detailed view). This design offers significant advantages over a straight lever arm: it provides a softer spring with the same overall length, while increasing stability and minimizing out-of-plane torque. The stiffness, k, of the spring to an in-plane force (applied to the end of the spring and perpendicular to the μHammer impact face) can be estimated using energy methods and Castigliano's theorem:

$$k = \mathbf{F}\left[\frac{\partial}{\partial \mathbf{F}}\left(\int_{\theta_1}^{\theta_2} \frac{\mathbf{M_1}^2(\varphi)}{2EI} r d\varphi + \int_{\pi-\theta_2}^{\theta_3} \frac{\mathbf{M_2}^2(\varphi)}{2EI} r d\varphi\right)\right]^{-1}$$

where $\mathbf{M_1} = 0.8r - \cos\varphi$, $\mathbf{M_2} = 2.5r - \cos\varphi$, $I = hb^3/12$, and the Young's modulus of silicon, E, is 170 GPa. Substituting these values along with those described in Figure 3.4 results in a stiffness value of 224 N/m, with the scaling $k \sim Ehb^3/r^3$.

According to this relationship, the stiffness of the spring and its subsequent restoring force depend predominantly on the width of the spring, b, its radius of curvature, r, and the overall length of the spring, all of which can be modulated in future designs. It also depends on the

Young's modulus of the material, E, and the height of the spring, h, both of which are set by the fabrication technique.

To confirm this analytical value, I created a two-dimensional (2D) steady-state finite element model of the μHammer in COMSOL, solving for structural deformation under the influence of a point load on the end of the spring. This resulted in a linear stiffness of 240.1 ± 0.1 N/m that is within 10% of the analytically derived value, with much of the error likely due to the geometrical complexities of the spring that were not captured in the analytical model.

In the first design generation of the device, the width, b, was 1.95 μm and the overall length was about twice as long, resulting in an order of magnitude lower stiffness (~10 N/m as determined via COMSOL simulation). While the lower stiffness did provide finer control over the actuation of the device, it proved to be too soft for consistent and predictable performance. See Chapter 4 for further analysis of the ramifications of this soft spring design on actuation.

3.4 Design of μHammer magnetic assembly

To actuate the device, we use an electromagnetic assembly designed by Owl biomedical (USA) that is a component of their MACSQuant Tyto system. This actuation assembly consists of an external solenoid that abuts the μHammer's 45/55% Ni–Fe pole (Figure 3.5). The external solenoid is composed of 28 turns of copper wire wrapped around a 49/49/2% Co–Fe–V core that has a highly nonlinear relative magnetic permeability, μ_r, and a 2.34-T magnetic saturation field [105]. It is spring-loaded in the plane of the chip to enable intimate contact between the tip of the solenoid and the chip, resulting in a nominal distance of 10 μm between the solenoid tip and the Ni–Fe pole. Applying a current to the solenoid results in a magnetic field, $\boldsymbol{B}$, that is a function of the current applied, I_s, the relative magnetic

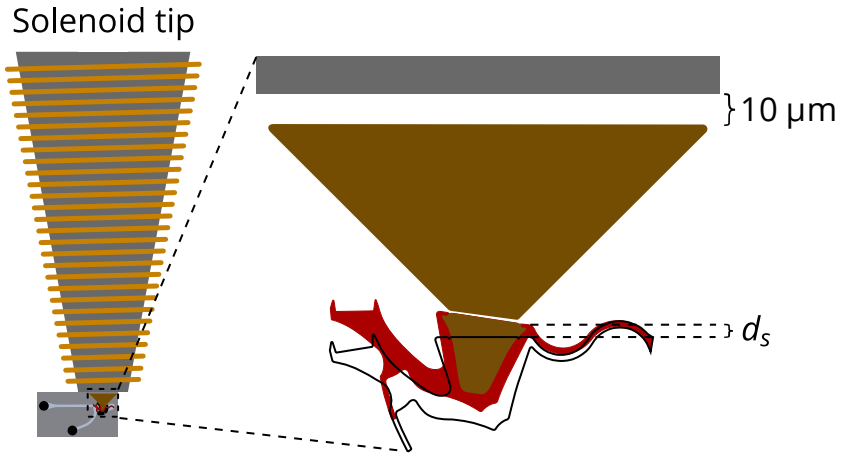

Figure 3.5: Solenoid and Ni–Fe pole schematic. Solenoid core in gray with 28 turns of copper wire in orange, Ni–Fe pole and armature in brown, actuated µHammer in red compared to µHammer at rest in black outline. Spring displacement, d_s, depicts vertical displacement of S-curve spring tip. Nominal distance between Ni–Fe pole and solenoid is also marked.

permeability of the material, μ_r, and the number of turns of the solenoid, while being roughly inversely proportional to the distance from the tip of the solenoid. This B-field travels through the µHammer's Ni–Fe pole to its released Ni–Fe armature, where it generates a magnetic force $\boldsymbol{F_m} = \boldsymbol{\nabla}(\boldsymbol{m} \cdot \boldsymbol{B})$. The magnetic moment $\boldsymbol{m} = \int (\mu_r - 1)/\mu_0 \, \boldsymbol{B} \, \mathrm{d}V$, where μ_0 is the vacuum permeability and the integral is taken over the volume V.

The Ni–Fe pole was designed by Owl biomedical to minimize the drop-off in B-field between the external solenoid and the released armature (both of which have a 1.6-T magnetic saturation field), thereby maximizing the applied magnetic force [106]. Its tapered geometry was optimized to focus the B-field to a maximum gradient in the region of the armature. It should be noted that the device operates in a regime in which the B-field of both the Ni–Fe pole and armature are highly non-linear functions of the driving parameters, since the materials are at or near magnetic saturation.

To analyze the magnetic field and resulting magnetic force generated by the solenoid, I developed 2 three-dimensional (3D) steady-state finite element models of the magnetic assembly in COMSOL, one with the optimized tapered Ni–Fe pole geometry used in the device and the other with a generic rectangular pole geometry. These models first determine the electric field in response to a current applied across the solenoid coils, then calculate the resulting B-field and ultimately the magnetic force applied to the Ni–Fe armature. In the tapered pole model, the magnetic force applied to the armature at rest appears to reach saturation at current values above 4 A (Figure 3.6a). The rectangular pole model, on the other hand, applies about half the magnetic force to the armature at each of the current values tested while never reaching saturation. This indicates that the geometry of the tapered pole enhances the magnetic nonlinearities. By taking advantage of this and operating the solenoid in the saturated region, we reduce the change in applied load to the armature that accompanies slight changes in applied current, making the resulting actuation more robust and consistent.

Since the magnetic field and resulting magnetic force applied to the armature changes as it moves in tandem with the spring, I used the COMSOL model of the magnetics to determine the magnetic force as a function of spring displacement, d_s (Figure 3.5). I chose an input DC current of 5 A in combination with the tapered Ni–Fe pole geometry to ensure that the device was operating above magnetic saturation (Figure 3.6a). As shown in Figure 3.6b, the applied magnetic force (with the magnitude adjusted to represent the force applied to the spring tip) is initially 1.5 mN, enough to rapidly pull the armature toward the pole. This causes the released impact assembly to rotate in-plane around the anchor point, increasing the applied magnetic force as the gap between the armature and pole decreases. This applied force is always higher than the restoring spring force, resulting in a relatively constant net force above

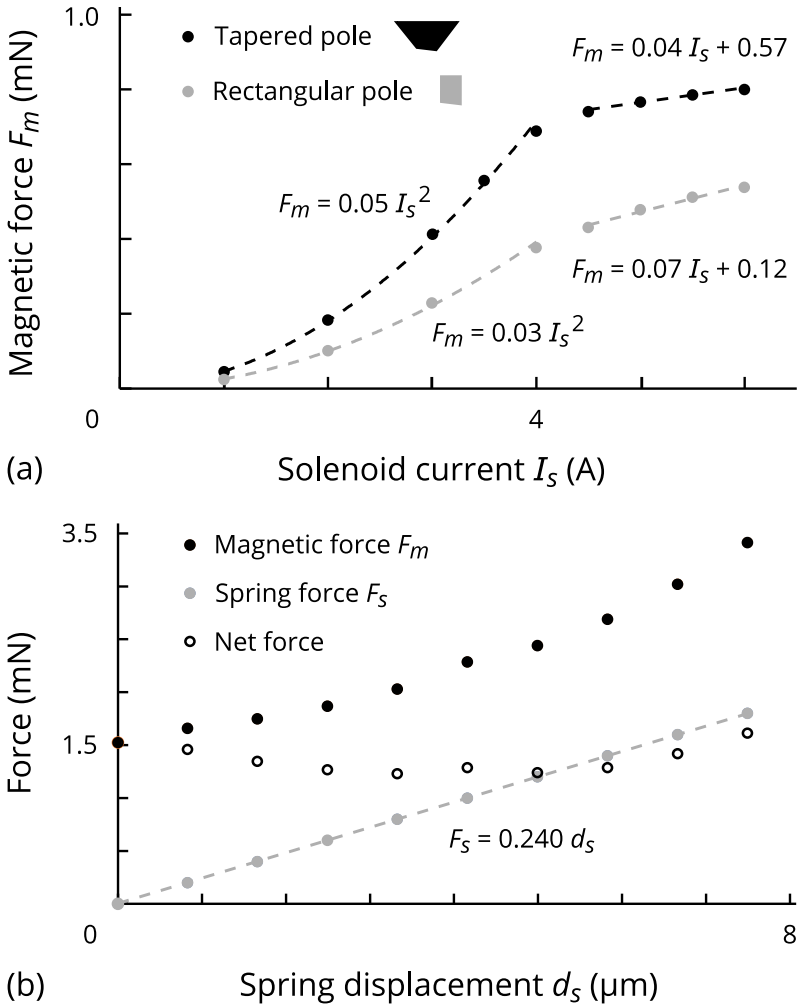

Figure 3.6: COMSOL simulation of forces applied during μHammer actuation. (a) Tapered vs rectangular Ni–Fe pole design. Points depict magnetic load applied to Ni–Fe armature by each design at rest (d_s = 0) at varying current values as determined by 3D COMSOL model. Equations of best fit lines shown for exponential phase (up to 4 A) and linear phase (above 4.5 A). Note the nearly doubled slope value in the linear region of the rectangular pole (0.07 mN/A) as opposed to the tapered pole (0.04 mN/A), which appears to have reached saturation. (b) Force applied to end of silicon spring. Grey points depict restoring S-curve spring force as a function of spring tip displacement (d_s, see Figure 3.5) calculated by 2D COMSOL model. Black points depict magnetic force applied to Ni–Fe armature by solenoid (adjusted to represent force applied to end of spring) as a function of spring tip displacement calculated by 3D COMSOL model. Black open circles depict net force applied to end of spring (applied magnetic force minus restoring spring force). Stiffness of spring to in-plane deflection towards upper wall of channel (240.1 ±0.1 N/m) determined by taking slope of spring force-displacement best fit line via a Levenberg-Marquardt optimization algorithm in MATLAB R2015B.

1 mN that will rotate the armature through its entire range of motion until contact with the channel wall.

In order to achieve a consistent magnetic field and thus a consistent magnetic force as shown in Figure 3.6, the Ni–Fe pole must be aligned with the external solenoid tip (which generates the magnetic field) in all 3 axes. As previously mentioned, the external solenoid is a part of the MACSQuant Tyto system. This system includes feature-tracking software and motorized stages that align landmarks on the device a calibrated distance from the stationary solenoid. Proper alignment with the solenoid both maximizes and standardizes the applied magnetic force, ensuring consistent actuation across devices. Throughout the course of an experiment, the Tyto software checks and adjusts the alignment at 30-second intervals, maintaining alignment to within ±5 μm. Simulations indicate that the force applied to the armature is more sensitive to variations in the distance from the solenoid tip to the device (labeled in Figure 3.5; ±0.08 mN when the distance is varied by ±5 μm with the device at rest) than in the horizontal or vertical direction (-0.02 mN). However, this variation is at most 5% of the total force. Thus, variations in alignment during operating conditions are negligible, as long as the solenoid tip is in intimate contact with the μHammer chip (which is ensured by the spring-loaded design).

As mentioned above, I chose to trigger the solenoid with a 5-A DC current during actuation. This value not only ensures that the device operates comfortably above magnetic saturation, but it also minimizes heat generation and dissipation (which scales with I_s^2) compared to other current values above the saturation threshold. Limiting these is important, both to prevent the solenoid from overheating as well as to avoid temperature swings in the cellular environment that can lead to heat shock and other detrimental effects. Once the device

reaches full actuation with the Ni–Fe pole and armature in close proximity, this 5-A "ignition" current is lowered to a 2-A "hold" current, which is high enough to hold the device in place while further minimizing heat dissipation during compression. The amount of heat dissipation varies from 55 to 715 mW depending on the "hold time" of full actuation. Since some heat dissipation is unavoidable, a copper heat sink surrounds the solenoid to transfer heat away from the device. Furthermore, the solenoid, cartridge, and cell buffer are housed in a temperature-controlled environment with a user-controlled set point ranging from 4 °C to 37 °C (±1 °C) to minimize temperature fluctuations.

3.5 Fabrication of μHammer device

The devices are fabricated by Innovative Micro Technology, Inc. (USA) using a 14-layer process [107]. This process can be divided into three main steps: etching the silicon actuator wafer, etching the silicon via wafer, and bonding the components together (see Appendix B for detailed description of fabrication). Once the chip itself is assembled, the exposed underside of the via wafer is bonded by Owl biomedical (USA) to a macroscale interposer, which serves as a conduit between the three vias (input, output, and waste, Figure 3.1) and the macroscale cartridge (both of which are proprietary and Tyto-compatible). Each via feeds to a separate chamber in the cartridge that can hold up to 10 mL of fluid (cell suspension input or output). Once the interposer and cartridge are bonded together, they are sterilized with a validated Ethylene Oxide (EtO) process, completing the fabrication of the μHammer assembly.

Chapter 4. Device Characterization

4.1 Introduction

In order to use the μHammer to impact cells, I first needed to characterize the device's actuation and timing. To do this, I determined the μHammer's position as a function of time after the magnetic field was turned on with solenoid activation. This allowed me to calculate the velocity of the impact face during compression, and ultimately to predict the appropriate timing of solenoid activation. This timing must account for the inherent delay between solenoid activation and the μHammer impact face entering the compression zone, as well as the velocity of the cell and its location within the channel. At the beginning of this chapter, I describe how the device actuates and explore the range of impact parameters the device can apply to individual cells. I then discuss how this information was used to characterize the timing of μHammer impacts, first via simulation and then experimentally with polystyrene beads.

4.2 Characterization of μHammer actuation

4.2.1 Methods

To characterize the actuation profile of the μHammer, I loaded it into the MACSQuant Tyto system and flowed Tyto Running Buffer (Miltenyi Biotec, Germany) through the device with the system's integrated flow-controlled pump. I then captured strobed images (using a Cognex Advantage 100 camera) of the device at 1-μs intervals after triggering the Tyto's solenoid actuation assembly, which was aligned with the μHammer's Ni–Fe pole as described in Chapter 3. This experiment was first performed with the 7.5-μm final gap distance (x_G)

Table 4.1: Approximate pressure applied by Tyto as a function of flow rate and temperature

	8 °C	37 °C
4 ml/hr	500 – 600 mbar	300 – 400 mbar
8 ml/hr	1100 – 1200 mbar	700 – 800 mbar

device with flow rates of 4 ml/hr and 8 ml/hr, at both 8 °C and 37 °C (see Table 4.1 for the pressures applied by the Tyto to achieve the desired flow rate at each temperature). In order to highlight the design flaws of the previous device generation described in Chapter 3, I also captured strobed images of a first-generation device while actuating with a flow rate of 4 ml/hr at 8 °C. As discussed in Section 3.4, the solenoid was activated with a 5-A DC current in all experiments, ensuring that it was above the saturation threshold while minimizing the amount of heat dissipated in the system (which scales with I_s^2). Once the images were acquired, I processed them in ImageJ (Version 1.50i, public domain) to measure the gap distance between the μHammer impact face and top of the channel as a function of time.

After measuring and quantifying the μHammer's actuation, I created a time-dependent 2D COMSOL model of the device and optimized its actuation profile to mirror the experimental results. This model solves for structural deformation of the impact assembly (in response to a boundary magnetic force applied to the armature) and fluid velocity (in response to pressure applied at the inlet). Once this model was generated, I then used it to precisely determine the velocity of the μHammer during actuation via a centered finite difference approximation of the first numerical derivative of the position data.

4.2.2 Results and discussion

4.2.2a Current device generation

As shown in Figures 4.1 and 4.2, the impact face of the current μHammer design with a 7.5-μm gap distance (x_G) entered the channel (and thus the compression zone) approximately 10 μs after the solenoid was activated at a temperature of 8 °C with a flow rate of 4 ml/hr. The amount of time required for the μHammer to close completely after solenoid activation, t_{SC}, was 18 μs. It remained at full actuation with the pincers in contact with the channel wall during the entire user-specified hold time, after which it returned to rest (~20 μs after the solenoid was turned off). Figure 4.2 also shows that the 2D COMSOL simulation of actuation closely matches the experimentally measured profile, and thus provides an accurate model for further simulation. Using this model, I determined that the velocity of the μHammer ranges from 2 to 3 m/s as it travels across the compression zone, with an average velocity of 2.6 m/s (Figure 4.3).

When the device was actuated at 37 °C (data not shown), the device closed approximately 1 μs sooner than at 8 °C (t_{SC} = 17 μs vs 18 μs), likely due to the decreased viscosity of the buffer fluid at this temperature (0.7 mPa·s at 37 °C vs 1.4 mPa·s at 8 °C). Despite this slight decrease in time to complete actuation, however, the overall actuation profile at 37 °C had the same shape and range of compression velocities as at 8 °C (Figures 4.2 and 4.3). Furthermore, the actuation of the device did not change with flow rate, with the same profile occurring at 8 ml/hr (not shown) as at 4 ml/hr (Figure 4.2).

It is important to note that all of the devices tested (N = 15) were from the same fabrication batch, with each batch yielding hundreds of devices. Due to etching tolerances and other variations in manufacturing, the thickness of the μHammer spring can vary by up to ±0.15 μm

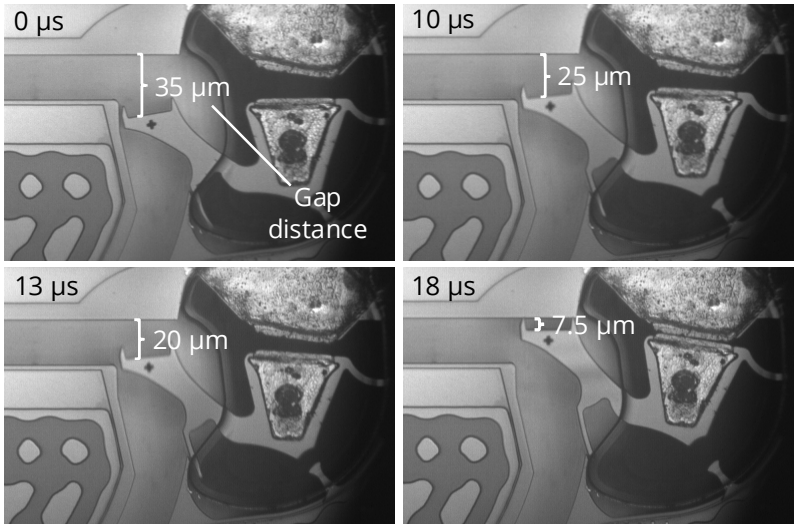

Figure 4.1: Strobed images of µHammer actuation as a function of time after solenoid activation. Device actuated at 8 °C with a 4 ml/hr flow rate. White brackets denote gap distance between µHammer impact face and top of channel at each timepoint until closure to a 7.5-µm final gap distance at 18 µs.

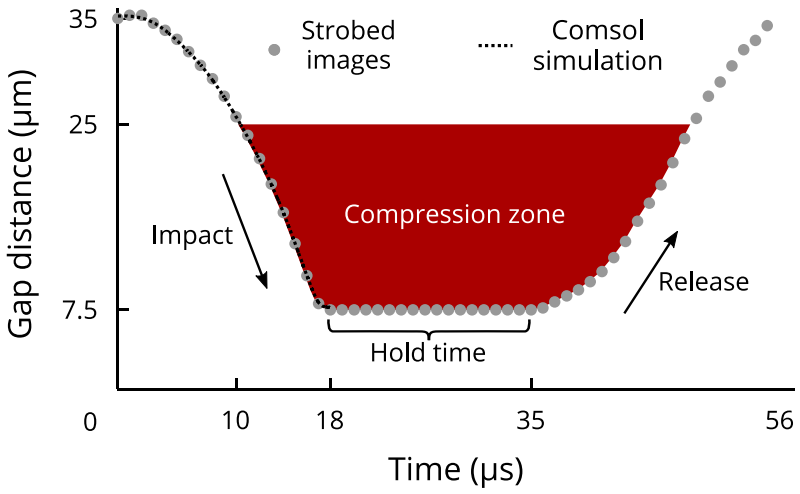

Figure 4.2: Characterization of µHammer actuation at 8 °C with a 4 ml/hr flow rate. (a) µHammer compression and recovery profile of current device design with 7.5-µm final gap distance. Grey points measured from strobed images of devices from actuation until full recovery after release. N = 15 devices, standard deviation of each point (0.7 µm) approximately equal to marker size. Dashed black line depicts results from COMSOL model up to full actuation (18 µs). Compression zone indicates when impact face is within the channel and may be compressing cells. Bracket demarcates the hold time of maximum compression. Arrows indicate motion of µHammer during impact and release.

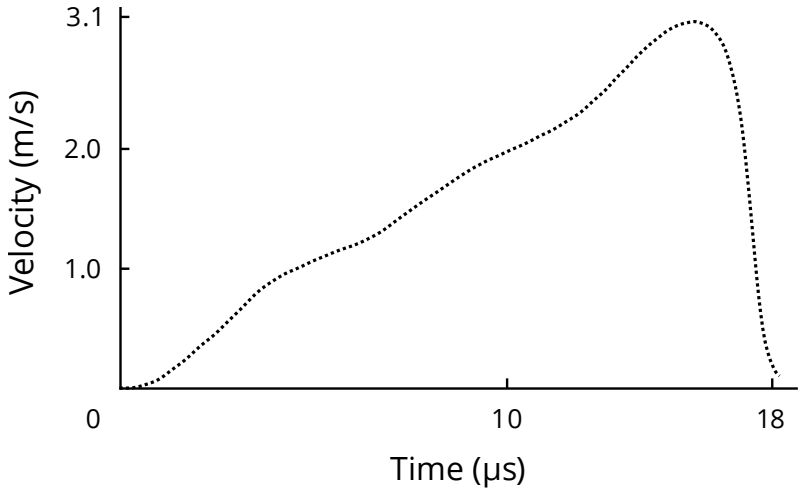

Figure 4.3: μHammer velocity profile. Data points generated via centered finite difference approximation of first numerical derivative of COMSOL simulation data in Figure 4.2. Velocity ranges from 2 to 3.1 m/s (2.6 m/s average velocity) while impact face is in channel (after 10 μs).

between batches. This changes the stiffness of the spring and thus the restoring force by up to 10%, resulting in approximately ±1-μs variation in the t_{SC} value for devices from different fabrication batches. To counteract these variations in t_{SC} and ensure consistent actuation across experiments, I used an external bar magnet to slightly modify the net magnetic force applied to the armature during actuation, which I describe in more detail in Appendix D.

4.2.2b First device generation

As shown in Figure 4.4, the surface of the first μHammer generation's impact face displayed an interference pattern during actuation, indicating that the μHammer impact assembly was rotating out-of-plane. This interference pattern changed over the course of actuation, demonstrating that the out-of-plane rotation was dynamic. Such a lack of stability suggests that the spring was too soft for the net force applied to the armature, resulting in an inconsistent actuation profile. Furthermore, the soft spring combined with the lack of pincers bounding the impact face in this design allowed the impact face to overshoot its intended final

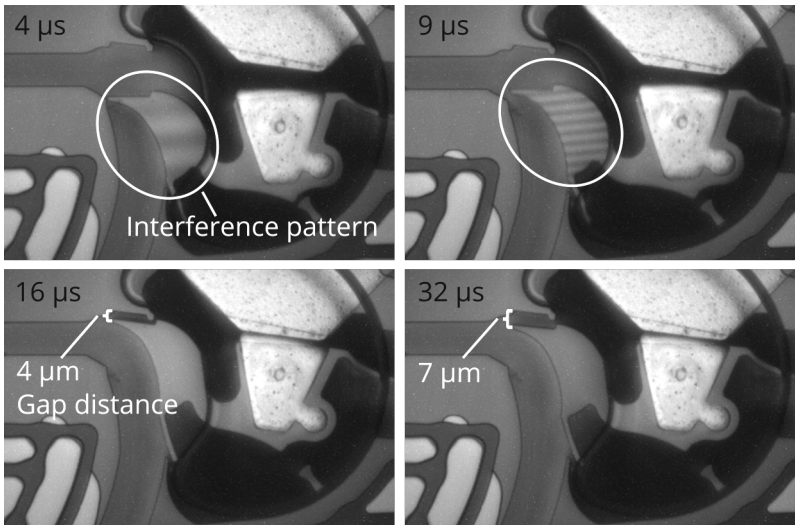

Figure 4.4: Strobed images of the first generation µHammer design as a function of time after solenoid activation. Note the dynamic interference pattern during actuation as the device was closing (4 µs and 9 µs), as well as the increase in gap distance with time after the device closed at 16 µs.

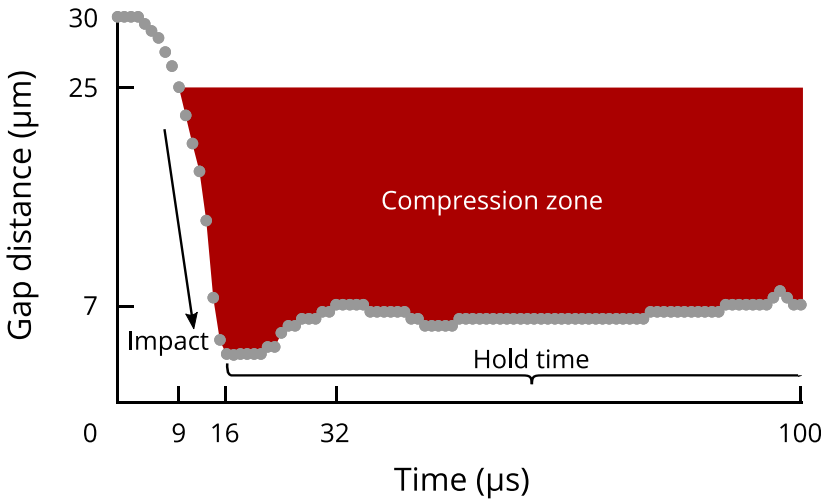

Figure 4.5: µHammer compression and recovery profile of first device generation. Grey points measured from strobed images of device without cells for 100 µs after actuation (maximum time allowed by software). Device reached its intended final gap distance of 7 µm at 14 µs but overshot it, closing to 4 µm at 16 µs before eventually returning to 7 µm at 32 µs. Note how device was still fully actuated and didn't begin to recover within 100-µs window, even though magnetic force generated by solenoid was removed at 20 µs. $N = 1$ device. Compression zone indicates when impact face is within the channel and may be compressing cells. Bracket demarcates hold time of maximum compression. Arrow indicates motion of µHammer during impact.

gap distance, x_G. It initially closed to a gap distance of 4 μm before eventually recovering to its intended x_G of 7 μm (Figures 4.4 and 4.5). Finally, the restoring force provided by the spring was too low to quickly return the impact assembly to rest after the actuation force was removed, remaining at full actuation for at least 80 μs without beginning to return to rest (due to software restrictions, I could only capture strobed images for 100 μs after the initialization of actuation and thus could not determine when the device actually began to recover). This diminished the throughput capabilities of the device and limited the user's control over the duration of impact, issues that were resolved by the increased spring stiffness of the current device generation as described in Section 3.3, resulting in the consistent actuation profile shown in Figure 4.2.

4.3 Characterization of μHammer hit severity parameters

In most explorations of external biological impacts to date (including *in vitro* and *in vivo* experiments and simulations), the three parameters that are altered to adjust hit severity are impact duration (hold time), impact depth, and impact velocity. In this section, I explore the values of these parameters that have been achieved with past device generations and that can be achieved in existing device generations, then discuss how to vary these parameters in the future. I conclude this section by using this information to estimate the compressive stresses experienced by cells during a μHammer impact.

The impact duration of the μHammer is determined by the amount of time the hold current is applied. Due to the vacuum-like seal between the Ni–Fe pole and armature, the existing design iteration of the μHammer maintains full compression 3 to 4 μs after the hold current is turned off (the first device generation, on the other hand, maintained full compression at least 80 μs after the hold current was turned off). Thus, the minimum impact duration is under

10 μs, whereas the maximum with the existing software is 1 ms, providing 2 orders of magnitude adjustment in this parameter.

The impact depth is determined by the final gap distance to which the cell is compressed, which as discussed in Chapter 3 is set by the height of the pincers on each end of the μHammer impact face. The device shown in Figure 4.1 has a 7.5-μm final gap, but devices with a 4-μm final gap have also been fabricated and used. The final gap distance, x_G, can easily be varied in future iterations. The impact depth determines the percent strain applied to the cell, which is unique for each cell due to variations in individual cell size. The larger final gap (7.5 μm) translates to ~50% strain for a 15-μm cell, and the smaller final gap (4 μm) translates to an ~75% strain.

Finally, the impact velocity of the μHammer during compression is determined by the net force applied to the μHammer. This device generation has been optimized for maximum impact velocity (2 to 3 m/s as shown in Figure 4.3). In the future, that range can be lowered through a decrease in the applied magnetic force from the solenoid or an increase in the restoring force from the spring. The easiest way to lower the magnetic force applied to the μHammer is by reducing the current applied to the solenoid. As shown in Table 4.2, I was able to halve the average actuation velocity of the first-generation thin spring design by decreasing the applied current from 5 to 3 A. However, the overall actuation profile with these settings was inconsistent since the device was operating in the exponential region of the current versus applied force curve (Figure 3.6a), instead of at saturation. A more sophisticated but resource-intensive approach would be to redesign the Ni–Fe pole geometry to lower the force applied at each current value (Figure 3.6a). This would come at the expense of the benefits of running at saturation though. A simpler and more effective approach is through

Table 4.2: μHammer impact velocity capabilities

Method	Range	Average	Strain Rate[a]
1st Gen Thin Spring Design (5-A DC)	1.0 – 4.3 m/s	3.0 m/s	200,000 s^{-1}
1st Gen Thin Spring Design (3-A DC)	0.5 – 2.2 m/s	1.3 m/s	80,000 s^{-1}
Existing Design (5-A DC)	2.0 – 3.1 m/s	2.6 m/s	170,000 s^{-1}
Existing Design (PWM)	0.5 – 1.6 m/s	1.1 m/s	70,000 s^{-1}
Thick Spring Redesign (5-A DC)	0.8 – 1.6 m/s	1.4 m/s	90,000 s^{-1}

[a]Strain rates based on average impact velocity for a 15 μm diameter cell.

pulse width modulation (PWM), which produces a square wave with the same amplitude as a direct current (DC), but with adjustable on and off times. Using this method to actuate the μHammer, I determined that the optimal t_{on} and t_{off} values for the slowest complete actuation of the μHammer were 2.6 μs and 0.5 μs, respectively. This resulted in compression velocities within the channel ranging from 0.5 to 1.6 m/s, as shown in Table 4.2.

If a further decrease in impact velocity is desired, the restoring force applied by the spring can also be adjusted in future iterations by simply increasing the spring width, *b*. I used a Nelder-Meade optimization algorithm in COMSOL coupled with the 2D time-dependent μHammer model to determine the thickest width capable of full actuation with the same steady-state magnetic force. The solution, 4.6 μm (20% wider than the existing spring), resulted in a range of velocities in the channel from 0.8 to 1.6 m/s (Table 4.2). However, making fine adjustments in the spring thickness can be tricky due to the batch variability of device fabrication discussed in Section 4.2.2a. To achieve the desired spring thickness and actuation velocity through this method, fabricating multiple devices in a single batch with a gradient of spring thicknesses is recommended.

While the impact duration, depth, and velocity of a μHammer impact comprehensively describe the loading conditions applied to each cell, quantifying the applied stress is also of

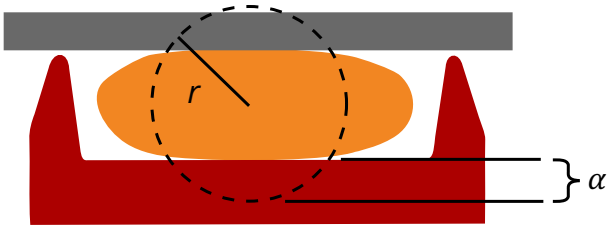

Figure 4.6: Hertz contact model parameters. Channel wall depicted in grey, deformed cell in orange, and impact face in red. Dashed line depicts undeformed cell with the radius, *r*, labeled. The distance of compression applied to one side of the cell, α, is also labeled.

interest. Under the operating conditions described in this manuscript, stress and strain are coupled. In the future, however, it may be possible to decouple these two parameters to explore their differential effect on the cellular response to impact. The force applied to each cell is difficult to quantify, since the stiffness of the silicon that makes up the spring (GPa) is orders of magnitude larger than the stiffness of the cells (~kPa [108]), making it nearly impossible to calculate the force dynamically. However, using a simple Hertz contact model between two parallel plates (used in most calculations of force in AFM and microplate cell compression studies [43, 92, 94, 109]), we can estimate the quasi-static pressure F (in Newtons) applied to the cell at maximum compression:

$$F = \frac{4E\sqrt{\alpha^3 r}}{3(1-\nu^2)},$$

where E is the Young's Modulus at that strain rate, α is half the total distance of compression (Figure 4.6), r is the initial (undeformed) radius of the cell, and ν is the Poisson's ratio. Although cell stiffness is difficult to quantify and no values have been reported at strain rates on the order of 100,000 s^{-1}, published trends in the viscoelastic behavior of cells and tissue indicate that an E value on the order of 10 to 100 kPa at such high strain rates is likely [43, 49, 80, 92, 94, 110]. Furthermore, it is commonly assumed that cells are incompressible with a Poisson's ratio, ν, of 0.5. Given these values, we can estimate a contact force between 0.1

and 10 μN depending on the applied strain and the stiffness of the cell, which translates to an applied stress between 1 and 100 kPa assuming a contact area on the order of 100 μm^2.

4.4 Characterization of μHammer timing

4.4.1 Methods

4.4.1a Overview of μHammer operation

In order to subject biological cells (or any other desired type of particles) to impact, they are first suspended in Tyto Running Buffer and loaded into a macroscale cartridge that interfaces the device with the MACSQuant Tyto system. In addition to the flow-controlled pump, solenoid actuation assembly, and alignment stages discussed in previous sections, the Tyto system also includes two laser-detector pairs (405-nm and 488-nm wavelength, 100-mW excitation lasers each paired with multiple filters for detection). Prior to entering the μHammer chip, each individual particle is pressure-driven through a focusing channel designed by Owl biomedical that has a variable cross-section as described by Foster et al. [111] (see Chapter 6 for further description of flow focusing in the μHammer). It then flows into and through the μHammer channel, where the particle is eventually sensed by the laser-detector pairs spaced 50 μm apart. These detectors measure either fluorescence or the backscatter signal that arises from reflection as the particle passes through the laser planes. The transit time between these lasers, t_{LL}, is measured and used to calculate the particle velocity, u (see Table 4.3 and Figure 4.7 for further explanations and illustrations of all timing parameters). The flow is controlled such that the average t_{LL} of the particle population is set to a user-specified value.

Table 4.3: μHammer experimental and timing parameters

Category	Variable	Parameter described	Definition
Setup	x_G	Final gap distance	Distance between impact face and upper channel wall after full actuation (fixed device parameter)
	x_{HF}	Hammer face width	Distance between pincers that bound impact face (fixed device parameter)
	x_{LH}	Laser-hammer separation distance	Distance between detecting laser and center of impact face (adjustable)
	x_{LL}	Intra-laser separation distance	Distance between detecting lasers (fixed system parameter)
Flow	t_B / t_V	Blue / violet laser detection time	Time that particle signal pulse is detected by blue (488 nm) and violet (405 nm) laser detector
	t_D	Detection time	Time that particle signal pulse is detected by final laser detector ($t_D = t_V$)
	t_{LL}	Intra-laser transit time	Time of transit between blue and violet lasers ($t_{LL} = t_V - t_B$)
	u	Particle velocity	Velocity of particle as detected by lasers ($u = x_{LL} / t_{LL}$)
Timing	t_{DS}	Solenoid trigger time	Time after particle detection that solenoid pulse triggers actuation ($t_{DA} - t_{SA}$)
	t_{DA}	Particle arrival time	Time after detection that particle is predicted to arrive at center of impact face ($t_{LL} \bullet x_{LH} / x_{LL}$)
	t_{SA}	Pre-arrival trigger time	Time before particle is predicted to arrive at μHammer that solenoid triggers actuation ($t_{SC} - t_{AC}$)
	t_{SC}	μHammer closure time	Time after solenoid trigger that μHammer fully actuates (varies between devices)
	t_{AC}	Post-arrival closure time	Time after particle is predicted to arrive at μHammer that it fully actuates ($t_{DS} + t_{SC} - t_{DA}$)
	t_{SD}	Post-trigger detection time	Time after solenoid trigger that next particle is detected (varies with distance between cells)
	x_C	Particle-center separation distance	Distance of impacted particle from center of impact face (varies based on accuracy of timing)

Throughout this work, two average particle velocities are used: "slow" velocity, u_S (1.2 to 1.3 m/s, $\overline{t_{LL}}$ = 40 μs), and "fast" velocity, u_F (2.3 to 2.7 m/s, $\overline{t_{LL}}$ = 20 μs). These velocities represent those typically used when operating the MACSQuant Tyto system for cell-sorting applications and correspond to flow rates of 4 ml/hr and 8 ml/hr (see Table 4.1 for pressure settings as a function of flow rate and temperature). The calculated particle velocity is used to predict the particle arrival time at the center of the μHammer face, t_{DA}, measured in relation

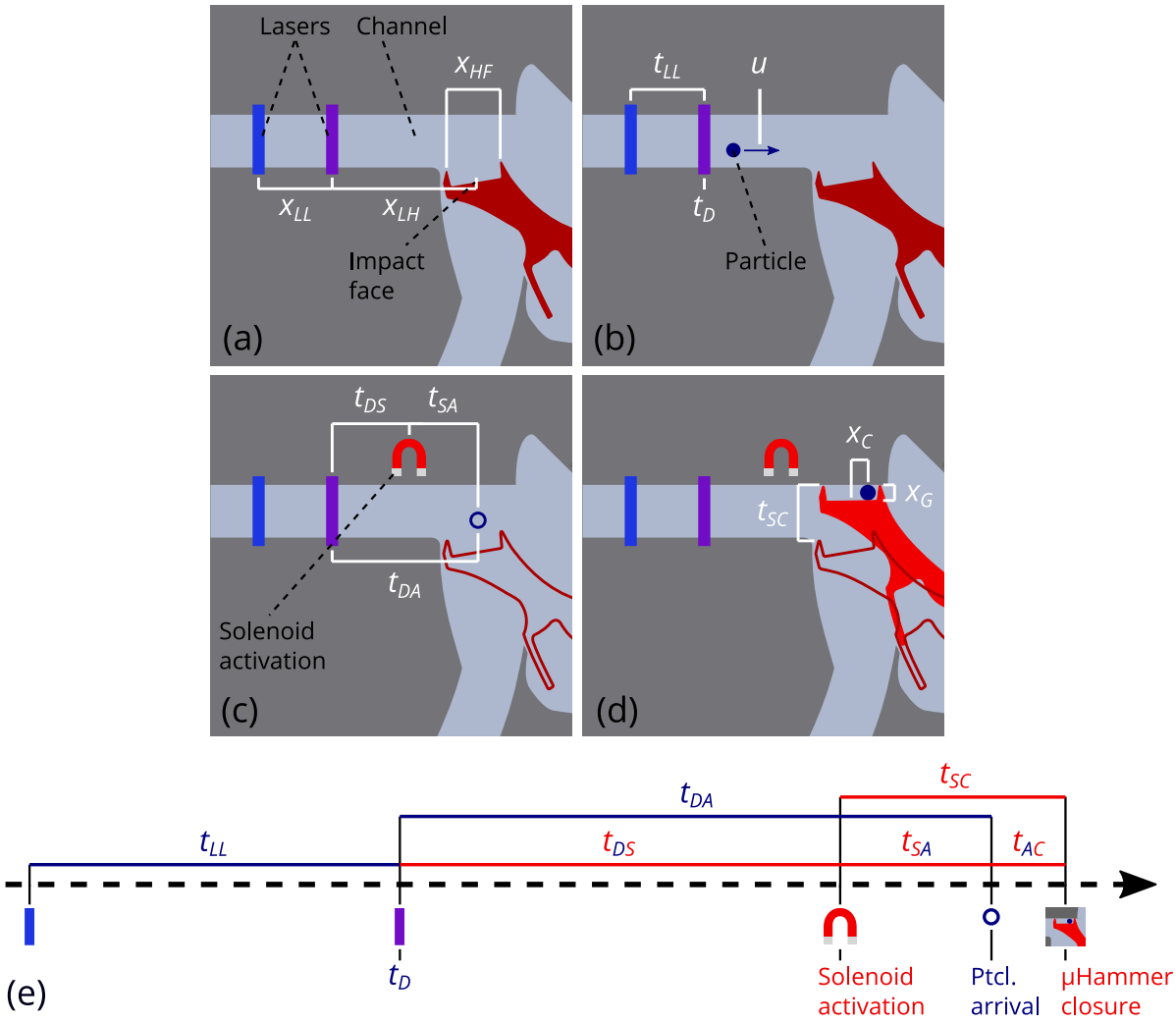

Figure 4.7: Illustrations of μHammer experimental variables from Table 4.3 overlaid on μHammer schematic as viewed from top of device. (a) Variables that define device dimensions related to experimental setup. Blue and violet laser-interrogation positions marked, along with channel and center of impact face. (b) Variables related to flow. Particle depicted travelling through channel. (c) Variables related to timing. Red magnet illustrates activation of external solenoid (not shown). Outlines of μHammer (dark red outline) and bead (dark blue outline) depict their predicted locations in the absence of device actuation. See Figure 6.4b inset for illustration of t_{SD}. (d) Variables relating to μHammer actuation and cell impact. μHammer before actuation depicted in dark red outline, μHammer at full actuation depicted in solid red. (e) Overall sequence of timing variables. Movement from left to right depicts the passage of time. Timing variables associated with the bead are depicted in dark blue, while variables associated with the solenoid activation and μHammer actuation are depicted in red.

to the time of detection by the final laser, t_D. This particle arrival time depends on the distance between the detecting laser and the center of the μHammer impact face, x_{LH}. To actuate the μHammer, the Tyto's external solenoid is activated with a 5-A DC current t_{DS} microseconds after particle detection at a predetermined amount of time before the particle is expected to arrive at the μHammer face, t_{SA}. The μHammer then completes actuation t_{SC} microseconds after the solenoid is actuated. To account for slight differences in t_{SC} between devices (±1 μs, see Section 4.2.2a for further discussion), we define our timing settings in terms of the pre-arrival closure time, t_{AC}. This value measures the amount of time after the particle is predicted to arrive at the center of the impact face that the μHammer completes actuation. When full actuation is reached, the amount of compression applied to each particle depends on the final gap distance, x_G, which is determined by the length of the pincers bounding the impact face. The particles are held in compression for a user-specified period that depends on the length of the hold current applied to the solenoid, after which they are released and the μHammer returns to rest in preparation for the next actuation.

4.4.1b Simulated characterization of μHammer timing

In order to determine the correct timing of actuation, I first simulated the trajectory of particles passing through the device using the two-dimensional COMSOL model introduced in Section 4.2.1. In addition to solving for fluid velocity and structural deformation, this model also traces the trajectory of particles suspended in buffer through the channel until contact with the μHammer impact face. For the calculation of particle trajectories, I modeled the drag force with the Schiller-Naumann (SN) drag law. Different drag laws are appropriate in different scenarios, determined in large part by the relative Reynolds number of particles flowing through the system:

$$Re_r = \frac{|\boldsymbol{v} - \boldsymbol{u}|\rho a}{\mu}$$

where $\boldsymbol{v}$ is the fluid velocity, $\boldsymbol{u}$ is the particle velocity, a is the particle diameter, ρ is the fluid density, and μ is the fluid dynamic viscosity. In the context of the µHammer, Re_r is on the order of 1 where the SN drag law is considered valid [112]. I used this COMSOL model to track the trajectories of 12- to 16-µm-diameter prototypical cells flowing through a 7.5-µm gap distance (x_G) device for u_S bead velocity settings at 37 °C. At a user-determined time, the device began to actuate across the channel as depicted in Figure 4.2. These simulations were performed for prototypical cells travelling both through the middle and along the edges of the µHammer channel to determine any variations in timing based on particle location across the channel.

To further explore the sensitivities of µHammer timing to changes in experimental conditions and to model subsequent experiments with microbeads, I used the same COMSOL model to simulate the trajectories of 6-µm particles during µHammer actuation for u_S bead velocity settings at both 8 °C and 37 °C. I performed these simulations with different t_{AC} values for both 4- and 7.5-µm gap distance devices, measuring the distance of the particle from the center of the impact face, x_C, when it first made contact with the µHammer. I also recorded the fluid velocity at the center of the particle at the time of initial contact to gain a more complete understanding of how actuation affects the flow of particles across the impact face.

4.4.1c Experimental characterization of µHammer timing

In order to characterize the µHammer's timing experimentally and validate the findings from simulation, I captured images of 6-µm-diameter Polybead® microbeads (Polysciences, Inc., USA) as they were held in compression following impact by a 4-µm final gap distance

device. These beads were suspended in buffer at the appropriate concentration to enable the detection and impact of 300 ± 50 beads/s (2.8×10^5 beads/mL for slow bead velocity, u_S, and 1.4×10^5 beads/mL for fast bead velocity, u_F). They were then strained with a 10-µm CellTrics filter (Sysmex Partec, Germany) and loaded into the µHammer cartridge. The beads were pressure-driven through the device and timed using backscatter signals generated with the 405- and 488-nm-wavelength lasers, as described in Section 4.4.1a. Once the beads were timed and impacted by the µHammer, they were held in compression for 200 µs and imaged by a Ximea MQ003MG-CM high-speed camera (Ximea, Germany). These images were taken at a rate of 10 Hz to gather data from a representative fraction of the total impacted bead population. Using image analysis software (ImageJ Version 1.50i, public domain), I classified the captured beads according to their position along the impact face. Beads found within 7 µm of either pincer were labeled "burst," while beads outside of these zones near the center of the impact face were labeled "centered." If no bead was found in the image, I applied the label "missing."

This assay was performed with different t_{AC} (post-arrival closure time) values for both u_S and u_F bead velocities, all at 37 °C with an x_{LH} (laser-hammer separation distance) of 80 µm. The results were used to determine the optimal t_{AC} values for both u_S and u_F settings based on the percentage of centered bead impacts. To determine how the measured bead displacement across the µHammer impact face (as a function of t_{AC}) compares to the expected bead displacement (as a function of u), I only imaged and analyzed beads within a small range of t_{LL} (intra-laser transit time) values in this assay (42 µs < t_{LL} < 45 µs for u_S, 23 µs < t_{LL} < 26 µs for u_F). For each t_{AC} value, 400 images were collected over the course of approximately 1 minute with the same µHammer device and analyzed.

4.4.2 Results

4.4.2a Simulated characterization of μHammer timing

Using the actuation profile and timing information from Figure 4.2, I decided to trigger the solenoid so that the μHammer completely actuates 3 to 4 μs after the cell is predicted to arrive at the center of the μHammer impact face (for a post-arrival closure time, t_{AC}, of 3 to 4 μs). As shown in Figure 4.8, the COMSOL model predicts that a 14-μm particle travelling down the center of the channel easily clears the pincer at the front of the μHammer impact face before contacting the face itself, 13 μs after ignition. Similar particle and impact face trajectories were obtained for all other cell diameters simulated between 12 and 16 μm, including cells flowing along the channel periphery (with a reduced velocity up to 30% slower than cells flowing through the center due to the parabolic decay of fluid velocity from the center of the channel, Figure 4.9). These cells all cleared the μHammer's front pincer before contacting its impact face, though the time and thus location of initial contact varied based on the distance of the edge of the cell from the impact face prior to actuation (cells closer to the impact face made contact with it sooner and thus further upstream). This confirms that cells are present in the μHammer compression zone concurrently with the impact face. However, it should be noted that larger cells travelling along the periphery narrowly cleared the front pincer before contacting the impact face in these simulations. As a result, using cells larger than 16 μm with the current device generation is not recommended due to their high probability of being sheared by the pincers.

In order to further investigate the sensitivity of μHammer timing to changes in experimental parameters and provide a model for later experiments with microbeads, I used the COMSOL model to simulate impacts of 6-μm particles with different t_{AC} (post-arrival

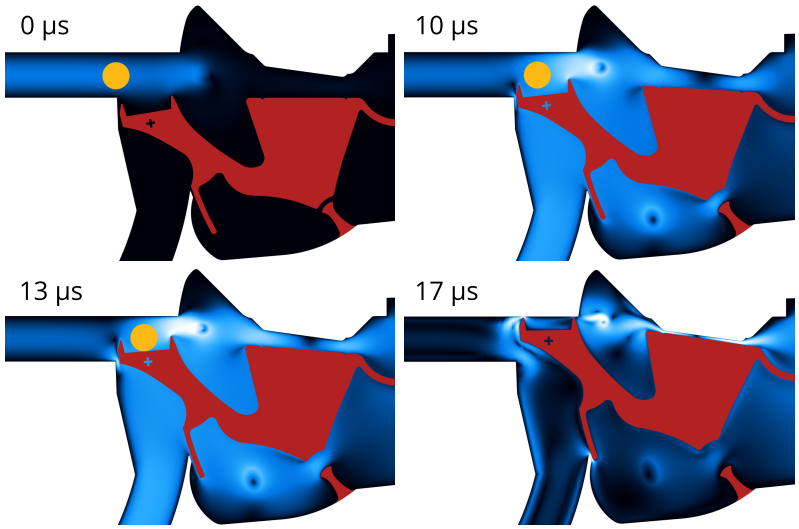

Figure 4.8: Images of 2D COMSOL time-dependent model of 14-µm cell impact. Images depict cells (in orange) impacted by 7.5-µm final gap distance device (in red) for *us* bead velocity settings at 37 °C. Timepoints chosen reflect when external solenoid (not shown) is triggered for impact (0 µs), µHammer impact face enters channel (10 µs), first makes contact with cell (13 µs), and fully compresses cell (17 µs). Dark blue-to-white gradient depicts flow rates ranging from 0 to 10 m/s, respectively (average cell velocity: 1.25 m/s). Cell locations are calculated by model, up to contact with impact face (13 µs).

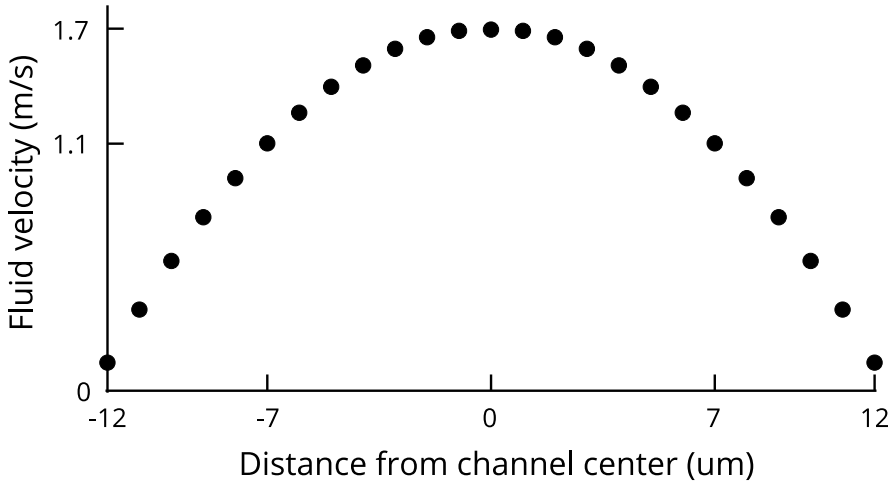

Figure 4.9: The fluid velocity in the µHammer channel decays parabolically from the channel center. Plot depicts fluid velocity from 2D COMSOL simulation as a function of distance from the center of the channel across its 25-µm width. Note the ~30% decrease in fluid velocity 7 µm from the channel center.

closure time) values. For each t_{AC} setting, I determined both the fluid velocity at the center of the particle as well as the distance of the particle from the center of the impact face, x_C, when the particle first made contact with the μHammer. Furthermore, I classified particles that first contacted the impact face within 7 μm of either pincer as "burst," since cells larger than 14 μm impacted within these zones are likely burst by the pincers as discussed in Chapter 3. Particles contacted outside these zones near the center of the impact face were labeled "centered," while particles that first made contact with the pincers or did not contact the impact face at all were eliminated from the dataset.

As shown in Figure 4.10a, the optimal t_{AC} value for u_S settings at 37 °C with the 4-μm gap distance device was 3 μs, consistent with the simulations above with larger particles. The data in this plot was obtained using particles travelling offset from the center of the channel (bead center 5.5 μm from the channel wall closest to the μHammer impact face at rest, 7 μm from the channel center as shown in Figure 4.11a) with a velocity of 1.15 m/s before actuation. For particles travelling down the center of the channel with a higher velocity (1.7 m/s, data not shown), the optimal t_{AC} value was 2 μs due to the increased distance between the impact face and the particle before impact. Changing the temperature to 8 °C, on the other hand (data not shown), had no effect on the optimal timing. As shown in Figure 4.10a, there were a total of 5 t_{AC} values that resulted in the particles initially contacting the impact face in the centered region, and 2 that initially made contact in the burst region. Furthermore, there was a clear trend of increasing fluid velocity at the center of the particle at contact as the t_{AC} value (and thus the x_C value) increased. All of the fluid velocity values at contact were larger than the initial velocity of the fluid at the center of the particle before entering the impact region (1.15 m/s). This indicates that the particle velocity increases dramatically as it crosses the

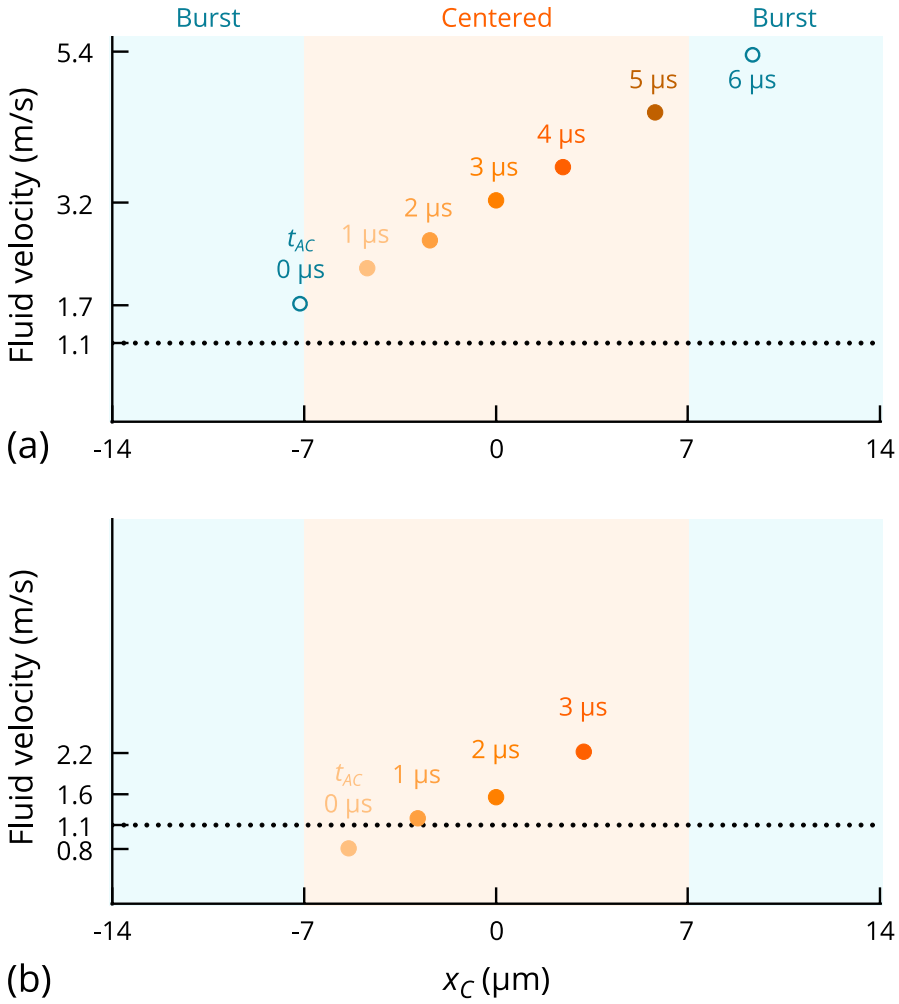

Figure 4.10: The impact location and fluid velocity at contact vary with timing changes in COMSOL model. Each point represents a different t_{AC} value, plotting the fluid velocity at the center of the particle as well as the bead-center separation distance, x_C (illustrated in Figure 4.11b), both measured when the particle first contacts the impact face. Simulations performed with particles offset from the center of the channel traveling with u_S particle velocity settings at 37 °C (a) Results from simulations with a 4-µm final gap distance device. (b) Results from simulations with a 7.5-µm device. In both plots, the two outer quadrants (shaded blue, 7 µm < $|x_C|$ < 14 µm) correspond to the "burst" region, and the two inner quadrants (shaded orange, $|x_C|$ < 7 µm) correspond to the "centered" region. Only t_{AC} values that resulted in particles clearing pincers and making contact with the impact face are shown. Centered t_{AC} values in which particles first contact the impact face in the centered region are depicted by filled orange circles, while burst t_{AC} values are depicted by open blue circles. The maximum and minimum fluid velocities at impact are marked, as well as the fluid velocity for the optimal t_{AC} value (x_C = 0). Dashed line indicates fluid velocity at center of particle before entering the compression zone.

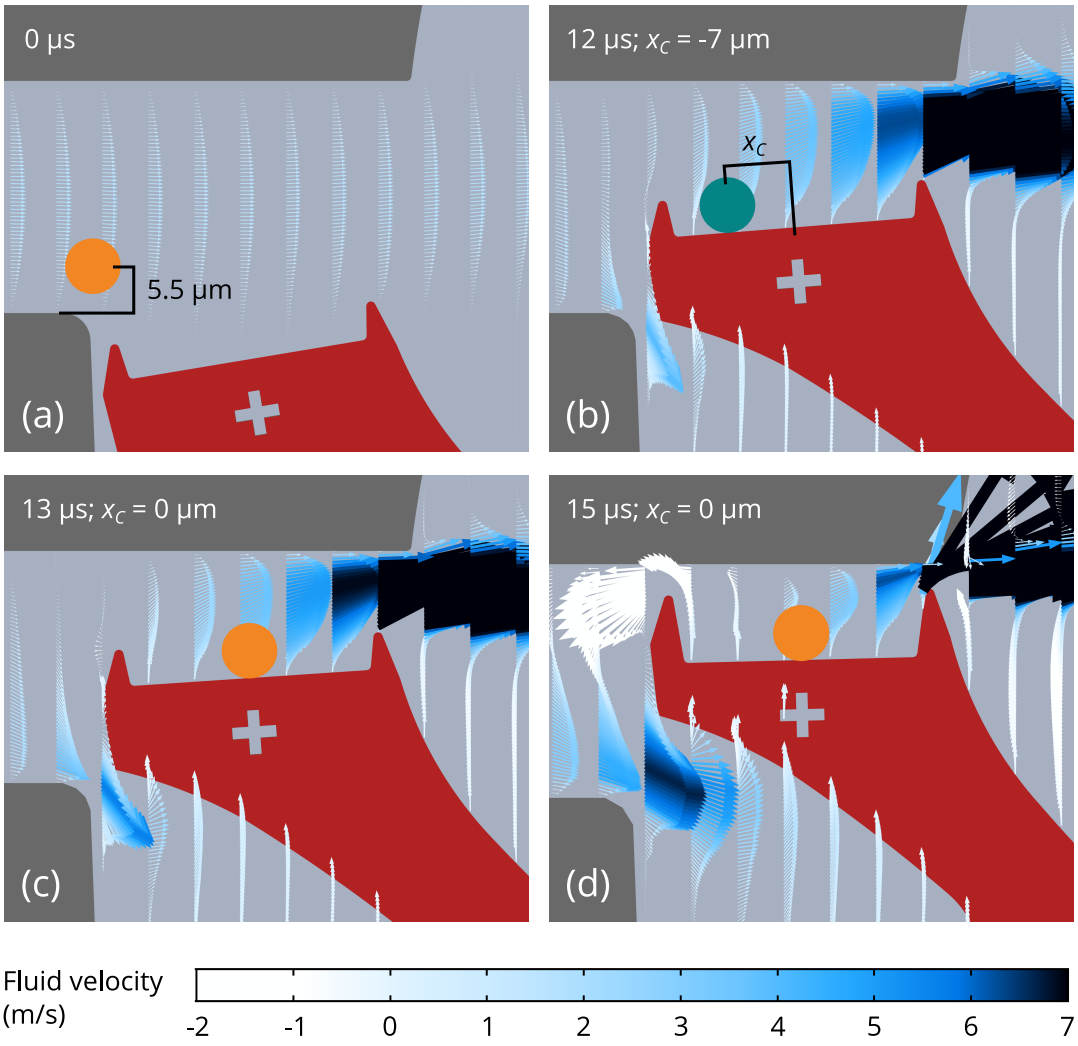

Figure 4.11: COMSOL simulations of 6-µm particle impact. (a) Particle (in orange) location when actuation begins. Distance of particle from channel wall (in dark grey) marked. (b) Burst particle (in blue) impact by 4-µm gap final distance device with t_{AC} = 0 µs. Particle first makes contact with impact face (in red) 12 µs after solenoid ignition. Distance of particle from center of impact face, x_C, marked. (c) Centered particle impact by 4-µm final gap distance device with t_{AC} = 3 µs. Particle first contacts impact face 13 µs after solenoid ignition. (d) Centered particle impact by 7.5-µm final gap distance device with t_{AC} = 2 µs. Particle contacts impact face 15 µs after solenoid ignition. In each panel, arrows denote direction of flow, with x-component of fluid velocity denoted by white to blue gradient (Note: gradient is inverted from Figure 4.8).

impact face. The increase in fluid velocity that supports this hypothesis is illustrated in Figures 4.11b and 4.11c, which show that the fluid velocity changes from 0 to over 7 m/s across the

width of the impact face.

For 7.5-µm gap distance devices, on the other hand, the optimal t_{AC} value was 2 µs for 6-µm particles flowing through the channel offset from the center (5.5 µm from the channel wall nearest the impact face at rest), 1 µs less than for the 4-µm gap distance devices (Figure 4.10). There were only 4 total t_{AC} values that resulted in particles contacting the center of the impact face (Figure 4.10b), while the rest of the t_{AC} values resulted in particles being caught by the pincers before touching the impact face or being missed completely. Furthermore, as shown in Figure 4.11d, the particles did not contact the impact face with optimal t_{AC} settings until 15 µs after solenoid ignition, 2 µs later than with the 4-µm gap distance device (Figure 4.11c). These differences are due to the recessed impact face and the longer pincers compared to the 4-µm device, which means the impact face has a longer distance to travel before it reaches the compression zone. As a result, the pincers are more likely to catch the particles before they reach the impact face. These longer pincers also diminish the magnitude of the velocity increase across the impact face (Figure 4.10b), essentially forming a pocket that decreases the velocity of the fluid between the pincers compared to the surrounding fluid (Figure 4.11d).

4.4.2b Experimental characterization of µHammer timing

Once I gained a sense of the appropriate timing of µHammer impact through simulation, I sought to characterize it more fully through experiment. The most direct way to do this would be to image biological cells as they are held in compression following impact. However, cells are optically transparent and highly deformable, and thus are difficult to image clearly through the depth of the channel. To obtain sharper images that are easier to analyze, I used 6-µm-diameter polystyrene beads instead. This particular bead size was chosen because beads larger than 6 µm become wedged between the tapered Ni–Fe poles and prevent actuation. Only rigid

particles like polystyrene beads experience this form of clogging, since larger viscoelastic particles like cells can easily pass between the Ni–Fe poles unperturbed. Furthermore, the 6-µm beads were chosen because they are larger than the 4-µm final gap distance under full compression, x_G (7.5-µm devices had a final gap size larger than the beads and thus were not used). As a result, the µHammer pincers do not close all the way but are held 1 to 2 µm from the channel wall by the rigid beads (Figure 4.12a), ensuring that the beads are immobilized between the µHammer face and the channel wall during compression. This allows one to determine the position along the µHammer face where the beads were impacted. Beads found within 7 µm of either pincer were labeled "burst," since cells larger than 14 µm impacted within these zones are likely burst as discussed in previous sections. Beads outside these zones near the center of the impact face were labeled "centered," while images with no bead visibly present were labeled "missing."

In order to determine the optimal t_{AC} values that result in the highest percentage of centered beads, I impacted beads with different t_{AC} values for both u_S and u_F bead-velocity settings. As shown in Figure 4.12b, three t_{AC} values resulted in finding a majority of beads in the centered region (orange, with t_{AC} = 3 µs being optimal in agreement with COMSOL simulations) for u_S settings. By comparison, five t_{AC} values resulted in a majority of beads being found in the burst region (blue). This indicates there is a preference for the beads to end up along the edges of the impact face near the pincers, which may be due to the displacement of fluid toward the edges of the µHammer during actuation. Furthermore, given the bead velocity measured by the lasers before actuation, u (1.1 to 1.2 m/s), it should take ~24 µs for the beads to "walk" across the width of the µHammer impact face, x_{HF} (28 µm). However, it only took a 7-µs change in t_{AC} values for the majority of beads to traverse this distance (Figure 4.12b). This

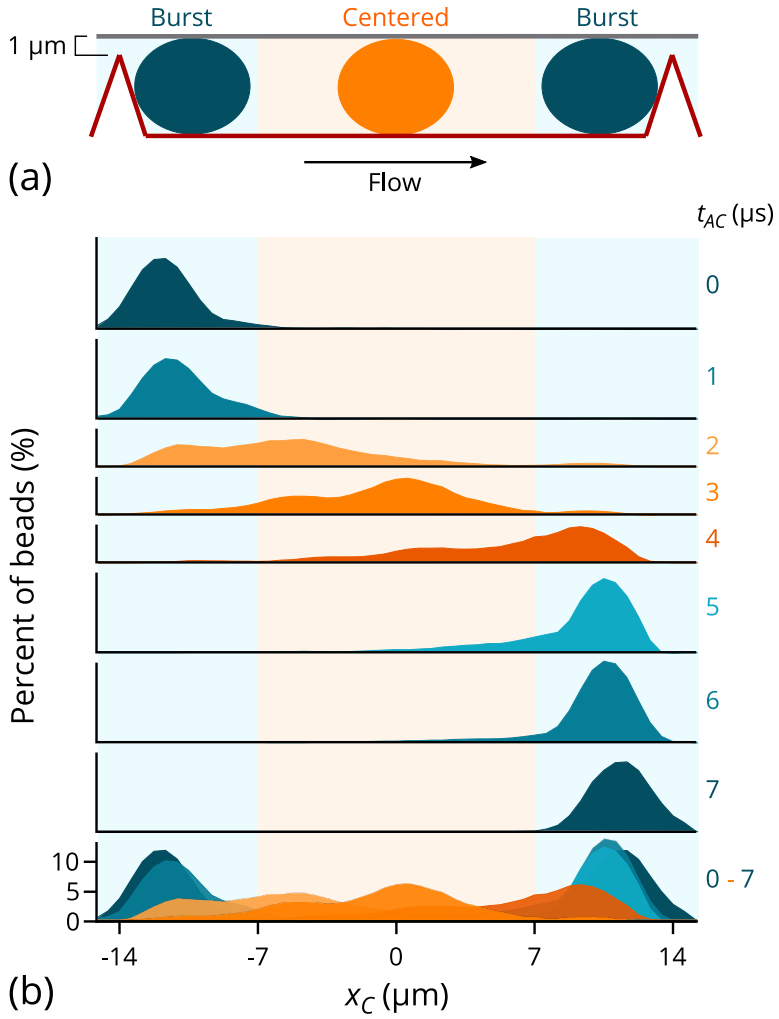

Figure 4.12: (a) Schematic of μHammer face while impacting beads. μHammer impact face (shown in red outline) scaled to match x-axis of panel b. Beads shown being impacted in the burst and centered regions, shaded blue and orange, respectively. Distance between channel wall and μHammer pincers labeled. Flow direction marked. (b) Histograms of bead-center separation distance, x_C, for slow bead velocity, u_S, as a function of post-arrival closure time, t_{AC}. Each histogram corresponds to a different t_{AC} value. In both panel a and b, the two outer quadrants (7 μm < | x_C | < 14 μm) correspond to the "burst" region, and the two inner quadrants (| x_C | < 7 μm) correspond to the "centered" region. Blue histograms correspond to t_{AC} values that result in the majority of beads being impacted in the burst region, while orange histograms correspond to t_{AC} values that result in the majority of beads being impacted in the centered region. Only t_{AC} values that result in less than 50% of beads being labeled as missing are shown. $N = 400$ images analyzed for each t_{AC} value. Histograms created with a bin width of 0.6 μm and lightly smoothed with a Savitsky-Golay filter averaging 4 values on each side.

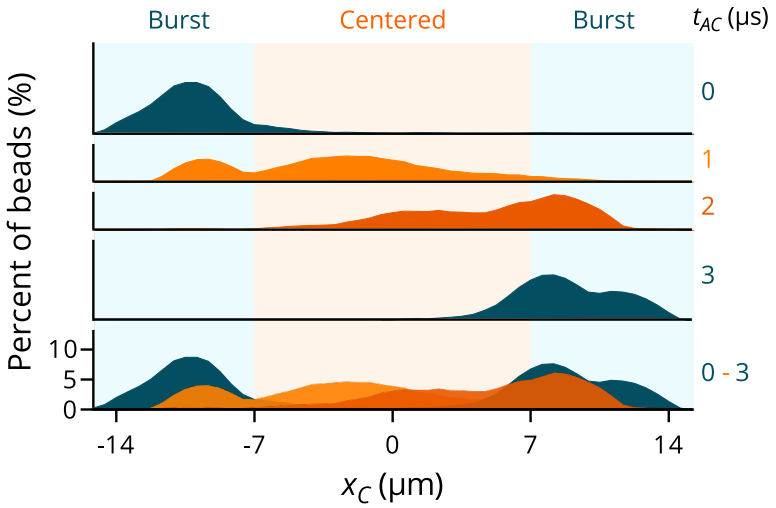

Figure 4.13: Histograms of x_C for fast bead velocity, u_F, as a function of t_{AC}. Each histogram corresponds to a different t_{AC} value. The two outer quadrants (7 µm < | x_C | < 14 µm) correspond to the "burst" region, and the two inner quadrants (| x_C | < 7 µm) correspond to the "centered" region. Blue histograms correspond to t_{AC} values that result in the majority of beads being impacted in the burst region, while orange histograms correspond to t_{AC} values that result in the majority of beads being impacted in the centered region. Only t_{AC} values that result in less than 50% of beads being labeled as missing are shown. N = 400 images analyzed for each t_{AC} value. Histograms were created with a bin width of 0.6 µm and were lightly smoothed with a Savitsky-Golay filter averaging 4 values on each side.

indicates that the average bead velocity increases while the µHammer actuates. A similar trend was found for u_F settings (Figure 4.13), which had only two t_{AC} values that resulted in a majority of centered beads and two values that resulted in a majority of burst beads. This decrease in both total and centered t_{AC} values is likely due to the higher average bead velocity compared to u_S settings, which reduces the amount of time beads are in the impact region and thus decreases the safety factor for error in timing.

4.4.3 Discussion

Overall, there is good agreement in the timing characterization results between simulation and experiment. This indicates the optimal t_{AC} (post-arrival closure time) value that will result

in the greatest number of centered impacts is approximately 3 μs for slow bead-velocity settings, u_S, and 1 μs for fast bead-velocity settings, u_F, regardless of the experimental temperature. Furthermore, both simulation and experiment demonstrate that the fluid and thus the particle velocity increase significantly in the compression zone during actuation.

Despite the general agreement between simulation and experiment, however, there were a couple of discrepancies that are important to discuss. First, the two-dimensional COMSOL simulations with a 4-μm final gap distance device (Figure 4.10a) resulted in a narrower spread of particle impact locations, x_C, as a function of t_{AC} than experiments with polystyrene beads (Figure 4.12b). As a result, these simulations predicted that a total of 5 t_{AC} values would result in a majority of particles being impacted in the centered region, in contrast with the 3 centered t_{AC} values observed experimentally. This difference in bead trajectory across the impact face is potentially due to the method of particle velocity calculation in the COMSOL model. When cells and other particles travel through the μHammer channel, each particle's velocity is determined by the fluid velocity across the entire surface area of that particle. In the COMSOL model, however, the particle velocity is only determined by a point calculation of the fluid velocity at the center of the particle and does not take the rest of the particle's surface area into account. Thus, the changes in fluid velocity across the μHammer impact face are likely to have an even greater effect on particle velocity than the model suggests, indicating the importance of experiments to validate the predictive power of these simulations. This is particularly true in the case of the COMSOL simulations with 7.5-μm final gap distance devices, which indicate a slightly different optimal timing than with 4-μm devices (t_{AC} = 2 μs vs 3 μs, respectively). Preliminary experiments with 7.5-μm devices have not yet confirmed

this, necessitating further experiments to determine if there are any noticeable differences in timing between these two device designs.

In addition to the experiments discussed above, I also performed preliminary experiments analyzing the impact of all beads regardless of their measured velocity, u (as opposed to beads within a narrow range of measured velocities like the experiments presented in Figures 4.12b and 4.13). These were performed with 6-µm polyester beads and 4-µm final gap distance devices, resulting in approximately the same optimal t_{AC} values already reported for both u_S and u_F bead-velocity settings. However, they did indicate that up to 4 t_{AC} values can result in a majority of centered impacts for u_S settings in a given device (compared to the 3 t_{AC} values shown in Figure 4.12b), and that only 1 to 2 t_{AC} values result in a majority of centered impacts for u_F settings (compared to the 2 t_{AC} values shown in Figure 4.13). These discrepancies are due in part to the low resolution of control over t_{AC} values (±1 µs), which makes it difficult to fully optimize timing for every µHammer device. However, they also likely reflect the slight differences in timing for particles travelling through the center as opposed to the edges of the channel, as predicted by COMSOL simulations with u_S settings (t_{AC} = 2 µs vs 3 µs, respectively). The beads impacted in the experiment presented in Figure 4.12b had a controlled velocity between 1.1 and 1.2 m/s, likely consisting of particles travelling offset from the center of the channel. This hypothesis is supported by the fact that the fluid velocity in the µHammer channel decays parabolically from its center, decreasing from the maximum velocity of 1.7 m/s to the measured particle velocity of 1.1 m/s approximately 7 µm from the center with u_S settings (Figure 4.9). Thus, particles travelling through the center of the channel could have slightly different optimal t_{AC} values than those travelling along the edges, thereby expanding the range of optimal t_{AC} values for the overall population.

Chapter 5. Device Implementation

5.1 Introduction

To demonstrate the efficacy of the μHammer in applying sublethal impacts to large populations of cells, my collaborators and I used immortalized human myelogenous leukemia K562 cells (ATCC, USA) as a model cell type. These cells have an average diameter of 14.3 ± 2 μm as determined by phase microscopy (N = 38 cells from 4 different experiments). In each of the following experiments, K562 cells were flowed through the μHammer channel, timed, and subsequently impacted. The impact depth (amount of strain applied) and duration (hold time of maximum strain) varied between assays, whereas a similar impact velocity was used in all experiments (2 to 3 m/s, see Figure 4.3). After being subjected to impact, cells were then extracted from the device and processed for analysis. In this chapter, I describe how I validated the optimal timing of solenoid activation for cell impact (predicted in Chapter 4) by quantifying the percentage of cells that were still intact following impact as a function of timing. I then discuss how my collaborators and I used these optimal timing settings to assess whether a μHammer impact has any effects on K562 cell viability, as determined through analysis of their membrane integrity, commitment to apoptosis, and subsequent proliferation.

5.2 Validation of μHammer timing with K562 cells

5.2.1 Methods

5.2.1a K562 cell culture

K562 cells, an immortalized human myelogenous leukemic cell line (ATTC, USA), were cultured according to vendor recommendations. Cells were grown in RPMI-1640 media

(Fisher Scientific, USA) supplemented with 10% FBS, 25 mM HEPES, and 0.01% penicillin streptomycin (Lonza Biologics, UK) at 37 °C and 5% CO2. Cells were seeded at 100,000 cells/mL and subcultured once cell density reached 1,000,000 cells/mL. Cell density was measured by analyzing 20-µL aliquots of cell suspension with the MACSQuant® Flow Cytometer (Miltenyi Biotech, Germany).

5.2.1b K562 cell impact

In order to validate the optimal timing of µHammer impacts described in Chapter 4, I sought to characterize timing efficacy as a function of the pre-arrival closure time, t_{AC}, using cells instead of polystyrene beads. I performed these experiments with both the 4-µm and 7.5-µm final gap distance devices at a temperature of 8 °C using u_F cell velocity settings. The overall protocol for µHammer timing and impact is described in detail in Chapter 4. Briefly, K562 cells were suspended in Tyto Running Buffer at a concentration of 2.0×10^5 cells/mL. They were then passed through a 20-µm Pre-Separation filter (Miltenyi Biotec, Germany) to remove large cells or other particles before being transferred to the input chamber of the µHammer cartridge (Figure 5.1). Subsequently, the cartridge was loaded into the Tyto experimental system, which (in addition to all of the components described in previous chapters) has a magnetic propeller that mixes the input chamber at 800 rpm for 1 minute every 10 minutes to keep the solution well mixed. To achieve a consistent magnetic field strength and ensure lasers were aligned with the microfluidic channel over the course of an experiment, the stationary solenoid and lasers were aligned with landmarks on the µHammer device as described in Section 3.4, maintaining a laser-hammer separation distance (x_{LH}) of 120 µm. This alignment was checked and maintained to within ±5 µm every 30 seconds by the Tyto's feature tracking software and motorized stages. Once the cartridge was loaded and aligned,

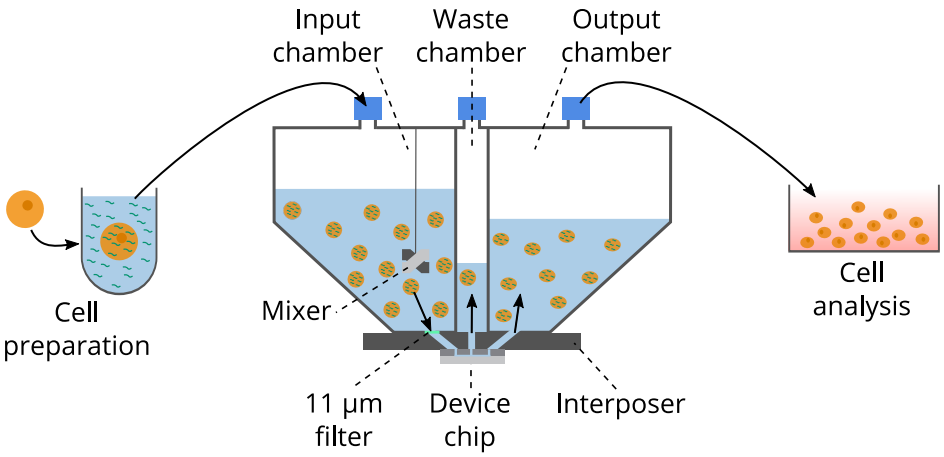

Figure 5.1: K562 cell impact overview. Cells are stained with fluorescent markers (optional) and suspended in buffer to prepare them for impact. They are then injected into the input chamber of the cartridge which is subsequently loaded into the MACSQuant Tyto (not shown). While in the input chamber, they are mixed by a magnetic propeller before being pressure driven through an 11-µm filter through the interposer into the device chip. Cells in the device are either sorted into the waste chamber or impacted and flowed into the output chamber, where they are ultimately extracted from the device for continued culture or analysis. Note: illustration is not drawn to scale and depicts side view of cartridge and µHammer device chip.

the pump applied positive pressure (700 to 800 mbar) to flow cells through an 11-µm filter and subsequently through the input via into the device, where they passed through the channel with u_F velocity settings (average population velocity of 2.3 to 2.7 m/s). Each cell's velocity was monitored by two laser-detector pairs which measured the backscatter generated by each cell as it passed through the laser plane, allowing the Tyto software to predict the cell's time of arrival at the center of the impact face. Using this information, the software was able to trigger the solenoid so that µHammer closed a user-determined amount of time after the cell was predicted to arrive at the impact face, t_{AC}. Once the µHammer impact assembly reached full actuation, it was held there for a user-specified period (20 µs for this particular experiment) before the solenoid was turned off. This allowed the µHammer to return to rest, releasing the impacted cell if the timing was successful (see Figure 5.2 for example of an ideal

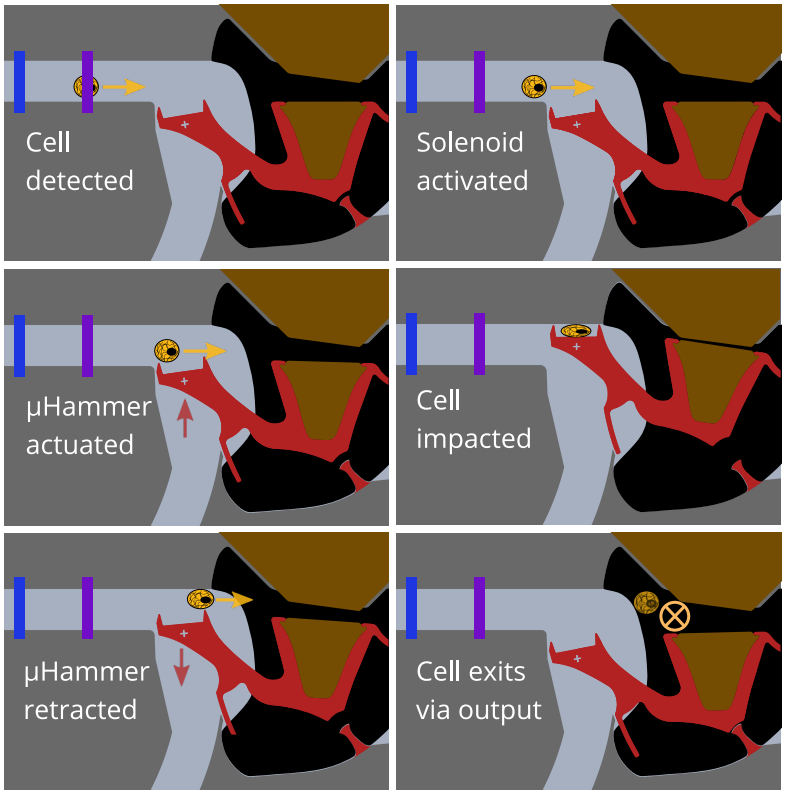

Figure 5.2: Timeline of successful µHammer impact. Cells (in orange) suspended in buffer enter µHammer channel through input via (not shown). They then flow through the channel where they are detected by laser-detector pairs (in blue and violet), which calculate the cell velocity and determine the appropriate time for the solenoid to trigger µHammer actuation. Once the cells enter the compression zone they are impacted by the µHammer (in red) against the wall of the channel (in dark grey), where they are held for a user-determined amount of time. After the solenoid is turned off, the µHammer retracts and the cell is released, allowing the cell to enter the output via (in black) and flow into the page to the output chamber of the µHammer cartridge. Cell motion is depicted with an orange arrow, and motion of µHammer is indicated with a red arrow.

impact sequence). Once released, the impacted cell flowed into the via underneath the Ni–Fe armature and out of the device chip, ultimately arriving in the cartridge's output chamber where it was extracted for analysis.

In cases where the timing wasn't successful, one of a few potential scenarios occurred. If the timing was off by a moderate amount, the cell was caught by the pincers and likely burst as shown in Figure 3.2. If the timing was significantly too early, the cell was "sorted" into the

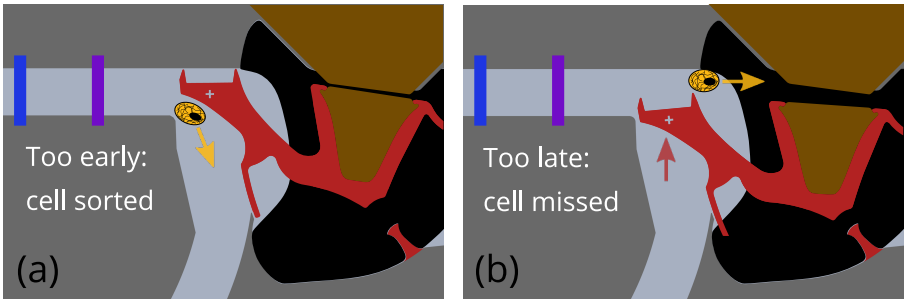

Figure 5.3: Illustration of significantly mistimed µHammer impacts. Orange arrows depict motion of cell, and red arrows depict motion of impact assembly. (a) When the µHammer actuates too early, cells are diverted (sorted) into the channel beneath the µHammer impact face at rest. They then flow through this channel into the waste via (not shown) and ultimately out of the device into the waste chamber of the cartridge. (b) When the µHammer actuates too late, cells flow through the channel past the impact face into the output via (in black) and ultimately the output chamber of the cartridge without being subjected to a µHammer impact.

waste via and out of the device into a separate chamber of the cartridge (Figure 5.3a). If the timing was significantly too late or if the cell was travelling too fast, then the cell passed by the µHammer impact face and out of the device into the output chamber without being subjected to a µHammer impact (Figure 5.3b).

In order to quantify the range of outcomes as a function of the solenoid activation timing, I impacted approximately 1×10^5 cells over the course of 5 minutes for each t_{AC} value tested and extracted the suspended cells from both the output and waste chambers. I then measured the cell density by analyzing 50-µL aliquots of the samples from each chamber with the MACSQuant Flow Cytometer. The fraction of cells that were sorted, P_s, and burst, P_b, were determined with the following equations:

$$P_s = \frac{\rho_w V_w}{\rho_i V_i};\ P_b = 1 - \frac{\rho_w V_w + \rho_o V_o}{\rho_i V_i}.$$

In these equations, ρ_i is the density of suspended cells that entered the device from the input chamber, ρ_w is the density of cells extracted from the waste chamber, and ρ_o is the density of

cells extracted from the output chamber, while V_i, V_w, and V_o are the volumes of each of these groups. This experiment was performed once with a 4-µm and once with a 7.5-µm gap distance device, for a total of two different devices.

5.2.2 Results and discussion

Using this procedure, I was able to successfully impact cells as they flowed through the µHammer channel suspended in buffer and thereby validate the optimal timing settings discussed in Chapter 4 (see Appendix C for analysis of device lifecycle during cell-impact experiments). As shown in Figure 5.4, I was able to capture images of cell impacts (held in compression for 200 µs) with a Ximea MQ003MG-CM high-speed camera. However, due to the deformability and opacity of the cells, it was difficult to accurately categorize cell impacts as burst, centered, or missing through the depth of the channel using visualization alone. Thus, to supplement this information, I used flow cytometry to compare the number of cells extracted from the output and waste chambers after impact to the number of cells that flowed into the device from the input chamber. Although this comparison does not directly indicate the percentage of cells that were centered on the impact face during compression, it does provide the information necessary to determine the number of cells that were missing from the population after impact (and thus classified as "burst"), as well as the number of cells that were "sorted" into the waste chamber through early actuation (Figure 5.3a). I could then infer that the remaining cells in the output chamber were successfully impacted by the µHammer (or missed completely if the timing of actuation was significantly late, Figure 5.3b). In order to ensure that all sorted cells ended up in the waste chamber, I performed the experiment with the higher flow rate of u_F cell velocity settings, since cells sorted with a lower flow rate (e.g. u_S settings) occasionally got stuck in the waste via and didn't emerge into the waste chamber

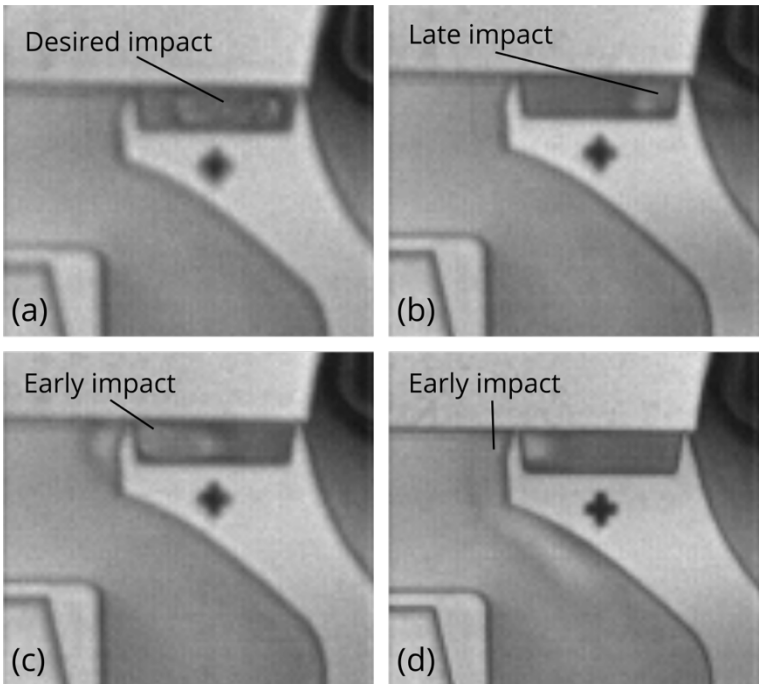

Figure 5.4: Micrographs of µHammer impacts with a 7.5-µm gap distance device. (a) Example of centered impact. Note how entire cell is contained within the compression zone and is not pinched by pincers bounding the impact face. (b) Example of burst impact resulting from late µHammer actuation. Note how only a small part of the cell is contained within the compression zone. (c) and (d) Examples of burst impacts resulting from early µHammer actuation. Note how most of the cell in panel c is contained in the compression zone, while most of the cell in panel d is outside the compression zone and stretched into the waste via. This indicates that the cell remnants from panel c end up in the outlet chamber while the remnants from panel d end up in the waste chamber. However, cells in panels b through d are all pinched by the µHammer pincers and likely burst, and thus do not affect the purity of the impact parameters applied to the analyzed hit cell population.

(leading to an inflated measurement of burst cells). Following impact, I determined the percentage of burst and sorted cells for each t_{AC} (post-arrival closure time) value tested to determine the optimal impact timing with both 4-µm and 7.5-µm gap distance devices.

As shown in Figure 5.5a, the t_{AC} value that resulted in the highest percentage of cells burst with a 4-µm gap device was -3 µs. As the t_{AC} value decreased below -3 µs, the percentage of cells burst began to decrease while the percentage of cells sorted began to increase. Since

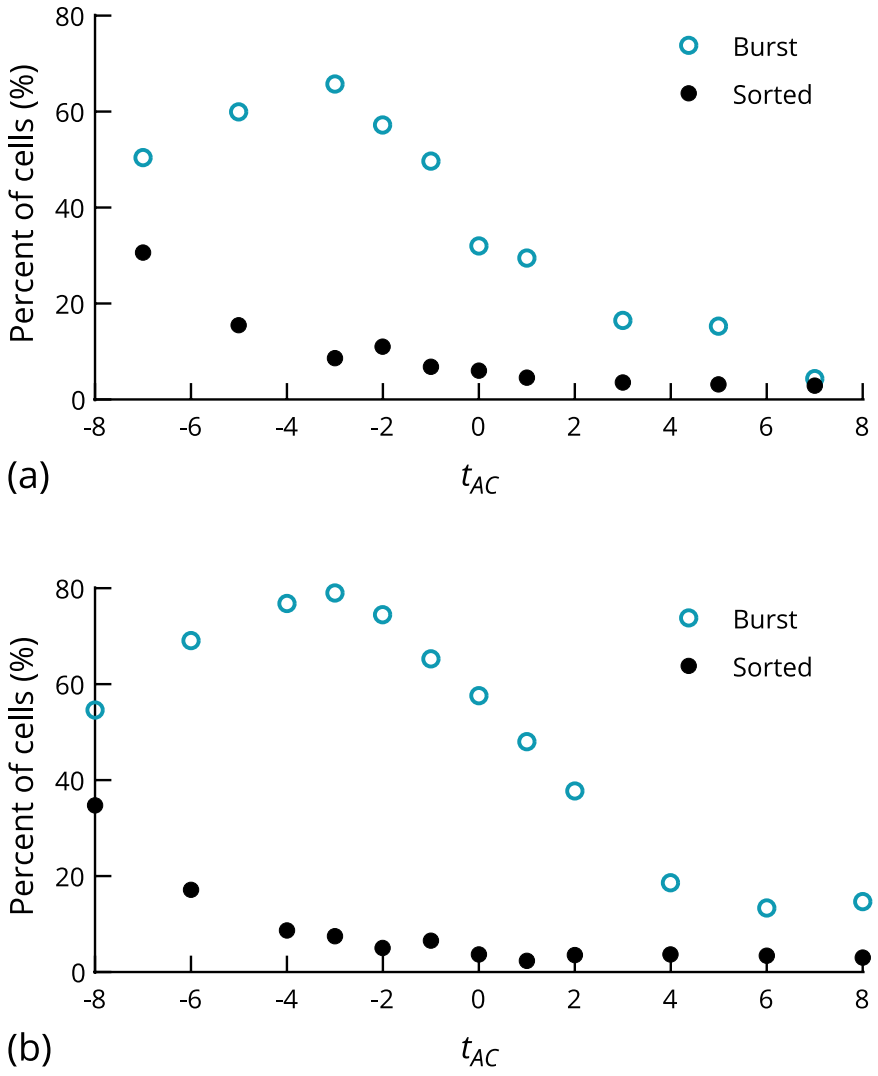

Figure 5.5: Quantification of K562 impacts validates the optimal timing for u_F settings. (a) Percentage of input cell population missing after impact (burst) and present in the waste chamber (sorted) for 4-µm gap distance devices as a function of t_{AC}. Percent of burst cells denoted by open blue circle, percent of sorted cells denoted by filled black circle. Lower t_{AC} values correspond to earlier commencement of µHammer actuation and thus result in initial cell contact with impact assembly further upstream. (b) Percent of cells burst and sorted for 7.5-µm gap distance devices as a function of t_{AC}. N = 100,000 total cells in sample for each t_{AC} value. N = 1 device tested for each gap distance.

lower t_{AC} values correspond to an earlier commencement of actuation, this indicates that the µHammer closes too early with a t_{AC} value of -3 µs, catching a majority of cells on its upstream pincer and subsequently bursting them (as shown in Figures 5.4c and 5.4d). As the t_{AC} value

decreases, the μHammer closes even earlier to the point where it is fully actuated before cells arrive in the compression zone, thereby sorting them into the waste chamber. On the other hand, very few cells were sorted or burst with a t_{AC} of 7 μs (a trend which continues for higher t_{AC} values not shown), suggesting that the μHammer impact is too late and that the majority of cells are missed completely by the impact face with these settings. As the t_{AC} value decreased to 5 μs, however, the percentage of burst cells began to increase substantially, indicating that at this point some cells are caught by the downstream pincer (Figure 5.4b). Collectively, these results demonstrate that cells travel across the μHammer impact face as the t_{AC} value increases from -3 to 5 μs for u_F velocity settings, with a midpoint of 1 μs. This is in agreement with the timing results with beads presented in Chapter 4, validating our conclusion that the optimal t_{AC} value (which results in the highest percentage of centered impacts) is 1 μs for u_F settings.

A similar trend occurred with the 7.5-μm gap distance device (Figure 5.5b). The percentage of burst cells began to increase from baseline levels at a t_{AC} of 4 μs, and continued to increase as the t_{AC} decreased to -3 μs. After this point, the trend reversed, and the percentage of burst cells began to decrease while the percentage of sorted cells began to increase. This indicates that the optimal t_{AC} value for 7.5-μm devices is between 0 and 1 μs, consistent with the optimal t_{AC} value determined for 4-μm devices. Furthermore, both device designs resulted in approximately 30% to 50% of cells being burst with optimal timing settings (t_{AC} = 1 μs, Figure 5.5), indicating that a certain amount of measurement and timing error is inevitable with the current setup. Qualitative assessment of cell impact visualization (demonstrated in Figure 5.4) supports these conclusions. Images of cell impacts with t_{AC} values around 1 μs indicated an equal spread of cell impact locations across the μHammer face (and on both

pincers), images with t_{AC} values around -3 µs indicated a majority of cells were on the upstream pincer, and images with t_{AC} values around 4 µs indicated a majority of cells were missed completely or on the downstream pincer. Collectively, these results validate the optimal timing settings measured with polystyrene beads in Chapter 4, indicating that the timing of µHammer impact for 14-µm cells is essentially equivalent to the timing for 6-µm beads. Furthermore, it demonstrates that the µHammer pincers are functioning as intended, bursting off-center impacts to preserve the uniformity of impact parameters applied to our hit cell population as discussed in Chapter 3.

Although the optimal timing and overall trend in burst versus sorted cells are consistent across 7.5- and 4-µm gap distance devices, Figure 5.5 demonstrates that more cells are burst by the 7.5-µm device than by the 4-µm device. This occurred both on the upstream pincer (80% vs 65%) and with optimal timing (50% vs 30%), although the devices did burst the same amount on the downstream pincer (20%). These results are in agreement with the simulations with 6-µm beads in Chapter 4, which predicted that the 7.5-µm device would have a smaller margin for error in t_{AC} values and thus burst more cells compared to the 4-µm device due to its longer front pincer, which is more likely to catch cells before they can reach the impact face. Furthermore, these results indicate that cells are much more likely to be burst if the timing is too early than too late. This is likely a result of the velocity gradient across the impact face discussed in Chapter 4, which decreases cell velocity in the region of the front pincer and increases cell velocity in the region of the back pincer. As a result, cells spend significantly more time near the upstream pincer than the downstream pincer, greatly increasing the odds that they will be caught and burst by the upstream pincer during mistimed impacts. The percentage of cells burst by early timing is also likely increased by cells being sheared open

as they are sorted into the waste chamber. The current device geometry is not optimized to gently sort cells, and thus even if the μHammer is already closed by the time the cell arrives the cell may still be sheared open by the back of the impact face or the corner of the channel wall as it passes through the small (~13 μm) gap between them (see Figure 5.3a for reference).

5.3 Characterization of K562 cell viability following μHammer impact

5.3.1 Methods

5.3.1a K562 cell impact

Once the μHammer timing settings had been validated, my collaborators and I sought to characterize the ramifications of μHammer impact on K562 cell viability. We impacted the cells suspended in Tyto Running Buffer at 2×10^5 cells/ml as described in Section 5.2.1b with our optimal timing settings, with a few minor differences. First of all, to demonstrate the Tyto's capability to detect fluorescently labeled cells, we stained K562 cells with a nontoxic intracellular dye. Prior to impact, CellTrace™ CFSE (Fisher Scientific, USA) was added to the suspended cells at 0.1% v/v, incubated for 15 minutes in a water bath at 37 °C, and washed. This non-toxic dye covalently binds to lysine residues and other amine sources within the cell, enabling the fluorescent signal of each cell to be detected by both laser-detector pairs in sequence as it travels through the device. We also chose to impact the cells with u_S bead velocity settings (t_{AC} = 3 μs) and a laser-hammer separation distance (x_{LH}) of 80 μm in order to maximize the μHammer's safety factor for error in timing (discussed in Chapter 4), potentially decreasing the percentage of burst cells. We removed any cells that did burst along with their resulting cellular debris from the sample via low-speed centrifugation prior to any subsequent analysis of impacted cellular response. Finally, the hit group samples were only

extracted from the output chamber, since cells in the waste chamber were sorted and not subjected to a μHammer impact.

5.3.1b Membrane damage and cell death assay

To determine if cells were viable immediately following μHammer mechanical injury, we studied cells impacted with several different loading conditions to model different hit severities. Two commonly used experimental temperatures, 8 °C and 37 °C, were compared to identify a possible temperature-dependent cellular response. Fluorescently labeled K562 cells were transferred to the input chamber of a sterile μHammer cartridge, which was maintained at the experiment-dictated temperature. The cells were pressure driven through the device and impacted until 60,000 to 100,000 cells could be collected (approximately 10 minutes per sample). A total of 6 different impact treatments were applied to the cells, combining different impact depths (4-μm and 7.5-μm final gap distances) with different impact durations (10 μs, 100 μs, and 1 ms) at the same impact velocity (2 to 3 m/s). This translates to 39% to 54% applied strain (48% average) for the 7.5-μm final gap device and 67% to 75% applied strain (72% average) for the 4-μm final gap device, both at a 120,000 to 240,000 s^{-1} strain rate (ranges calculated based on average K562 cell size within 1 standard deviation). These impacts were applied to the vast majority of cells passing through the device, with only 1% to 5% of the total population escaping a μHammer impact for hold times less than 100 μs. Cells that were too fast passed by the μHammer into the output chamber without triggering solenoid activation and being hit, while cells that pooled too close together while the cell in front of them was being impacted were sorted into the waste. As the hold time increased, the fraction of cells directed to the waste chamber increased, with an additional 5% to 10% of the total population being sorted into the waste for a 1 ms hold time compared to

the 10 and 100 μs hold times. Cells that were directed to the waste chamber did not affect the purity of the sample, since only cells in the output chamber were extracted for hit group analysis.

Once the sample was extracted, we added SYTOX Red Dead Cell Stain (Fisher Scientific, USA) at 0.1% (v/v) to the cells in suspension to determine if they had compromised membrane integrity or if they were undergoing necrotic cell death. These cells were incubated with SYTOX for 15 minutes at room temperature before being washed. Following staining, the samples were analyzed by MACSQuant Flow Cytometer to determine the concentration of cells positive for SYTOX, as well as the total number of cells remaining. Positive controls were used to set flow cytometer excitation laser voltages and validate the gates used to identify SYTOX-positive cells. These consisted of K562 cells subjected to heat shock via incubation in a water bath at 60 °C for 15 minutes. Two non-impacted control groups were also incubated with the dye and analyzed for concentration of SYTOX. The sham-hit control consisted of cells that had been flowed through the μHammer into the output chamber but not impacted (since the device was not allowed to actuate), and the negative control consisted of cells that had been fluorescently labeled but never introduced to the device. Each impact treatment was repeated in triplicate at each experimental temperature. One μHammer device was used for each final gap distance tested at each experimental temperature, for a total of four different devices.

5.3.1c Apoptosis assay

To see if a μHammer impact induces apoptosis, fluorescently labeled K562 cells were pressure-driven through a sterile μHammer device maintained at 23 °C and impacted until 60,000 to 100,000 cells could be collected (approximately 10 minutes per sample). Six groups

of cells impacted to a 7.5-µm final gap distance and 10-µs impact duration were collected and seeded, along with a negative control that had been fluorescently labeled but never introduced to the device, at 6×10^5 to 1×10^6 cells/mL in 96-well cell culture microplates (Fisher Scientific, USA). At specified timepoints post-impact, Annexin V-APC (Enzo Life Sciences, USA) and SYTOX Blue (Fisher Scientific, USA) were added to each well (at 5% and 0.1% v/v, respectively) and incubated for 15 minutes at room temperature, after which the samples were removed from the wells and washed. Following staining, the samples were analyzed by MACSQuant Flow Cytometer. The apoptotic positive controls used to set flow cytometer excitation laser voltages and validate the gates consisted of K562 cells subject to 0.1 µM staurosporine (RPI, USA) for 4 hours at 37 °C.

Due to the time-dependence of the apoptotic pathway, the timepoints chosen to stain and analyze the cells were 0.5, 1, 1.5, 2, 2.5, and 3 hours after cell collection. This experiment was repeated for a total of two replicates with two different µHammer devices.

5.3.1d Proliferation assay

To investigate the proliferative capabilities of K562 cells after µHammer impact, we cultured cells subjected to impact for up to 8 days while monitoring cell number. These K562 cells were fluorescently labeled, pressure driven through a device maintained at 8 °C, and then impacted to a 7.5-µm final gap distance with a 10-µs impact duration until 1,000,000 cells could be collected (approximately 2.5 hours). Non-impacted, sham-hit control cells were also pressure driven through the device, whereas negative control cells were neither fluorescently labeled nor introduced to the device. Following impact, the hit and sham-hit control samples were spun down for 5 minutes at 300g to remove dead cells and other cellular debris, then resuspended in K562 culture medium. Three replicates of each group were seeded at 9×10^4 to

1.2×10^5 cells/mL for culturing in 12-well cell culture microplates (Fisher Scientific, USA). Approximately every 24 hours for up to 192 hours, cell density was measured in triplicate by MACSQuant Flow Cytometer. This experiment was repeated for a total of three replicates with three different μHammer devices.

After gathering data for all timepoints, the doubling time, t_{double}, of each cell population's exponential growth phase was determined by plotting the natural logarithm of the number of cells, N, as a function of time, t. We determined r by a linear fit with a Levenberg-Marquardt optimization algorithm to the exponential growth phase and assumed exponential increase in the initial number of cells, N_0:

$$\ln N = \ln N_0 + rt.$$

We then solved for doubling time using:

$$t_{double} = \frac{\ln(2)}{r}.$$

5.3.2 Results and discussion

5.3.2a Membrane damage and cell death assay

To determine if K562 cells were undergoing necrotic cell death following μHammer impact, a membrane-impermeant dye (SYTOX) was added that binds with nucleic acids inside cells with compromised membrane integrity. As shown in Figure 5.6, the hit variants at both temperatures consistently registered at or below 1.0% positive for SYTOX as determined by flow cytometry. There was no statistical difference in the uptake of SYTOX between the hit variants, sham-hit controls, and negative controls (p = 0.26 as determined by one-way ANOVA with MATLAB R2015B). This similarity between the control and hit populations indicates that there is no marked increase in membrane damage as a result of μHammer

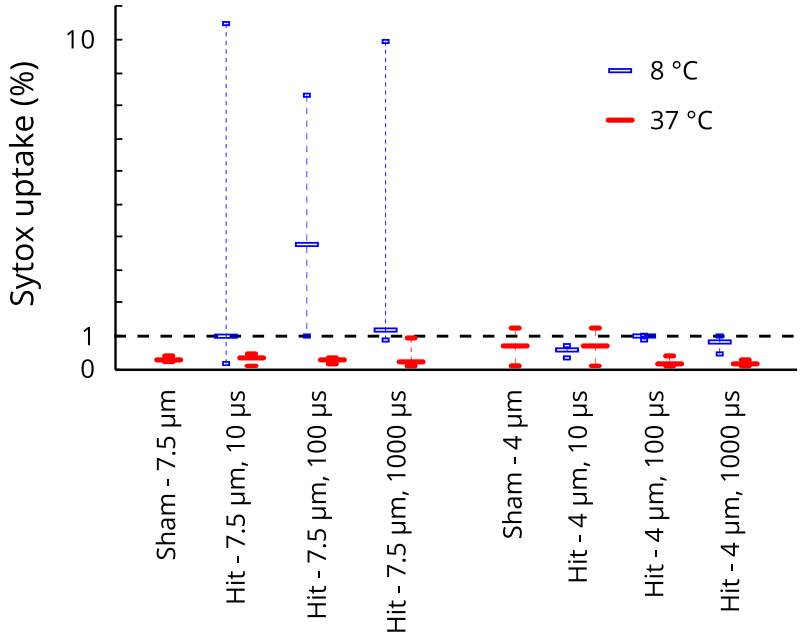

Figure 5.6: Cells experience minimal membrane damage and necrosis following impact. Plot shows percent SYTOX uptake for the sham-hit controls and each of the 6 impact treatments. Sham-hit controls and impact treatments are grouped by device final gap distance (4 µm and 7.5 µm) and arranged in order of increasing impact duration (10 µs, 100 µs, and 1 ms). 8 °C data points depicted with open blue bars, and 37 °C points depicted with filled red bars. Wide bar represents median value, while narrow bars represent maximum and minimum values (all experimental treatments repeated in triplicate). Black dotted line emphasizes that nearly all data points are at or below 1% uptake of SYTOX.

impact. However, approximately 20% to 40% of the hit populations were missing after each experiment, indicating a significant burst cell population as discussed in Section 5.2.2. Since this percentage did not increase with hit severity, the burst population likely consisted of either mistimed impacts or larger cells (>16 µm) that were sheared or pierced by the µHammer pincers during off-center hits, and thus did not result from typical µHammer impacts. Furthermore, these dead (burst) cells and the resulting cellular debris were removed from the sample via low-speed centrifugation prior to any subsequent analysis of impacted cellular response.

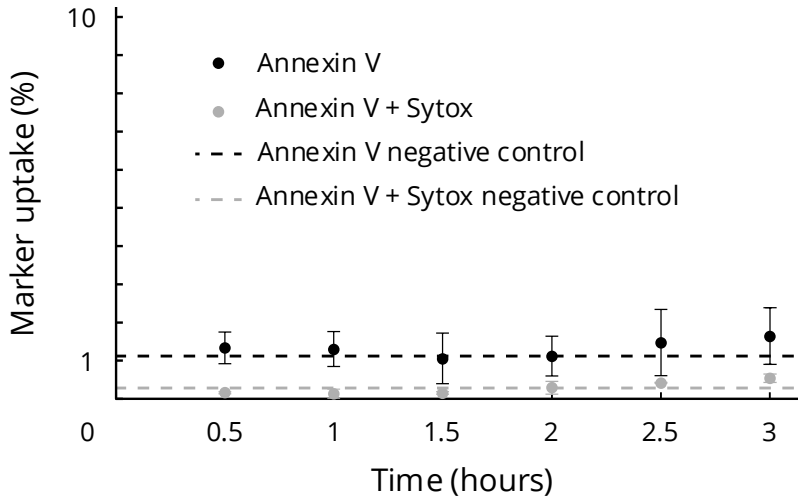

Figure 5.7: Cells experience minimal programmed cell death following µHammer impact. Plot depicts percent uptake of Annexin V (early apoptosis) and Annexin V + Sytox (late apoptosis) of hit cells (7.5-µm final gap, 10-µs hold time). Dotted lines depict percent uptake of Annexin V (1.1%) and Annexin V + Sytox (0.3%) in negative control. Error bars depict standard deviation across two experimental replicates.

5.3.2b Apoptosis assay

Having ruled out increased necrotic cell death shortly after impact, my collaborators and I next considered the possibility of induced apoptosis, a programmed cell death with a time scale on the order of hours. During the beginning stages of apoptosis, phosphatidylserine (PS) is translocated to the outer cell membrane, an event that can be identified by the addition of Annexin V. This membrane impermeant marker specifically binds with PS to identify apoptotic cells. In later stages of apoptosis, the cell membrane degrades, an event that can be identified by the addition of SYTOX as described in the previous section.

As shown in Figure 5.7, there was no statistical difference in the presence of Annexin V between the hit populations and the controls at any time point ($p = 0.93$). Even at 3 hours after impact, less than 2.0% of hit cells tested positive for the apoptotic marker Annexin V alone and 1.0% for the late stage apoptotic markers Annexin V and SYTOX together. Thus, there

was no indication that a μHammer impact to a 7.5-μm final gap with a 10-μs hold time causes cells to initiate apoptosis.

Collectively, due to the lack of Annexin V binding and SYTOX uptake, we conclude that a μHammer impact does not induce cell death in K562 cells across a wide range of hit severities.

5.3.2c Proliferation assay

Once we determined that a μHammer impact does not induce death in K562 cells, we cultured cells subjected to impact for up to 8 days while monitoring cell number to investigate their proliferative capabilities. In each of three independent experimental replicates, cell populations that experienced impact had impaired proliferation compared to the sham-hit and negative control populations (Figure 5.8). The negative control populations grew exponentially from the time they were seeded at hour 0 until they reached plateau phase between 115 to 140 hours later. The sham-hit populations started exponential growth within 24 hours and followed a similar growth trajectory, reaching plateau phase in the same time span. The hit populations, conversely, did not enter exponential growth until 50 to 70 hours after seeding, and thus had a lag phase 25 to 50 hours longer than the sham-hit control. Furthermore, the hit populations did not reach plateau phase within the timespan of the conducted experiment.

Despite disparate log phase durations between groups, their respective doubling times during the exponential phase of growth (Figure 5.8, inset) were not statistically different (averages of 33.4 hours [standard deviation, SD, 5.1 hours], 32.2 hours [SD, 1.7 hours], and 34.2 hours [SD, 1.5 hours] for the negative control, sham-hit control, and hit groups respectively across all three replicates, $p = 0.74$). The cells impacted by the μHammer retained

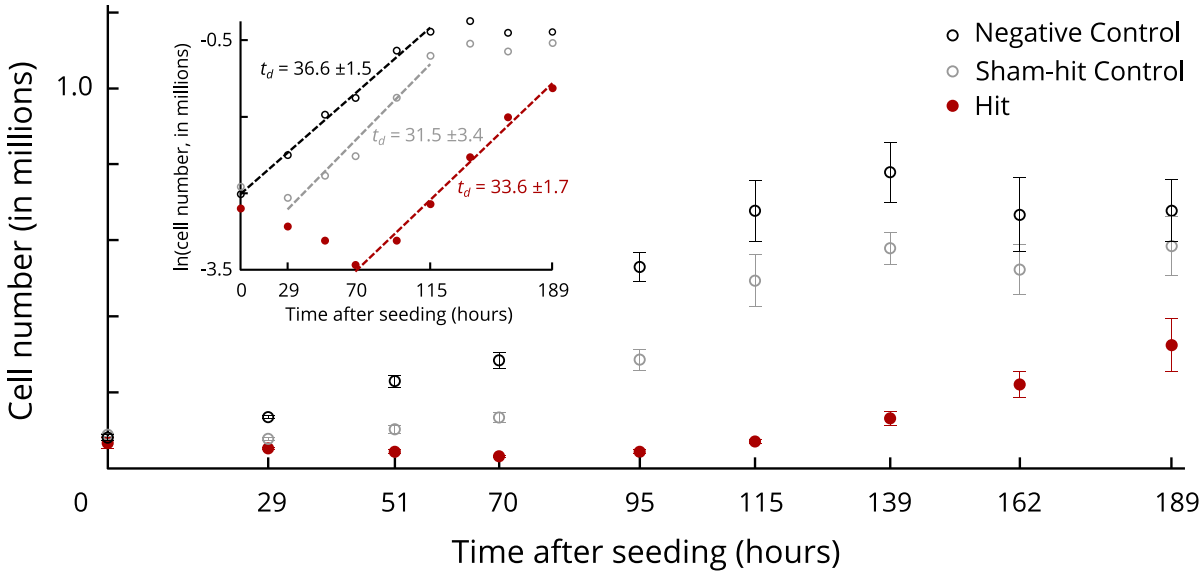

Figure 5.8: µHammer impact temporarily affects cell proliferation. Plot of representative data from one replicate, showing K562 cell growth over 8 days culturing post-µHammer experiment. Inset shows plot used to calculate doubling time values, as determined by slope of best fit line in exponential region as shown. Error bars depict standard deviation of cell number in this experimental replicate ($N = 3$ wells per group, all taken from the same initial population of cells and impacted with the same device).

their ability to proliferate post-impact, demonstrating that basic cellular functions (including cell division and metabolism) were not irreparably compromised following impact. However, as previously mentioned, these hit populations also experienced an extended lag phase. The similarity between the proliferation of the negative and sham-hit controls demonstrates these lag effects in the hit cells are the result of the µHammer impact alone, not other variables arising from cell labeling or the device microfluidics. From this, we conclude that the µHammer can apply controlled, sublethal cellular damage, a prerequisite to enable study of the biological consequences of mechanical impacts on cells at longer timescales relevant to human physiology.

Chapter 6. Device Optimization

6.1 Introduction

As discussed in Chapter 5, my collaborators and I have demonstrated the μHammer's ability to apply sublethal cellular damage through dynamic, serial impacts to large populations of cells. However, we have also demonstrated that even with optimal timing, a significant portion of the cells (up to 40%) will be burst by off-centered impacts, reducing the effective throughput of the device. This is sub-optimal, since we seek to maximize the amount of data collected in each experiment in order to efficiently investigate the consequences of mechanical impacts on inherently heterogeneous cell populations.

In order to understand the root causes of mistimed impacts and fully leverage the μHammer's high throughput capabilities, I sought to more thoroughly characterize the μHammer's timing as a function of the experimental conditions of the fluid and particles flowing through it. Parameters such as flow velocity and particle size are known to affect the trajectories of particles through microfluidic devices like the μHammer and have been studied extensively in these systems, but the effects of temperature, buffer viscosity, and particle concentration are not as well understood [113-115]. In this chapter, I introduce the phenomenon behind these effects, known as inertial focusing, and discuss how it manifests itself in the μHammer. I then explore how the aforementioned parameters affect the performance of the μHammer, first by tracking the velocity of polystyrene beads through the device and then by visualizing the impact of these beads. As demonstrated in Chapters 4 and 5, polystyrene beads are a good proxy for cells in the μHammer since they have similar timing profiles while being easier to visualize. Through these assays, I show that the timing of our

device is sensitive to changes in the ratio of inertial forces to viscous forces that particles experience while traveling through it. I then discuss how this sensitivity provides a set of parameters that can serve as a robust framework for optimizing μHammer performance under various experimental conditions. I conclude this chapter by applying the lessons gleaned from characterizing the current μHammer design to develop and model the next design generation in COMSOL, demonstrating how to improve μHammer performance even further in future iterations.

6.2 Background of flow focusing in microchannels

6.2.1 Theoretical background

When cells and other particles pass through a microfluidic channel, they experience both inertial and viscous drag forces, the ratio of which is typically described by the Reynold's number, *Re.* Under certain conditions, this combination of forces pushes the particles away from the center of the channel toward equilibrium points near the periphery. The conditions under which particles are guided into these equilibrium positions in straight channels is described by the particle Reynolds number, Re_p [113, 115]. This quantity is related to the Reynolds number of the flow, *Re*, but is rescaled to account for the ratio of particle to channel size:

$$Re_p = \frac{u_{max}\rho a^2}{\mu D_h}.$$

In this relationship, u_{max} = maximum fluid velocity, ρ = fluid density, a = particle diameter, μ = dynamic fluid viscosity, and D_h = channel hydraulic diameter, which is a function of the channel height, h, and width, w: $D_h = 2hw / (h + w)$. When Re_p is on the order of 1, inertial lift forces dominate and the particles are focused to equilibrium positions that depend on the

channel geometry [115]. The formation of these equilibrium positions has been studied extensively as a function of most parameters which determine Re_p, including flow velocity and particle size [114-116]. However, little documentation exists regarding the effects of buffer viscosity and temperature (which influences viscosity) on these focused streams in microfluidic systems. Although some studies have investigated the role of buffer viscosity in mixing and droplet formation [117, 118] or in inertial focusing of viscoelastic fluids and coflow systems [119, 120], the μHammer provides a platform to further understand how the interplay between buffer fluid temperature, viscosity, and other experimental parameters affects the inertial focusing of a microfluidic device with a single stream of Newtonian fluid.

In the case of a rectangular channel as is used in the μHammer, there are generally two equilibrium positions that are centered along the longest sides of the channel (Figure 6.1a). The width of these streams as well as their distance from the channel wall, x_f, can vary with the Re_p value of the system [115]. In order for particles to reach their equilibrium positions, however, they must travel a minimum distance along the channel length, L, which we define as:

$$L_{min} = \frac{3\pi\mu h^3}{u_{max}\rho a^3}$$

[121]. The concentration of particles suspended in the buffer solution also affects their trajectories, since when particles are too close together they fail to focus effectively into their preferred streamlines due to steric crowding effects [122-124]. The critical volume fraction of particles for the onset of this effect, φ_C, is approximately 0.001 to 0.01 [122, 125, 126]. On the other hand, for $\varphi < \varphi_C$, some studies have reported that focused streams form more quickly and to a narrower width as φ increases [116, 127]. This is likely due to hydrodynamic interactions between particles that help them reach their equilibrium positions [116].

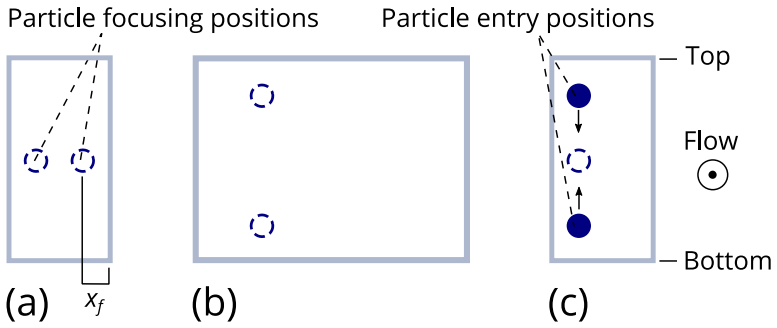

Figure 6.1: Illustrations of focused stream positions for different channel geometries and experimental conditions. In all panels, channel cross-section is depicted in grey, with flow coming out of page. Top and bottom of channels are marked. Focused stream locations at equilibrium are depicted by blue dashed circles. (a) Stream positions for generic rectangular channel (height / width ratio h / w > 1). Distance of focused stream from the closest channel wall, x_f, is marked. Stream width is determined by size of focused particle region(s). (b) Stream positions for inlet focusing channel (single slice of variable cross-section geometry shown; h / w = 0.75). (c) Stream positions for μHammer channel (h / w = 2). Particle positions at channel entry are marked with solid blue circles. Arrows depict movement of particles toward focusing position. Only one equilibrium position is shown, since particles are already ordered when they enter the channel and thus do not sample the second focusing node depicted in panel a.

For channels with curves or variable cross-sections, such as the μHammer's inlet focusing channel [111], the locations and widths of focusing streams are much harder to predict. These geometries introduce secondary flows that interact with the inertial lift forces to create new equilibrium locations [115]. The magnitude of this interaction is described by the Dean number, *De*, which scales *Re* to account for the varying curvature of the channel:

$$De = Re \cdot f\left(D_h, r_{eff}\right),$$

where f is a function of D_h and the channel's effective radius of curvature, r_{eff}. Collectively, these dependencies indicate that flow velocity, particle size, particle concentration, and buffer viscosity (which in turn depends on temperature) will all affect the trajectory of particles flowing through the μHammer.

6.2.2 Flow focusing in the μHammer

In the context of the μHammer, cells or other particles passing through its microfluidic channels experience a combination of inertial forces, viscous forces, and secondary flows. These interactions focus the particles into predictable regions of the channels prior to impact. As described in Chapter 4, particles initially flow through a focusing channel of varying cross-section before entering the μHammer chip. This channel geometry introduces secondary flows that interact with the forces typically experienced in rectangular channels, directing particles into one of two streams vertically oriented on the same side of the focusing channel (Figure 6.1b). As particles transition into the rectangular μHammer channel, the focused streams maintain the same orientation. However, due to the change in aspect ratio, the equilibrium locations shift and the focused streams begin to migrate toward each other (Figure 6.1c). Since the μHammer channel is relatively short (~350 μm), streams may or may not converge depending on the L_{min} for those experimental conditions.

Achieving and maintaining focused streams in the μHammer channel is important, since the fluid velocity in a rectangular channel decays parabolically from its center during Poiseuille flow (Figure 4.9) [128, 129]. The μHammer meets the conditions of a Poiseuille flow, with an incompressible fluid as the buffer, a low *Re* on the order of 10 to 100 (ensuring laminar flow), and L (~350 μm) much greater than D_h (~30 μm). Thus, by limiting the lateral movement of particles as they travel through the μHammer and by making their path more consistent, inertial focusing minimizes the magnitude of velocity changes during transit. Focusing also constrains the particles to a narrow window of distances from the side of the channel, which makes the initial contact point between the μHammer impact face and the particles more uniform. Given this improved consistency in both particle velocity and

location, it is clear that flow focusing is a powerful tool for optimizing the timing and ultimately the throughput of our device.

6.3 Optimization of µHammer timing

6.3.1 Methods

6.3.1a Quantifying bead impacts

In order to determine the effect of various experimental parameters on device performance, I used the optimal t_{AC} (post-arrival closure time) values that resulted in the highest percentage of centered bead impacts (as discussed in Chapter 4) to quantify the percentage of beads that were centered and missing as a function of bead velocity (u_F vs u_S), temperature (8 vs 37 °C), and laser-hammer separation distance (80 vs 60 µm). These assays were carried out using the methods discussed in Chapter 4. Briefly, I suspended 6-µm-diameter Polybead® microbeads (Polysciences, Inc., USA) in buffer at the appropriate concentration to enable the detection and impact of 300 ± 50 beads/s (2.8×10^5 beads/mL for slow bead velocity, u_S, and 1.4×10^5 beads/mL for fast bead velocity, u_F). I then loaded the beads into the µHammer cartridge of a 4-µm final gap distance device, at which point they were pressure-driven through the µHammer channel and timed using backscatter signals. Once the beads were timed and impacted by the µHammer, they were held in compression for 200 µs and imaged by a Ximea MQ003MG-CM high-speed camera (Ximea, Germany). These images were taken at a rate of 10 Hz to gather data from a representative fraction of the total impacted bead population. Using image analysis software (ImageJ Version 1.50i, public domain), I classified the captured beads according to their position along the impact face. Beads found within 7 µm of either pincer were labeled "burst," while beads outside of these

zones near the center of the impact face were labeled “centered.” If no bead was found in the image, I applied the label “missing.” For each combination of settings tested, at least five replicates of 500 images were collected. Each replicate was obtained using a unique device.

To determine the effects of throughput on µHammer timing, I increased the concentration of beads first to 5.6×10^5 beads/mL and then to 1.1×10^6 beads/mL (corresponding to volume fractions, φ, of 6.0×10^{-5} and 1.2×10^{-4}). I then impacted them with the µHammer’s benchmark settings (37 °C, u_S, 60-µm x_{LH}) at throughput values of 600 ± 50 beads/s and 1,200 ± 50 beads/s, respectively. For the 600 beads/s group, four replicates of 500 images were gathered with different devices. Only one dataset was acquired for the 1,200 beads/s group, since at this concentration the beads tended to accumulate between the Ni–Fe poles and prevent actuation.

6.3.1b Quantifying flow profile

In order to investigate the effects of temperature and average bead velocity on the µHammer’s flow profile, I suspended 6-µm beads in buffer at the appropriate concentration for a throughput of 300 ± 50 beads/s (as described in the previous section), then flowed them through the µHammer device at a controlled average velocity (u_F or u_S). I did this at both 8 °C and 37 °C while measuring the transit time between lasers, t_{LL}, of each bead. The solenoid was never actuated, allowing the beads to pass through the device unimpacted. For each of these experimental groups, data were collected over the course of approximately 0.5 min with a single device until a total of 10,000 beads were measured.

In subsequent experiments, I repeated the same assay with different experimental conditions. First, I added BSA at 5% w/v to increase the viscosity of the buffer solution and measured the t_{LL} of beads flowing through the device at 37 °C with u_F settings. Next, I replaced

the 6-µm beads with 7.5-µm SPHERO™ polystyrene beads (Spherotech, Inc., USA) and then with 10-µm Polybead® polystyrene beads (Polysciences, Inc., USA) to repeat the assay, also at 37 °C with u_F bead velocity. Finally, I increased the concentration of 6-µm beads to achieve a throughput of 600 beads/s and measured the t_{LL} of each bead at 37 °C with u_S bead velocity.

To further investigate the effects of throughput on timing efficacy, I determined the bead velocity, u, as a function of time after the previous actuation, t_{SD} (see Table 4.3 for a detailed description of t_{SD}). Since the t_{LL} values for low t_{SD} were too large to measure accurately, the full-width half-maximum travel time, t_{FWHM}, across the final detecting laser was measured instead for each bead. I performed this assay using the µHammer's benchmark settings (37 °C, u_S, 60-µm x_{LH}) at a throughput of 600 beads/s, gathering data from a total of 60,000 beads over the course of approximately 2 min. A least-squares linear regression was fit to a t_{LL} vs t_{FWHM} plot of the data, which was then used to transform from t_{FWHM} to t_{LL} and ultimately to the bead velocity, u.

6.3.2 Results

6.3.2a Quantifying bead impacts

In order to determine how different experimental conditions affect the performance of the µHammer, I analyzed images of impacted polystyrene beads during their hold time of compression. I performed these experiments with the optimal t_{AC} (post-arrival closure time) values that result in the highest percentage of centered impacts. As discussed in Section 4.4.2b, 6-µm beads were chosen for this experiment since they are larger than the devices' 4-µm final gap distance, x_G, and thus are immobilized between the impact face and the channel wall during the entire hold time of compression (Figure 4.12a). Beads found within 7 µm of the

pincers bounding the μHammer impact face were labeled "burst," since cells greater than 14 μm in diameter (like K562 cells) impacted in this region are likely caught by the pincers and burst during compression. Beads were labeled "centered" if they were found at least 7 μm from either pincer during compression, representing an ideal impact. Finally, beads were labeled "missing" if there was no bead present in the image, representing beads that were either sorted into the waste via through significantly early timing or beads that were allowed to pass into the output via untouched through significantly late timing.

To determine the effect of flow velocity and temperature on μHammer performance, I gathered and analyzed images at a total of four different combinations of bead velocity (u_S vs u_F) and temperature (8 °C vs 37 °C). The results shown in Figure 6.2a demonstrate that there was no significant difference in the percentage of centered and missing beads between fast bead-velocity settings, u_F, and slow bead-velocity settings, u_S, at 8 °C. However, increasing the temperature to 37 °C led to an increase in centered impacts with u_S settings and a significant decrease with u_F settings.

As shown in Figure 6.2b, decreasing the laser-hammer separation distance, x_{LH}, from 80 μm to 60 μm significantly increased the percentage of centered impacts. This indicates that at least some of the burst and missing beads are the result of t_{LL} (laser transit time) measurement errors or changes in bead velocity between laser detection and solenoid activation. When either of these occur, the bead arrives in the impact region at a different time than predicted. This increases the likelihood that the bead will be burst or even missed completely. By decreasing x_{LH}, we decrease the distance between the measurement and impact areas, limiting the magnitude of these timing errors and subsequently increasing the percentage of centered impacts. Although a further decrease in x_{LH} would potentially be

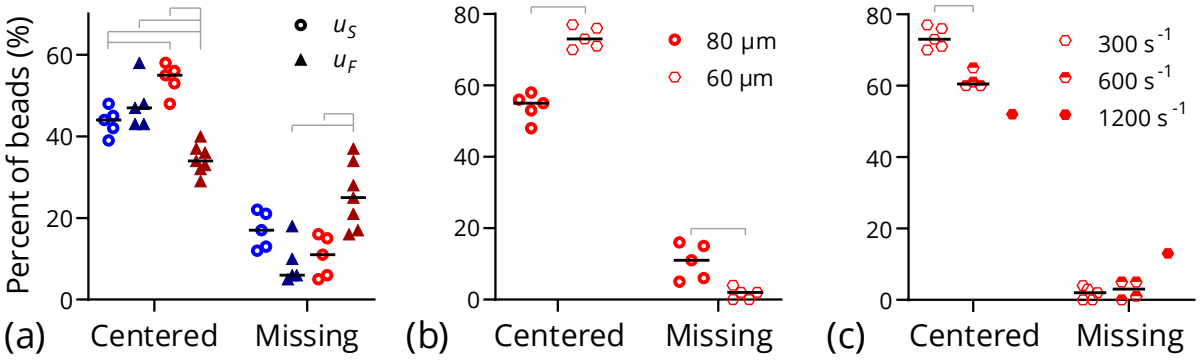

Figure 6.2: Efficacy of µHammer timing varies with temperature, bead velocity, laser-hammer separation distance, and throughput. (a) Percentage of centered and missing beads as a function of temperature and bead velocity. Four different combinations of parameters were tested: 8 °C temperature in blue, 37 °C in red, u_S bead velocity as open circles, and u_F as filled triangles. (b) Percentage of centered and missing beads as a function of laser-hammer separation distance, x_{LH}. Data for 80-µm x_{LH}, u_S bead-velocity settings duplicated from panel a for reference. (c) Percentage of centered and missing beads as a function of impact frequency. Data for 300 bead/s throughput, 60-µm x_{LH} settings duplicated from panel b for reference. N = 500 images analyzed for each experimental replicate. Black line depicts average of replicates for each group, gray brackets connecting two groups indicate statistical difference ($p < 0.01$). Factors tested by two-way ANOVA in panel a were temperature and bead velocity.

beneficial, due to manufacturing processes the bottom of the channel near the impact region has increased surface roughness compared to the rest of the channel. Lasers reflected from these relatively rough surfaces add a high level of noise to the backscatter and fluorescent signals used for timing µHammer impacts, significantly compromising the device's ability to detect particles and calculate their velocity. 60 µm was the shortest x_{LH} that consistently generated clean signals in my experiments, and thus is the optimal laser-hammer separation distance for the current devices with u_S settings.

Finally, to determine the effect of concentration on device performance, I analyzed µHammer impacts while running at increasing concentrations of 5.6×10^5 beads/mL and then 1.1×10^6 beads/mL (corresponding to throughput values of 600 beads/s and 1,200 beads/s).

These results were compared to those obtained previously at a concentration of 2.8×10^5 beads/mL (300 beads/s). As shown in Figure 6.2c, the percentage of centered beads decreased as the concentration increased. The highest percentage of centered beads (~75%) was achieved with the lowest throughput tested (300 beads/s). This translates to an effective impact frequency, ω_{eff}, of 225 centered beads/s. However, the highest ω_{eff} (360 centered beads/s) of the settings tested that resulted in minimal missing beads (< 5%) was achieved with a throughput of 600 beads/s. Under these settings, the higher overall throughput compensates for the decreased percentage of centered beads (~60%), thereby maximizing ω_{eff}.

6.3.2b Quantifying flow profile's sensitivity to Reynolds number

As discussed in Section 6.2.2, the focusing element positioned before the µHammer channel is designed to focus the beads into one of two streams (Figure 6.1b). These streams are stacked vertically on the side of the channel nearest to the impact face at rest. Once the beads enter the µHammer channel and flow through it, the streams begin to shift towards each other as shown in Figure 6.1c. However, the predicted distance required for convergence of these streams, L_{min}, is approximately 1,000 µm for u_F, 37 °C settings (and even higher for the other conditions tested) with 6-µm beads. Since the µHammer channel is only 350-µm long, this indicates that the streams will not converge. Instead, they remain as two vertically stacked streams on the same side of the channel, whose location can vary with Re_p. The system's Re_p value, in turn, depends on the maximum flow velocity, u_{max} (which is estimated to be equivalent to the maximum bead velocity), the dynamic viscosity, μ (which is estimated based on the temperature and BSA concentration of the buffer solution using the relationship generated by Monkos [130]), and the bead diameter, a. These relationships suggest that the

changes in impact efficacy illustrated in Figure 6.2a may be due to changes in the focusing profile.

In order to uncover the mechanism behind these changes in device performance, I investigated how different experimental settings influenced the flow of beads through the μHammer. I explored this by measuring the laser transit time, t_{LL}, of each bead as it passed through the device. As shown in Figure 6.3a, the t_{LL} values for u_S bead-velocity settings at both 8 °C and 37 °C were grouped into two distinct peaks. In the images of bead impacts discussed in the previous section, the beads in the peak with higher t_{LL} values were in a focal plane closer to the top of the channel than beads in the peak with lower t_{LL} values. This suggests that these peaks each correspond to a separate stream with a different range of fluid velocities. Since the fluid velocity in the channel decays parabolically from the center (Figure 4.9), the peak with higher t_{LL} values and thus lower bead velocities likely corresponds to a stream that is closer to the channel wall than the other focused stream ($x_{f1} < x_{f2}$, Figure 6.3b). Furthermore, Figure 6.3a shows that the width of the transit-time peaks decreased when the temperature changed from 8 °C (μ = 1.3 mPa·s, Re_p = 1.4) to 37 °C (μ = 0.7 mPa·s, Re_p = 2.5). This indicates that the width of the focused streams decreases with increased temperature for u_S settings, ultimately demonstrating an increase in focusing performance.

For u_F bead-velocity settings, on the other hand, the t_{LL} peaks and thus the bead streams were already tightly focused at 8 °C (μ = 1.3 mPa·s, Re_p = 2.4, Figure 6.3c). When the temperature increased to 37 °C (μ = 0.7 mPa·s, Re_p = 6.0), the t_{LL} peaks shifted dramatically outward, widening the gap between them (Figure 6.3c). This suggests that the slower stream focuses even closer to the wall as the temperature increases for u_F settings ($x_{f1,\,37C} < x_{f1,\,8C}$).

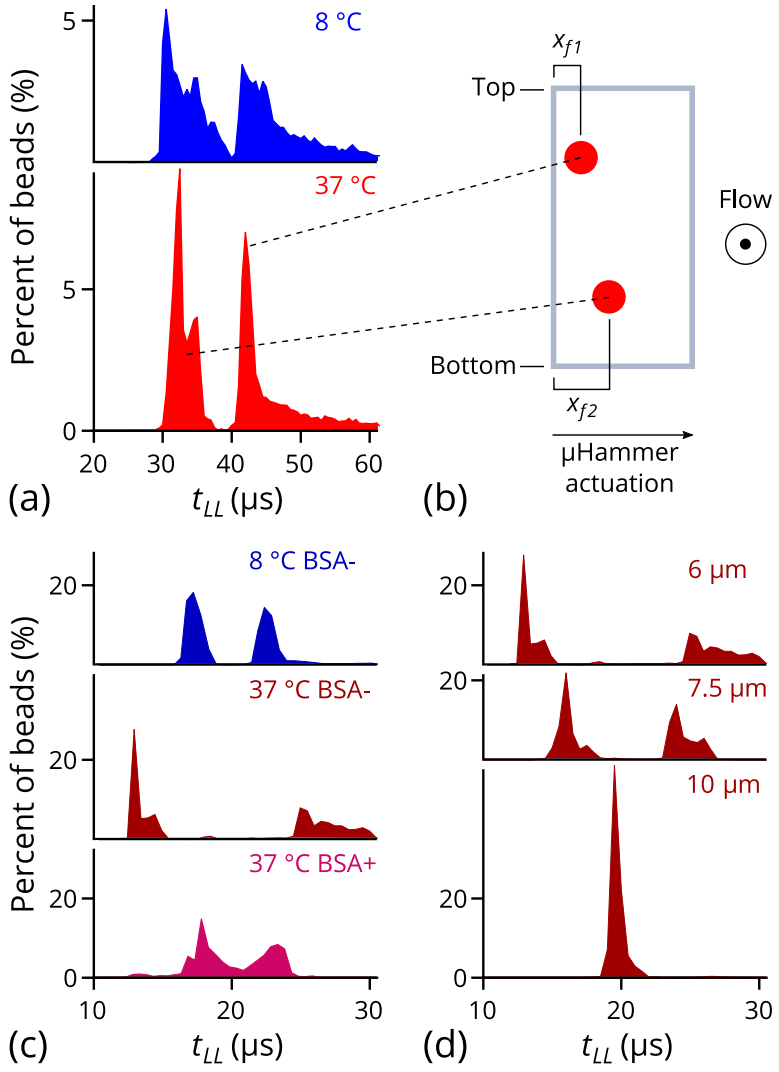

Figure 6.3: µHammer flow profile varies with changes in the particle Reynolds number, Re_p. (a) Histograms of the laser transit times, t_{LL}, for u_S bead-velocity settings as a function of temperature. (b) Slice of µHammer channel with approximate locations of the two focused streams. Top and bottom of channel are marked, as well as direction of µHammer actuation across channel. Flow direction is out of page. Distances between top / bottom stream and side of µHammer channel are marked x_{f1} and x_{f2}, respectively. Note that $x_{f1} < x_{f2}$. Distances of streams from top and bottom walls of the channel can also vary. (c) Histograms of t_{LL} for u_F settings as a function of temperature and viscosity. (d) Histograms of t_{LL} for u_F, 37 °C settings as a function of bead size. 6-µm bead data duplicated from panel c for reference. N = 10,000 beads analyzed for each experimental condition. All t_{LL} histograms created with a 0.5-µs bin width.

When this occurs, the velocity of the slower stream decreases, while the velocity of the faster stream conversely increases in order to maintain the same average bead velocity, u_F. This hypothesis is supported by the fact that in straight channels, the equilibrium stream position gets closer to the channel wall with increasing *Re* [115] and thus with decreasing viscosity.

Based on these results, it seems likely that the relationship between temperature and buffer viscosity, μ, is the root cause of these differences in bead trajectory and stream focusing when the average bead velocity is held constant. To confirm this, I added BSA to the buffer solution at 5% concentration (w/v). This addition slightly increased μ to 0.9 mPa·s and Re_p to 3.8 at 37 °C with u_F settings, resulting in μ and Re_p values intermediate between their respective values at 8 °C and 37 °C. As shown in Figure 6.3c, the t_{LL} profile for this condition was also intermediate between the 8 °C and 37 °C profiles in the absence of BSA. This indicates that μ is indeed the driving force behind changes in focusing with temperature and is thus a useful tool that can be used to fine-tune the focusing profile of the µHammer.

Although I could not impact beads larger than 6 µm without clogging the device, I did gather information on the trajectories of these larger beads as they flow through the µHammer. The effect of bead diameter, a, on t_{LL} is shown in Figure 6.3d. The t_{LL} peaks of the 7.5-µm beads (Re_p = 8.5) were shifted closer together compared to the peaks of the 6-µm beads (Re_p = 6.0), while the 10-µm beads (Re_p = 12.2) had only one t_{LL} peak. In these cases, it seems probable that the edge of the faster stream at the bottom of the channel moves closer to the wall as the bead size increases. This continues until the bead size reaches 10 µm, at which point the stream at the bottom of the channel is the same distance from the wall as the stream at the top of the channel ($x_{f1} = x_{f2}$). The two streams may even converge under these conditions, since the predicted L_{min} is only 300 µm for 10-µm beads at 37 °C with u_F settings. This is

approximately the same predicted L_{min} for 14-µm diameter cells with u_S settings at 37 °C, which also typically result in a t_{LL} profile with one focused peak (not shown). Thus, the beads and cells in these scenarios may travel a sufficient distance along the length of the µHammer channel to reach their equilibrium positions. Collectively, these results indicate that particle size, fluid velocity, and buffer viscosity are all crucial elements to consider when using the µHammer or any other microfluidic device where timing is important.

6.3.2c Quantifying flow profile's sensitivity to bead concentration and throughput

As discussed in Section 6.2.1, concentration is another parameter that can affect the flow of beads through microfluidic channels. Beads are more likely to focus into their equilibrium streams when the volume fraction, φ, of beads in solution is on the order of 1×10^{-3} or lower. The highest φ that I tested was 1×10^{-4} (for 6-µm beads at a concentration of 1.1×10^{6} beads/mL), indicating that these solutions fall in the region of volume fractions where increasing concentration can have a positive effect on bead focusing. This hypothesis is confirmed by the results in Figure 6.4a, where the laser transit-time t_{LL} peaks narrowed in width and moved slightly closer together as the concentration increased from 2.8×10^{5} to 5.6×10^{5} beads/mL (corresponding to throughput values of 300 and 600 bead/s, respectively).

To further explore the effect of throughput on device performance, I analyzed how actuation affects the flow profile of beads through the device. I did this by tracking the bead velocity, u, as a function of time since the last actuation, t_{SD}, as shown in Figure 6.4b. In this plot, only the highest u value for each t_{SD} is shown, likely corresponding to beads travelling down the middle of the channel where the flow velocity is highest. This allows interactions with the sidewalls to be ruled out as the cause for any changes in velocity. Figure 6.4b shows

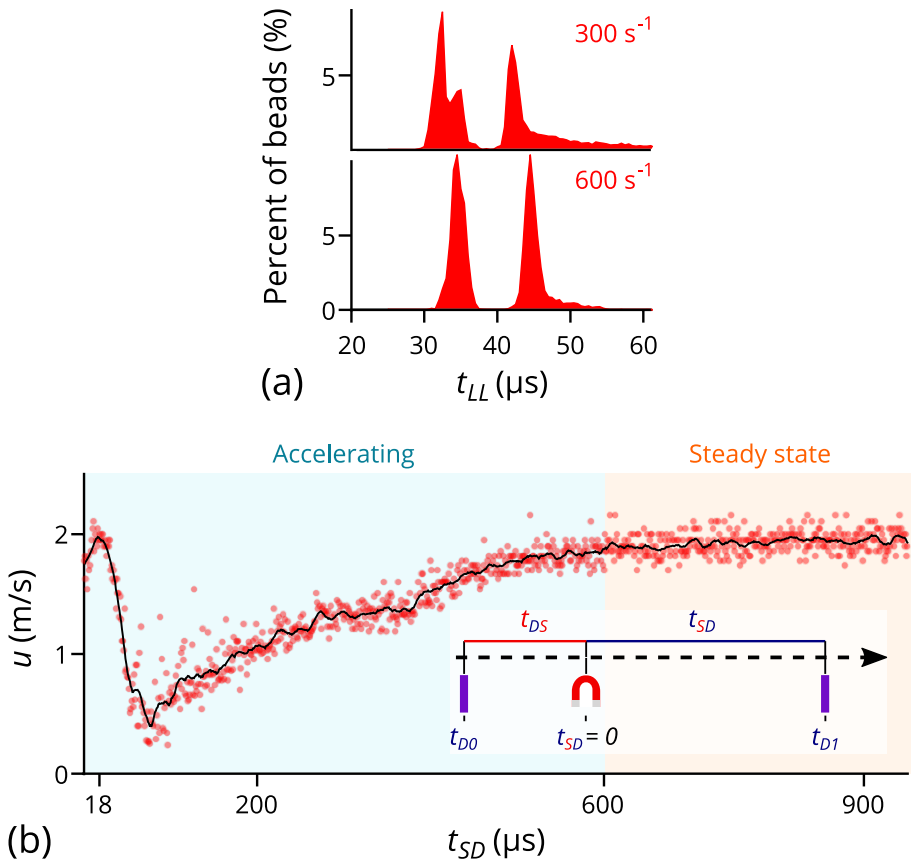

Figure 6.4: µHammer flow profile varies with bead concentration and throughput. (a) Histogram of laser transit time, t_{LL}, as a function of throughput for u_S, 37 °C settings. 300 beads/s throughput data duplicated from Figure 6.3a for reference. N = 10,000 beads analyzed for each experimental condition. (b) Bead velocity, u, as a function of time after the µHammer last actuated, t_{SD}. Inset illustrates relationship between the time bead 0 is detected (t_{D0}), the time solenoid is activated to impact bead 0 (t_{SD} = 0), and the time bead 1 (whose velocity is plotted in this panel) is detected (t_{D1}). Only the maximum u value measured for each t_{SD} value is shown, taken from a total of 60,000 measurements across all t_{SD} values. The µHammer begins to actuate at 0 µs, completes actuation at 18 µs, and begins to return to rest at 200 µs. Accelerating (t_{SD} < 600 µs) and steady-state (t_{SD} > 600 µs) velocity regions marked on chart with blue and orange backgrounds, respectively. Black line depicts data points smoothed with a Savitsky-Golay filter averaging 10 points on each side.

that u increased immediately after actuation began (t_{SD} = 0 µs) until the µHammer reached full actuation (t_{SD} = 18 µs). It then quickly dropped by ~90%, after which it slowly recovered until it returned to steady-state (t_{SD} ≈ 600 µs).

This dynamic bead-velocity profile reflects changes in the fluidic path through the device during actuation. When the μHammer begins to actuate, it blocks a portion of the channel and thus narrows the width of the fluidic path. Once the μHammer reaches the other side of the channel, it diverts all fluid to the waste via during the hold time of compression. It then returns to rest, allowing the fluid to flow normally into the output via until the next actuation. These sudden changes to both the fluidic resistance and the fluidic path cause the flow velocity to change dramatically, then slowly recover as the flow profile returns to steady-state.

The probability that such a dramatic change in velocity will occur to any given bead is directly related to throughput. As the throughput increases, the average time between consecutive bead detections decreases. This in turn results in an increased percentage of beads (5% to 10% at 300 beads/s, 20% at 600 beads/s, 40% at 1,200 beads/s) with low t_{SD} values (< 600 μs). Beads detected in this low t_{SD} region are accelerating and thus are difficult to time. As a result, minimizing the number of beads present in this region will maximize the percentage of centered bead impacts. Preliminary experiments with throughput values below 300 beads/s (not shown) did not result in a further increase of centered bead impacts, suggesting that the number of beads with low t_{SD} values is already minimized at 300 beads/s and that the percentage of centered bead impacts as a function of throughput is already maximized. Collectively, these results demonstrate the importance of considering both particle concentration and throughput in experimental design for the μHammer, especially when attempting to impact millions of cells in a single experiment.

6.3.3 Discussion

This in-depth analysis of 6-μm beads travelling through the μHammer demonstrates that the focusing ability and thus the impact performance of our device are strongly influenced by

the parameters encapsulated by the particle Reynolds number, Re_p, including temperature, buffer viscosity, particle velocity, and particle size. As shown in Figure 6.3a, the focusing performance of the device increases for u_S bead-velocity settings when the temperature changes from 8 °C (Re_p = 1.4) to 37 °C (Re_p = 2.5). In Figure 6.2a, we find that the percentage of centered bead impacts at 37 °C was significantly higher than at 8 °C for u_S settings, demonstrating the benefit of this increased focusing ability. The results presented in this chapter also suggest that particle size can have a similar effect on impact performance, since the focusing ability of the μHammer increases with bead size (Figure 6.3d).

While focusing performance is a powerful tool for optimizing impact efficacy, other phenomena influenced by the same parameters that define Re_p must also be considered. For example, the bead streams at 8 °C with u_F bead-velocity settings (Re_p = 2.4, Figure 6.3c) and at 37 °C with u_S settings (Re_p = 2.5, Figure 6.3a) are both tightly focused, but fewer of the bead impacts were centered with u_F settings than with u_S settings (Figure 6.2a). This is likely due to the higher average bead velocity of the u_F settings, which decreases the safety factor for error in overall timing. Furthermore, when the temperature increases from 8 °C (μ = 1.3 mPa·s, Re_p = 2.4) to 37 °C (μ = 0.7 mPa·s, Re_p = 6.0) for u_F settings, the focusing profile shifts (Figure 6.3c). This causes the beads travelling through the stream furthest from the wall (x_{f2}) to move too fast for the μHammer to impact properly, decreasing the percentage of centered impacts (Figure 6.2a). To overcome this unwanted shift in bead trajectory through the device, the results shown in Figure 6.3c indicate that buffer viscosity, μ, can be adjusted independently of temperature by the addition of BSA, thereby restoring the desired flow profile and impact efficacy.

In addition to the parameters encompassed by Re_p, bead concentration and throughput also influence the trajectory of beads through the device and thus affect its overall performance. Figure 6.4a indicates that the focusing capabilities of the μHammer increase with concentration, in agreement with the findings of other studies [116, 127]. However, the percentage of centered beads actually decreased with concentration (Figure 6.2c) due to the negative effect of actuation on bead velocity (Figure 6.4b). This is a function of throughput as opposed to concentration, since beads are only affected if they are detected soon after the previous μHammer actuation. When the throughput increases, the odds that each individual bead will undergo a dramatic change in velocity increases. This, in turn, decreases the percentage of properly timed and centered impacts. As a result, while the highest effective throughput, ω_{eff}, was achieved with a total throughput of 600 beads/s, the highest percentage of centered bead impacts was achieved with a throughput of 300 beads/s. This indicates that efforts to reduce the change in particle velocity with actuation could further increase ω_{eff}.

In order to minimize the detrimental effects of throughput and other phenomena on μHammer timing, the results discussed above suggest a number of design optimizations that could further improve the μHammer's performance (which I will discuss in Section 6.4). However, such changes can be time-consuming and expensive, requiring months to fabricate and validate new designs. In the absence of any geometric changes, the results presented in this chapter also provide a general framework for optimizing device performance immediately by simply adjusting the experimental parameters. For example, decreasing the laser-hammer separation distance, x_{LH}, from 80 to 60 μm can increase the percentage of centered particles by up to 20% with u_S settings (Figure 6.2b). On a more nuanced level, the results presented in Figures 6.2a, 4.12b and 4.13 collectively suggest that reducing the average particle velocity

below u_S settings could improve device performance by increasing the safety factor for error in timing. However, this could also decrease the focusing capability of the device, since it would lower Re_p. This tradeoff could be avoided by increasing the particle volume fraction, φ, which would help restore the focusing performance and thus maximize the effective impact frequency, ω_{eff}. Finally, the results shown in Figure 6.4b indicate that the negative effects of throughput on timing efficacy (Figure 6.2c) could be minimized by adjusting the Tyto's software to automatically sort particles that are too close together in the accelerating particle region. This would allow the μHammer to run at higher throughput values while avoiding the dramatic acceleration of particles after they are detected, reducing the number of burst and missed particles while maximizing ω_{eff}.

It is important to note that the experiments in this study were performed with spherical beads that are orders of magnitude stiffer than the biological cells our device is designed to impact (Young's modulus on the order of GPa for polystyrene versus ~kPa for cells) [108, 131]. Although the deformability of cellular particles adds another degree of complexity, they still can be focused into equilibrium streams in microfluidic channels whose location depends on the ratio of inertial to viscous forces [115, 123, 132, 133]. As shown in Chapters 4 and 5, cells exhibit the same timing characteristics and the same optimal timing settings as beads in the μHammer. In fact, the percent decrease in human leukemic K562 cells after impact with both u_S and u_F velocity settings reported in Chapter 5 is roughly equal to the percentage of beads found in the burst region for the same settings described in this chapter (Figure 6.2a). This provides further evidence that cells impacted in this region are burst as intended, ensuring the uniformity of impact parameters. Furthermore, it demonstrates that beads are a useful tool that can approximate and even predict the μHammer's performance with biological cells.

6.4 Optimization of μHammer design

6.4.1 Methods

As indicated in Section 6.3.3, the results presented throughout this work suggest a number of design optimizations that could further improve the μHammer's performance. For example, since measurement error and bead velocity changes can detrimentally affect timing, the μHammer could be redesigned with a wider hit face (x_{HF} > 28 μm). This would expand the range of centered t_{AC} values and thereby increase the percentage of centered impacts. Furthermore, redesigning the channel geometry by increasing the width of the channel right before the impact face would decrease the fluid velocity in that region. In turn, each particle's velocity would decrease as it passes through that region before impact, further increasing the safety factor for error in timing. Finally, alterations to the channel geometry could be made to help reduce changes in fluidic resistance during actuation. This would decrease the resulting fluidic acceleration that negatively affects μHammer timing, maximizing the percentage of centered impacts at higher throughput values.

To characterize the effectiveness of these potential redesigns, I updated the two-dimensional COMSOL model described in Chapter 4 with these device geometries and modeled the impact of 6-μm diameter particles suspended in buffer. I used these models to track the trajectories of particles travelling through the channel offset from the center (5.5 μm from the wall of the channel with the μHammer at rest, Figure 4.11a) at 37 °C with u_S bead velocity settings. Each device geometry was simulated with a range of different t_{AC} (post-arrival closure time) values to quantify each design's safety factor for error in timing (see Chapter 4 for a detailed description of timing). For each simulation, I measured the distance of the particle from the center of the impact face, x_C, when it first made contact with the

μHammer face (Figure 4.11b). I also recorded the fluid velocity at the center of the particle at the time of initial contact to quantify how the flow profile changes across the μHammer impact face.

6.4.2 Results and discussion

As discussed in Sections 6.2 and 6.3, inertial focusing guides particles into one of two streams on the side of the channel closest to the impact face at rest. Thus, the particles in this experiment were simulated flowing through the channel offset from the center (Figure 4.11a). These particles have an average velocity of 1.15 m/s prior to entering the compression zone, which is the same average velocity as the beads in Chapter 4 that were used to characterize μHammer timing experimentally (Figure 4.12b). As a result, these particles likely correspond to those in the slower bead stream closest to the channel wall (x_{fl}) depicted in Figures 6.3a and 6.3b.

Of all the potential geometric redesigns to improve μHammer performance, widening the impact face to provide a greater safety factor for error in timing is both the simplest to execute and the most likely to have a beneficial effect. In this redesign, the impact face width, x_{HF}, was increased by 50% from its current width of 28 μm to a new width of 42 μm (Figure 6.5). Furthermore, the distance between the back of the impact assembly and the channel wall at full actuation was also increased (from 13 μm to 20 μm). This will reduce the change in fluidic resistance and the resulting fluidic acceleration that accompanies device actuation discussed in Section 6.3.2c, ultimately minimizing the change in velocity for particles that are detected soon after the previous impact (illustrated in Figure 6.4b). As a result, particles are more likely to be properly timed and impacted by the μHammer. This increased distance between the back

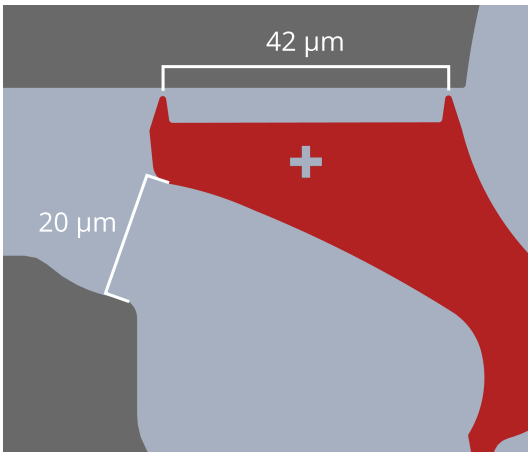

Figure 6.5: µHammer redesign with a 4-µm final gap distance. Note the increased impact face width (42 µm) as well as the increased distance between the back of the µHammer assembly and the channel wall during full actuation (20 µm).

of the impact assembly and the channel wall also makes it less likely that sorted cells (Figure 5.3a) are sheared open by the channel wall or the impact face on their way into the waste channel (as discussed in Section 5.2.2), reducing the amount of cellular debris buildup that can slow down actuation (discussed in the Appendix C).

As shown in Figure 6.6, COMSOL simulations with this redesigned 4-µm final gap device resulted in a total of 14 different t_{AC} (post-arrival closure time) values in which the particles first contacted the impact face within the centered region. This is almost three times the amount of centered t_{AC} values achieved with the current device design in COMSOL simulations (Figure 4.10a, Table 6.1), largely due to the doubled size of the centered region (28-µm wide vs 14-µm wide, Figures 6.6 and 4.10a). Although simulations slightly overestimated the actual number of centered t_{AC} values observed experimentally as discussed in Chapter 4, these results indicate that a wider µHammer face will have a significantly larger safety factor for error in timing than the current design.

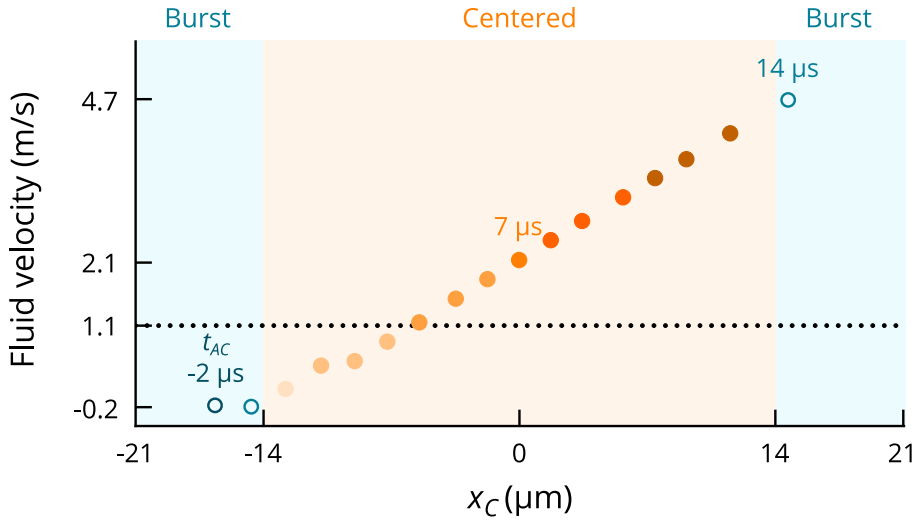

Figure 6.6: Wide face µHammer design results in a greater safety factor for error. Each point represents a different t_{AC} value (from t_{AC} = -2 µs to t_{AC} = 14 µs), plotting the distance of the particle from the center of the impact face at contact, x_C, as well the fluid velocity at the center of the particle at contact. The two outer quadrants (shaded blue, 14 µm < | x_C | < 21 µm) correspond to the "burst" regions, and the two inner quadrants (shaded orange, | x_C | < 14 µm) correspond to the "centered" region. Only t_{AC} values that resulted in particles clearing the pincers and making contact with the impact face are shown. Filled circles shaded orange are used to denote centered t_{AC} values which result in particles first contacting the impact face in the centered region, while open circles shaded blue are used to denote t_{AC} values which first contact the burst region. The maximum and minimum fluid velocities at contact are marked, as well as the fluid velocity for the optimal t_{AC} value (x_C = 0) at contact. Dashed line indicates fluid velocity at center of particle travelling through channel before entering the compression zone (1.15 m/s).

The redesigned 7.5-µm gap device (wide face, Table 6.1) resulted in a similar increase in the number of centered t_{AC} values compared to the current device design. However, it had two fewer centered t_{AC} values compared to the redesigned 4-µm gap device, in addition to a different optimal t_{AC} value (6 vs 7 µs). This is the result of the 7.5-µm gap device's recessed impact face, which causes the particles to initially contact the impact face later than they do with the 4-µm device as shown in Figures 6.7a and b (18 µs vs 16 µs, respectively). In order to eliminate these differences in timing, I adjusted the 7.5-µm gap device's impact face and

Table 6.1: COMSOL simulations of centered impacts with 6 µm beads

Final gap distance x_G	[a] Centered t_{AC} values	[b] Fluid velocity range	[c] Fluid velocity with optimal t_{AC}
4 µm (current)	5	2.2 – 4.5 m/s	3.2 m/s
7.5 µm (current)	4	0.8 – 2.2 m/s	1.6 m/s
4 µm (wide face)	14	-0.2 – 4.1 m/s	2.1 m/s
7.5 µm (wide face)	12	-4.7 – 5.8 m/s	1.2 m/s
7.5 µm (wide face 2.0)	15	-0.3 – 3.8 m/s	1.7 m/s
4 µm (wide face 3.0)	14	0.5 – 3.8 m/s	1.9 m/s

[a] Total number of t_{AC} values that resulted in centered impacts ($|x_C| < 7$ µm for current design and $|x_C| < 14$ µm for wide face redesign).

[b] Fluid velocity measured at center of particle at time of initial contact with µHammer face. Range shown only for centered impacts.

[c] Optimal t_{AC} defined as value that results in $x_C = 0$ µm.

pincer length to be the same as the 4-µm gap device. I then recessed the channel wall to achieve the 7.5-µm final gap distance (Figure 6.7c). This restored the same optimal timing as the 4-µm device (t_{AC} = 7 µs) and actually increased the number of centered t_{AC} values to 15 (Table 6.1, wide face 2.0 design). In this case, the increase in centered t_{AC} values compared to the 4-µm device is likely due to the slightly decreased fluid velocity across the impact face achieved by this design, resulting in a greater safety factor for error in timing (Table 6.1).

In an attempt to explore the benefits of reduced particle velocity on µHammer timing with a 4-µm gap device, I widened the channel leading up to the impact face as shown in Figure 6.7d. While this did result in a slight decrease in fluid velocity across the impact face, it did not increase the number of centered t_{AC} values (wide face 3.0, Table 6.1). This is likely due to the change in orientation of the impact face during contact (Figure 6.7d) compared to previous device iterations. In the future, alternative channel geometries that reduce fluid velocity across the impact face without changing the contact angle should be explored, since they could potentially increase the µHammer's safety factor for error in timing and result in an even greater percentage of centered impacts.

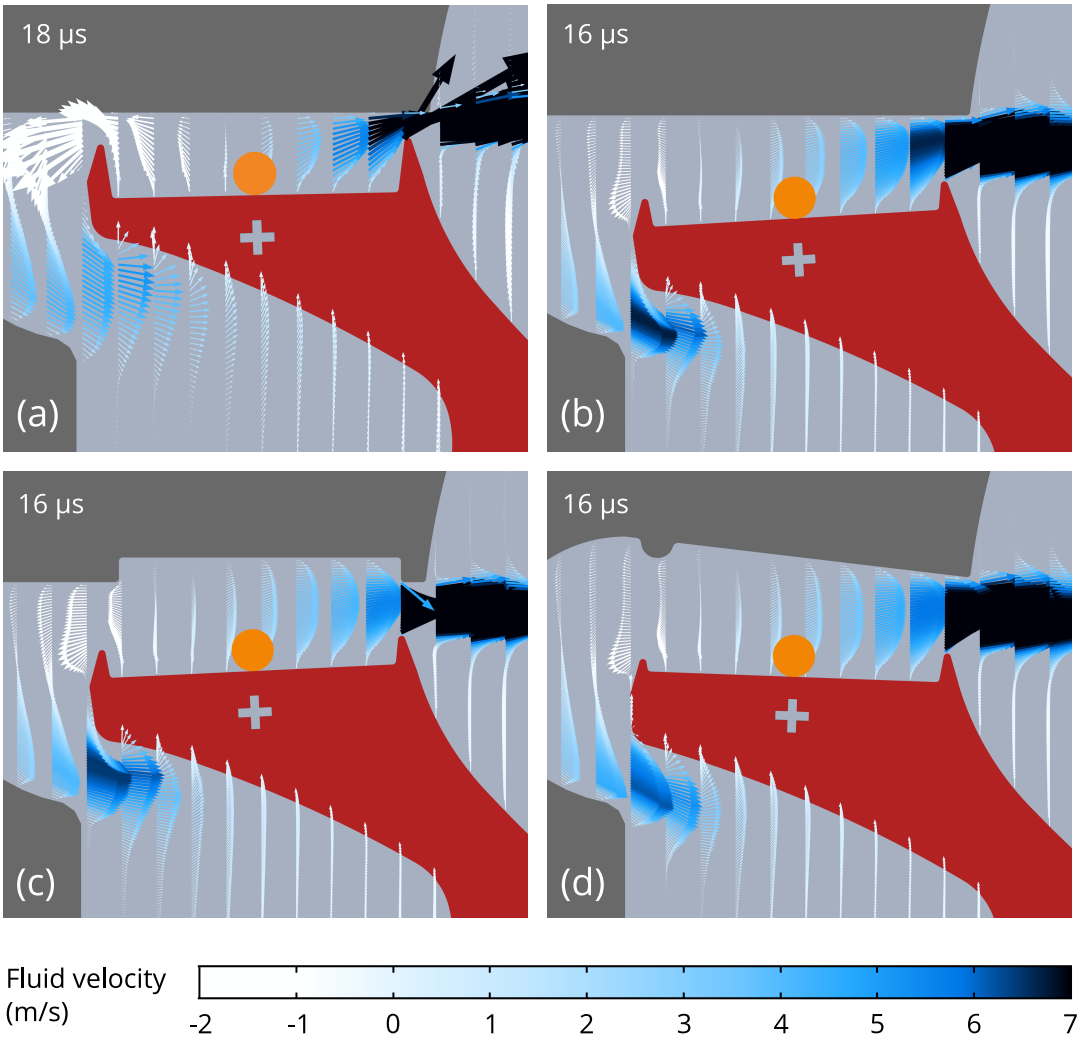

Figure 6.7: COMSOL simulations of optimal (x_C = 0 µm) impacts of 6-µm particles with potential µHammer redesigns. (a) Initial contact of particle with wide face design (7.5-µm final gap) occurs at 18 µs with a t_{AC} value of 6 µs. (b) Initial contact of particle with wide face design (4-µm final gap) occurs at 16 µs with a t_{AC} value of 7 µs. (c) Initial contact of particle with wide face 2.0 design occurs at 16 µs with a t_{AC} value of 7 µs. Note the same impact face geometry as the 4-µm gap distance device combined with the 3.5-µm cutout in the channel wall to achieve a final gap distance of 7.5 µm. (d) Initial contact of particle with wide face 3.0 design (4-µm final gap) occurs at 16 µs. Note the increased channel width upstream of the impact face. Also note the change in angle of the impact face at contact (tilted slightly downstream instead of upstream). In each panel, particles depicted in orange, channel walls in dark grey, µHammer impact assembly in red. Arrows denote direction of flow, with the x-component of the fluid velocity denoted by color gradient.

Chapter 7. Device Applications and Conclusions

7.1 Suitability of μHammer for modeling traumatic impacts

Given the public health and societal ramifications of traumatic brain and joint injuries, understanding the cellular consequences of impacts to brain- and cartilage-associated cells is of much interest. As shown in Table 7.1, the μHammer hit severity parameters (based on a 15-μm-diameter cell) overlap with nearly all of those reported for TBI [17, 28, 41, 49, 61, 63, 66, 134] and cartilage impact [18, 54, 56, 67]. However, it should be noted that these reported parameters were extracted from studies of *ex vivo* (and in some cases *in vivo*) tissue or from tissue-level finite element simulations, due to the lack of cell studies at these high impact rates as discussed in Chapters 1 and 2. Although tissue is typically modeled as a uniform linear viscoelastic material, its material properties are often nonlinear, with high regional heterogeneities and a strong dependence on loading rate [29, 49, 135]. Furthermore, studies have demonstrated that the peak applied strains and strain rates on the microscale are significantly higher than they are on the macroscale [67, 68, 76]. Thus, it can be expected that individual cells undergo more compression and are deformed at a higher rate than the tissue as a whole [73, 75, 136], which would minimize or potentially eliminate the differences in strain rate seen in Table 7.1. Subjecting cells to high impact rates is vital to fully understanding traumatic injuries, since the mechanical properties of cells are highly dependent on strain rate and thus their response to mechanical loading is likely correlated with strain rate as well. The μHammer is uniquely designed to apply such high loading rates on large populations of cells in a controlled manner, making it well-suited to address this need and study the cellular ramifications of traumatic impact on the brain and articular cartilage.

Table 7.1: Comparison of μHammer impact parameters with tissue-level traumatic impacts from literature

Device / Application	Strain	Strain Rate	Stress	Stress Rate	Duration	Velocity[b]
μHammer Capabilities	0 – 100%	30,000 – 200,000 s^{-1}	1 – 100 kPa[a]	100 MPa/s – 100 Gpa/s[a]	10 μs – 2 ms	0.5 m/s – 3 m/s
Cartilage Impact	0 – 60%+	10 – 10,000 s^{-1}	1 – 100 Mpa	10 Mpa/s – 100 Gpa/s	1 ms – 1 s	0.1 m/s – 5 m/s
TBI – Percussive Blast	0 – 30%	10 – 1,000+ s^{-1}	10 kPa – 1 Mpa	1 Mpa/s – 100 Gpa/s	< 1 ms – 10 ms	NA[b]
TBI – Physical Impact	0 – 60%+	10 – 1,000 s^{-1}	10 – 100 kPa	1 Mpa/s – 100 Mpa/s	10 ms – 1 s	1 m/s – 5 m/s

[a]Estimated using Hertz contact model with cell stiffness between 10 and 100 kPa.

[b]Velocity for tissue-level studies based on the impact velocity applied to tissue explants. Blast propagation experiments involve pressure waves but no physical impact and thus are not characterized by impact velocity.

Beyond applications to TBI and cartilage compression, the μHammer can have applications for other cellular force events with similar impact parameters including spinal cord injury [137], shock compression events [138, 139], and surgery [140]. In other cases, for example forces within bone tissue during ambulation [16, 141] and deep tissue injuries [142, 143], loading conditions may change over much slower timescales, but still depend on strain and strain duration. Furthermore, the μHammer could even be of interest in systems typically subject to tensile forces such as tendons and other connective tissue, since the compressive force applied by the μHammer can result in tensional membrane forces and vice versa [143]. Though the forces and various extracellular cues applied by the μHammer to a single cell in suspension likely differ from the exact forces experienced by a cell embedded in tissue *in vivo* (which themselves vary across individuals), the μHammer provides a simplified model system that produces first-in-class information to help fill the existing gap in understanding how mechanical force influences both short- and long-term cell function.

7.2 Future work

7.2.1 µHammer characterization and development

In this document, my collaborators and I have thoroughly characterized the µHammer's timing profile and extensively validated its ability to hit large populations of cells. However, a few different areas of device performance could be made even more robust through further research and development. For example, while the experimental results discussed in Chapters 4 and 5 do not suggest a difference in timing between particles detected with backscatter as opposed to fluorescent signals, a more thorough investigation is recommended to confirm this is the case. This could be achieved by characterizing the µHammer's timing with fluorescent polystyrene microbeads, comparing the optimal timing of solenoid activation while detecting those particles with backscatter to the optimal timing while detecting the same particles with fluorescent signals.

As discussed in Chapter 6, fabricating and characterizing a design with a wider impact face is of much interest as a potential strategy to maximize the percentage of centered impacts. In addition to increasing the safety factor for error in timing, a wider impact face would also provide a clearer distinction between a centered and burst cell impact than the current µHammer design (see Chapters 4 and 5), which could enable the visualization and accurate classification of cell impact locations throughout the depth of the channel. This would allow for a more direct determination of optimal µHammer timing with cells to supplement the experiments described in this document. It is possible, however, that the added mass and increased drag force that accompany a wider impact assembly could significantly slow down actuation or even prevent full closure. If this occurs, then material in the middle of the impact

assembly below the impact face could be removed, creating a cutout that could help limit such changes in actuation.

Another potential area of interest is the development of an even more comprehensive sham-hit control. In Chapter 5, I describe a sham-hit control where cells are flowed through the device without being impacted, subjecting cells to the fluid pressure and other mechanical forces they may experience while passing through the μHammer channel. As accurate as this control may be, it does not include the transient heat and magnetic field generated by the solenoid during actuation. If a more robust sham control is desired, experiments could be performed with a stationary armature that allows for solenoid activation without resulting in μHammer actuation. This could be achieved by designing and fabricating devices with the impact assembly anchored to the surrounding silicon to prevent movement. However, this could also be achieved by flowing buffer through existing devices and then allowing the device to dry completely. As a wetted cartridge dries, the impact assembly is pulled into close contact with the top or bottom of the channel, at which point the interfacial forces lock the assembly into place through a phenomenon called stiction. Although this occurs naturally within a few days after buffer is removed, the process can be expedited by loading a wetted cartridge into the Tyto, removing all buffer from the input chamber with a pipette, then applying a pressure of 500 to 600 mbar to force air through the channel for about an hour. Once locked into place, the interfacial forces holding the device continue to persist even when buffer is re-introduced into the device. Thus, cells can be flowed through the channel while the solenoid is activated without actuating the device, simulating all the inputs applied to a cell during impact except for compression to produce an even more accurate sham-hit population.

7.2.2 μHammer application

Although further development and characterization can continue to improve device performance, the μHammer is already well-suited to interrogate the effects of controlled traumatic impacts on large populations of cells as discussed in Section 7.1. Such work is currently underway with neural progenitor cells (NPCs), whose viability following μHammer impacts of varying magnitude has been explored by Walker et al. in an effort to model the effects of TBI on the cellular level [144]. Future work will explore the more subtle ramifications of traumatic impact on NPCs through microscopy and genetic expression analysis, with timescales ranging from minutes to days after μHammer impact. Proteomic analysis of the proteins secreted by these neural cells (the secretome) could also be performed, both to illuminate the biochemical cascade resulting from a TBI and to identify possible biomarkers for diagnosing brain injury *in vivo*.

In later experiments, the μHammer could be redesigned with an increased channel width to accommodate "microtissue" (in the form of cell aggregates) or cells embedded in a gel "matrix" to explore the effect of cell-cell and cell-matrix interactions during impact. This would provide an intermediate length scale that could link the results from our controlled compression of individual cells with the μHammer to those from other research groups' bulk compression of cell populations and tissue (discussed in Chapter 2). Comparing results across these different length scales would help identify and isolate the contributions of mechanical loading from the contributions of other extracellular interactions in a cell's response to impact. Furthermore, the behavior of different cell types from the brain (e.g. neurons and glial cells) following μHammer impacts could also be studied, either as individual cells or as components of cellular aggregates. This analysis could provide insight into which cell type is most

susceptible to mechanical injury in the brain, which could help guide the development of targeted therapies for TBI. Finally, future work could also explore the response of chondrocytes to a μHammer impact, not only to investigate the cellular ramifications of cartilage impact but also to identify any fundamental responses to dynamic compression that biological cells across different tissues of origin may exhibit.

7.3 Conclusions

In this document, I have described the design, fabrication, and characterization of a high-throughput microfluidic MEMS device capable of applying tunable impacts on the microscale. Using K562 cells as proof-of-concept, my collaborators and I have demonstrated the μHammer's ability to apply consistent sublethal impacts with high strain magnitude and strain rate to large numbers of individual cells. The severity of these impacts can easily be adjusted by altering either the impact duration or impact depth. Furthermore, I have presented the tools to optimize the μHammer's performance under a variety of different experimental conditions by manipulating the inertial focusing of the particles flowing through it. These tools are not just applicable to the μHammer but can ultimately serve as a framework for the design and optimization of other microfluidic devices, especially those that rely on precise particle trajectories and timing like microfluidic flow cytometers [116, 145, 146] and cell sorters [111, 132, 133, 147]. When parameters like temperature or particle size change in these systems, the results presented in this document indicate that it is possible to maintain or even improve device performance by adjusting other parameters including viscosity and flow velocity. Such changes can be implemented immediately, as opposed to more complex geometric redesigns which are often costly and time-consuming to execute, and in some cases are not even possible. These principles provide a simple framework for optimizing any microfluidic device

that is sensitive to its fluid and particle trajectories, enabling flexibility in experimental design without sacrificing efficacy and throughput.

Though some of the experimental systems discussed in this document may be able to approach or even replicate the dynamic force generation of the μHammer, these devices have not been used to apply such controlled high-velocity impacts on such large populations of microscale particles. With the μHammer, these precise loading profiles can be applied to any suspended cell or microscale material (with average diameter between 5 and 16 μm in the existing device iterations), opening doors for microscale materials characterization at high strain rates or investigations of force-induced trauma in a range of biological systems. Due to the μHammer's unprecedented combination of well-defined impact parameters and high throughput, it is uniquely suited to study traumatic impacts on the cellular level. The cell-preserving nature of the μHammer enables a broad range of downstream functional, damage, and stress-related cellular assays. Furthermore, the channel size and hammer width can be adjusted in future designs to accommodate "microtissue" (in the form of cell aggregates) or cells embedded in a gel "matrix" to explore the effect of cell-cell and cell-matrix interactions during impact. Through these and further studies, the mechanisms of cellular damage and recovery in physiologically relevant high strain and strain rate impacts can be elucidated, ultimately leading to an improved understanding of impact-based injuries and their treatment.

References

[1] J. Polkinghorne, "Cultural Context," in *The God of Hope and the End of the World*, pp. 47-48, New Haven, CT: Yale University Press, 2003.

[2] D. E. Ingber, "Cellular mechanotransduction: putting all the pieces together again," *FASEB J,* vol. 20, pp. 811-827, 2006.

[3] M. A. Hemphill, S. Dauth, C. J. Yu, B. E. Dabiri, and K. K. Parker, "Traumatic brain injury and the neuronal microenvironment: a potential role for neuropathological mechanotransduction," *Neuron,* vol. 85, pp. 1177-92, 2015.

[4] S. Kumar, "Cellular mechanotransduction: stiffness does matter," *Nat Mater,* vol. 13, pp. 918-20, 2014.

[5] D. Brindley et al., "Bioprocess forces and their impact on cell behavior: implications for bone regeneration therapy," *J Tissue Eng,* vol. 2011, p. 620247, 2011.

[6] M. A. Hemphill et al., "A possible role for integrin signaling in diffuse axonal injury," *PLoS One,* vol. 6, p. e22899, 2011.

[7] W. Lee, F. Guilak, and W. Liedtke, "Role of piezo channels in joint health and injury," in *Current topics in membranes*. vol. 79, pp. 263-273: Academic Press, 2017.

[8] Y. K. Wang and C. S. Chen, "Cell adhesion and mechanical stimulation in the regulation of mesenchymal stem cell differentiation," *J Cell Mol Med,* vol. 17, pp. 823-832, 2013.

[9] A. J. Keung, S. Kumar, and D. V. Schaffer, "Presentation counts: microenvironmental regulation of stem cells by biophysical and material cues," *Annu Rev Cell Dev Biol,* vol. 26, pp. 533-56, 2010.

[10] M. Sun et al., "Effects of matrix stiffness on the morphology, adhesion, proliferation and osteogenic differentiation of mesenchymal stem cells," *Int J Med Sci,* vol. 15, p. 257, 2018.

[11] J. Klein-Nulend, R. Bacabac, and A. Bakker, "Mechanical loading and how it affects bone cells: the role of the osteocyte cytoskeleton in maintaining our skeleton," *Eur Cell Mater,* vol. 24, pp. 279-291, 2012.

[12] A. Liedert, D. Kaspar, P. Augat, A. Ignatius, and L. Claes, "Mechanobiology of bone tissue and bone cells," in *Mechanosensitivity in cells and tissues*: Academia, 2005.

[13] J. J. Campbell, D. A. Lee, and D. L. Bader, "Dynamic compressive strain influences chondrogenic gene expression in human mesenchymal stem cells," *Biorheology,* vol. 43, pp. 455-470, 2006.

[14] W. S. Leong et al., "Cyclic tensile loading regulates human mesenchymal stem cell differentiation into neuron-like phenotype," *J Tissue Eng Regen Med,* vol. 6, pp. s68-s79, 2012.

[15] H. Cho et al., "Neural differentiation of umbilical cord mesenchymal stem cells by sub-sonic vibration," *Life Sci,* vol. 90, pp. 591-599, 2012.

[16] L. I. Plotkin et al., "Mechanical stimulation prevents osteocyte apoptosis: requirement of integrins, Src kinases, and ERKs," *Am J Physiol Cell Physiol,* vol. 289, pp. C633-C643, 2005.

[17] J. Cheng et al., "Development of a rat model for studying blast-induced traumatic brain injury," *J Neurol Sci,* vol. 294, pp. 23-28, 2010.

[18] N. P. Waters, A. M. Stoker, W. L. Carson, F. M. Pfeiffer, and J. L. Cook, "Biomarkers affected by impact velocity and maximum strain of cartilage during injury," *J Biomech,* vol. 47, pp. 3185-3195, 2014.
[19] K. Franze et al., "Neurite branch retraction is caused by a threshold-dependent mechanical impact," *Biophys J,* vol. 97, pp. 1883-1890, 2009.
[20] M. T. Janet et al., "Mechanical compression drives cancer cells toward invasive phenotype," *Proc Natl Acad Sci,* vol. 109, pp. 911-916, 2012.
[21] H. Zhong et al., "Generation of a co-culture cell micropattern model to simulate lung cancer bone metastasis for anti-cancer drug evaluation," *RSC Adv,* vol. 7, pp. 21837-21847, 2017.
[22] T. Araki, H. Yokota, and A. Morita, "Pediatric traumatic brain injury: characteristic features, diagnosis, and management," *Neurol Med Chir* pp. ra. 2016-0191, 2016.
[23] Centers for Disease Control and Prevention, "Report to Congress on Traumatic Brain Injury in the United States: Epidemiology and Rehabilitation," National Center for Injury Prevention and Control, Atlanta, GA, 2014, Available: https://www.cdc.gov/traumaticbraininjury/pdf/TBI_Report_to_Congress_Epi_and_Rehab-a.pdf
[24] M. H. Nabian, S. A. Zadegan, L. O. Zanjani, and S. R. Mehrpour, "Epidemiology of joint dislocations and ligamentous/tendinous injuries among 2,700 patients: five-year trend of a tertiary center in Iran," *Arch Bone Joint Surg,* vol. 5, p. 426, 2017.
[25] L. Murphy and C. G. Helmick, "The Impact of Osteoarthritis in the United States: A Population-Health PerspectiveA population-based review of the fourth most common cause of hospitalization in US adults," *Orthop Nurs,* vol. 31, pp. 85-91, 2012.
[26] A. C. Thomas, T. Hubbard-Turner, E. A. Wikstrom, and R. M. Palmieri-Smith, "Epidemiology of posttraumatic osteoarthritis," *J Athl Train,* vol. 52, pp. 491-496, 2017.
[27] J. V. Rosenfeld et al., "Blast-related traumatic brain injury," *Lancet Neurol,* vol. 12, pp. 882-893, 2013.
[28] R. K. Gupta and A. Przekwas, "Mathematical models of blast-induced TBI: current status, challenges, and prospects," *Front Neurol,* vol. 4, p. 59, 2013.
[29] D. F. Meaney, B. Morrison, and C. D. Bass, "The mechanics of traumatic brain injury: a review of what we know and what we need to know for reducing its societal burden," *J Biomech Eng,* vol. 136, p. 021008, 2014.
[30] K. Kenney et al., "Cerebral vascular injury in traumatic brain injury," *Exp Neurol,* vol. 275, pp. 353-366, 2016.
[31] R. C. Gardner and K. Yaffe, "Epidemiology of mild traumatic brain injury and neurodegenerative disease," *Mol Cell Neurosci,* vol. 66, pp. 75-80, 2015.
[32] B. P. Lucke-Wold et al., "Linking traumatic brain injury to chronic traumatic encephalopathy: identification of potential mechanisms leading to neurofibrillary tangle development," *J Neurotrauma,* vol. 31, pp. 1129-1138, 2014.
[33] J. Borrelli Jr and W. M. Ricci, "Acute effects of cartilage impact," *Clin Orthop Relat Res,* vol. 423, pp. 33-39, 2004.
[34] M. P. Alexander, "Mild traumatic brain injury: pathophysiology, natural history, and clinical management," *Neurology,* 1995.

[35] J. F. Annegers, W. A. Hauser, S. P. Coan, and W. A. Rocca, "A population-based study of seizures after traumatic brain injuries," *N Engl J Med,* vol. 338, pp. 20-24, 1998.
[36] C. M. McDonough and A. M. Jette, "The contribution of osteoarthritis to functional limitations and disability," *Clin Geriatr Med,* vol. 26, pp. 387-399, 2010.
[37] O. I. Schmidt, M. Infanger, C. E. Heyde, W. Ertel, and P. F. Stahel, "The role of neuroinflammation in traumatic brain injury," *Eur J Trauma,* vol. 30, pp. 135-149, 2004.
[38] A. Mobasheri et al., "The role of metabolism in the pathogenesis of osteoarthritis," *Nat Rev Rheumatol,* vol. 13, pp. 302-311, 2017.
[39] J. H. Lee, J. B. Fitzgerald, M. A. DiMicco, and A. J. Grodzinsky, "Mechanical injury of cartilage explants causes specific time-dependent changes in chondrocyte gene expression," *Arthritis Rheumatol,* vol. 52, pp. 2386-2395, 2005.
[40] T. R. McAdams, K. Mithoefer, J. M. Scopp, and B. R. Mandelbaum, "Articular cartilage injury in athletes," *Cartilage,* vol. 1, pp. 165-179, 2010.
[41] E. Bar-Kochba, M. T. Scimone, J. B. Estrada, and C. Franck, "Strain and rate-dependent neuronal injury in a 3D in vitro compression model of traumatic brain injury," *Sci Rep,* vol. 6, p. 30550, 2016.
[42] O. Loh, A. Vaziri, and H. D. Espinosa, "The potential of MEMS for advancing experiments and modeling in cell mechanics," *Exp Mech,* vol. 49, pp. 105-124, 2009.
[43] Q. Li, G. Lee, C. Ong, and C. Lim, "AFM indentation study of breast cancer cells," *Biochem Biophys Res Commun,* vol. 374, pp. 609-613, 2008.
[44] M. P. Stewart, Y. Toyoda, A. A. Hyman, and D. J. Muller, "Tracking mechanics and volume of globular cells with atomic force microscopy using a constant-height clamp," *Nat Protoc,* vol. 7, pp. 143-154, 2012.
[45] B. P. Chan, C. H. Li, K. L. Au-Yeung, K. Y. Sze, and A. H. Ngan, "A microplate compression method for elastic modulus measurement of soft and viscoelastic collagen microspheres," *Ann Biomed Eng,* vol. 36, pp. 1254-67, 2008.
[46] N. A. Zacchia and M. T. Valentine, "Design and optimization of arrays of neodymium iron boron-based magnets for magnetic tweezers applications," *Rev Sci Instrum,* vol. 86, p. 053704, 2015.
[47] E. Peeters, C. Oomens, C. Bouten, D. Bader, and F. Baaijens, "Mechanical and failure properties of single attached cells under compression," *J Biomech,* vol. 38, pp. 1685-1693, 2005.
[48] H. Takamatsu and N. Kumagae, "Survival of biological cells deformed in a narrow gap," *J Biomech Eng,* vol. 124, pp. 780-3, 2002.
[49] F. Pervin and W. W. Chen, "Dynamic mechanical response of bovine gray matter and white matter brain tissues under compression," *J Biomech,* vol. 42, pp. 731-735, 2009.
[50] D. Desmaële, M. Boukallel, and S. Régnier, "Actuation means for the mechanical stimulation of living cells via microelectromechanical systems: A critical review," *J Biomech,* vol. 44, pp. 1433-1446, 2011.
[51] M. Smith, "Monitoring intracranial pressure in traumatic brain injury," *Anesth Analg,* vol. 106, pp. 240-8, 2008.
[52] W. Hodge et al., "Contact pressures in the human hip joint measured in vivo," *Proc Natl Acad Sci,* vol. 83, pp. 2879-2883, 1986.

[53] J. Ghajar, "Traumatic brain injury," *Lancet,* vol. 356, pp. 923-929, 2000.
[54] R. Aspden, J. Jeffrey, and L. Burgin, "Impact loading: physiological or pathological?," *Osteoarthr Cartil,* vol. 10, pp. 588-589, 2002.
[55] J. Bingham et al., "In vivo cartilage contact deformation in the healthy human tibiofemoral joint," *Rheumatology,* vol. 47, pp. 1622-1627, 2008.
[56] Z. Abusara, M. Von Kossel, and W. Herzog, "In vivo dynamic deformation of articular cartilage in intact joints loaded by controlled muscular contractions," *PLoS One,* vol. 11, p. e0147547, 2016.
[57] F. Clausen and L. Hillered, "Intracranial pressure changes during fluid percussion, controlled cortical impact and weight drop injury in rats," *Acta Neurochir,* vol. 147, pp. 775-780, 2005.
[58] W. T. O'Connor, A. Smyth, and M. D. Gilchrist, "Animal models of traumatic brain injury: a critical evaluation," *Pharmacol Ther,* vol. 130, pp. 106-113, 2011.
[59] Y. Xiong, A. Mahmood, and M. Chopp, "Animal models of traumatic brain injury," *Nat Rev Neurosci,* vol. 14, pp. 128-142, 2013.
[60] D. I. Shreiber, A. C. Bain, and D. F. Meaney, "In vivo thresholds for mechanical injury to the blood-brain barrier," *SAE Trans,* pp. 3792-3806, 1997.
[61] F. Hernandez et al., "Six degree-of-freedom measurements of human mild traumatic brain injury," *Ann Biomed Eng,* vol. 43, pp. 1-17, 2014.
[62] L. Zhang, K. H. Yang, and A. I. King, "A proposed injury threshold for mild traumatic brain injury," *J Biomech Eng,* vol. 126, pp. 226-236, 2004.
[63] M. B. Panzer, B. S. Myers, B. P. Capehart, and C. R. Bass, "Development of a finite element model for blast brain injury and the effects of CSF cavitation," *Ann Biomed Eng,* vol. 40, pp. 1530-1544, 2012.
[64] P. A. Taylor and C. C. Ford, "Simulation of blast-induced early-time intracranial wave physics leading to traumatic brain injury," *J Biomech Eng,* vol. 131, p. 061007, 2009.
[65] B. Rashid, M. Destrade, and M. D. Gilchrist, "Mechanical characterization of brain tissue in compression at dynamic strain rates," *J Mech Behav Biomed Mater,* vol. 10, pp. 23-38, 2012.
[66] H. Mao et al., "Finite element analysis of controlled cortical impact-induced cell loss," *J Neurotrauma,* vol. 27, pp. 877-888, 2010.
[67] L. R. Bartell, L. A. Fortier, L. J. Bonassar, and I. Cohen, "Measuring microscale strain fields in articular cartilage during rapid impact reveals thresholds for chondrocyte death and a protective role for the superficial layer," *J Biomech,* vol. 48, pp. 3440-3446, 2015.
[68] C. R. Henak, L. R. Bartell, I. Cohen, and L. J. Bonassar, "Multiscale strain as a predictor of impact-induced fissuring in articular cartilage," *J Biomech Eng,* vol. 139, 2017.
[69] B. Ewers, D. Dvoracek-Driksna, M. Orth, and R. Haut, "The extent of matrix damage and chondrocyte death in mechanically traumatized articular cartilage explants depends on rate of loading," *J Orthop Res,* vol. 19, pp. 779-784, 2001.
[70] D. Milentijevic, I. F. Rubel, A. S. Liew, D. L. Helfet, and P. A. Torzilli, "An in vivo rabbit model for cartilage trauma: a preliminary study of the influence of impact stress magnitude on chondrocyte death and matrix damage," *J Orthop Trauma,* vol. 19, pp. 466-473, 2005.

[71] J. Borrelli Jr, M. E. Burns, W. M. Ricci, and M. J. Silva, "A method for delivering variable impact stresses to the articular cartilage of rabbit knees," *J Orthop Trauma,* vol. 16, pp. 182-188, 2002.
[72] S. N. Robinovitch and J. Chiu, "Surface stiffness affects impact force during a fall on the outstretched hand," *J Orthop Res,* vol. 16, pp. 309-313, 1998.
[73] R. G. Breuls, B. G. Sengers, C. W. Oomens, C. V. Bouten, and F. P. Baaijens, "Predicting local cell deformations in engineered tissue constructs: a multilevel finite element approach," *J Biomech Eng,* vol. 124, pp. 198-207, 2002.
[74] M. R. Buckley, A. J. Bergou, J. Fouchard, L. J. Bonassar, and I. Cohen, "High-resolution spatial mapping of shear properties in cartilage," *J Biomech,* vol. 43, pp. 796-800, 2010.
[75] F. Guilak and V. C. Mow, "The mechanical environment of the chondrocyte: a biphasic finite element model of cell–matrix interactions in articular cartilage," *J Biomech,* vol. 33, pp. 1663-1673, 2000.
[76] M. L. Upton, C. L. Gilchrist, F. Guilak, and L. A. Setton, "Transfer of macroscale tissue strain to microscale cell regions in the deformed meniscus," *Biophys J,* vol. 95, pp. 2116-2124, 2008.
[77] G. G. Scott, S. S. Margulies, and B. Coats, "Utilizing multiple scale models to improve predictions of extra-axial hemorrhage in the immature piglet," *Biomech Model Mechanobiol,* vol. 15, pp. 1101-1119, 2016.
[78] X. Wang, A. J. Neely, G. G. McIlwaine, and C. J. Lueck, "Multi-scale analysis of optic chiasmal compression by finite element modelling," *J Biomech,* vol. 47, pp. 2292-2299, 2014.
[79] D. Meaney, "Relationship between structural modeling and hyperelastic material behavior: application to CNS white matter," *Biomech Model Mechanobiol,* vol. 1, pp. 279-293, 2003.
[80] S. A. Lippert, E. M. Rang, and M. J. Grimm, "The high frequency properties of brain tissue," *Biorheology,* vol. 41, pp. 681-691, 2004.
[81] S. S. Margulies, L. E. Thibault, and T. A. Gennarelli, "Physical model simulations of brain injury in the primate," *J Biomech,* vol. 23, pp. 823-36, 1990.
[82] B. J. Pfister, T. P. Weihs, M. Betenbaugh, and G. Bao, "An in vitro uniaxial stretch model for axonal injury," *Ann Biomed Eng,* vol. 31, pp. 589-598, 2003.
[83] T. A. Lusardi, J. A. Wolf, M. E. Putt, D. H. Smith, and D. F. Meaney, "Effect of acute calcium influx after mechanical stretch injury in vitro on the viability of hippocampal neurons," *J Neurotrauma,* vol. 21, pp. 61-72, 2004.
[84] M. D. Tang-Schomer, A. R. Patel, P. W. Baas, and D. H. Smith, "Mechanical breaking of microtubules in axons during dynamic stretch injury underlies delayed elasticity, microtubule disassembly, and axon degeneration," *FASEB J,* vol. 24, pp. 1401-1410, 2010.
[85] E. Ellis, J. McKinney, K. Willoughby, S. Liang, and J. Povlishock, "A new model for rapid stretch-induced injury of cells in culture: characterization of the model using astrocytes," *J Neurotrauma,* vol. 12, pp. 325-339, 1995.
[86] C. J. Hunter, S. M. Imler, P. Malaviya, R. M. Nerem, and M. E. Levenston, "Mechanical compression alters gene expression and extracellular matrix synthesis by chondrocytes cultured in collagen I gels," *Biomaterials,* vol. 23, pp. 1249-1259, 2002.

[87] K. Dennis, "Mechanical Modification of Cells by Pressure Waves and Its Application to Traumatic Brain Injury," University of Ottawa, 2016.
[88] K. C. Neuman and S. M. Block, "Optical trapping," *Rev Sci Instrum,* vol. 75, pp. 2787-809, 2004.
[89] K. C. Neuman and A. Nagy, "Single-molecule force spectroscopy: optical tweezers, magnetic tweezers and atomic force microscopy," *Nat Methods,* vol. 5, pp. 491-505, 2008.
[90] J. Lin and M. T. Valentine, "High-force NdFeB-based magnetic tweezers device optimized for microrheology experiments," *Rev Sci Instrum,* vol. 83, p. 053905, 2012.
[91] O. Chaudhuri, S. H. Parekh, W. A. Lam, and D. A. Fletcher, "Combined atomic force microscopy and side-view optical imaging for mechanical studies of cells," *Nat Methods,* vol. 6, pp. 383-7, 2009.
[92] B. A. Smith, B. Tolloczko, J. G. Martin, and P. Grütter, "Probing the viscoelastic behavior of cultured airway smooth muscle cells with atomic force microscopy: stiffening induced by contractile agonist," *Biophys J,* vol. 88, pp. 2994-3007, 2005.
[93] T. D. Nguyen and Y. Gu, "Determination of strain-rate-dependent mechanical behavior of living and fixed osteocytes and chondrocytes using atomic force microscopy and inverse finite element analysis," *J Biomech Eng,* vol. 136, 2014.
[94] V. Lulevich, T. Zink, H.-Y. Chen, F.-T. Liu, and G.-y. Liu, "Cell mechanics using atomic force microscopy-based single-cell compression," *Langmuir,* vol. 22, pp. 8151-8155, 2006.
[95] Z. Zhang, M. Ferenczi, A. Lush, and C. Thomas, "A novel micromanipulation technique for measuring the bursting strength of single mammalian cells," *Appl Microbiol Biotechnol,* vol. 36, pp. 208-210, 1991.
[96] K. Van Vliet, G. Bao, and S. Suresh, "The biomechanics toolbox: experimental approaches for living cells and biomolecules," *Acta Mater,* vol. 51, pp. 5881-5905, 2003.
[97] J. Brugués et al., "Dynamical organization of the cytoskeletal cortex probed by micropipette aspiration," *Proc Natl Acad Sci,* vol. 107, pp. 15415-15420, 2010.
[98] E. M. Darling and D. Di Carlo, "High-throughput assessment of cellular mechanical properties," *Ann Rev Biomed Eng,* vol. 17, pp. 35-62, 2015.
[99] A. Adamo et al., "Microfluidics-based assessment of cell deformability," *Anal Chem,* vol. 84, pp. 6438-6443, 2012.
[100] J. Mancuso and W. Ristenpart, "Stretching of red blood cells at high strain rates," *Phys Rev Fluids,* vol. 2, p. 101101, 2017.
[101] J. S. Dudani, D. R. Gossett, T. Henry, and D. Di Carlo, "Pinched-flow hydrodynamic stretching of single-cells," *Lab Chip,* vol. 13, pp. 3728-3734, 2013.
[102] D. R. Gossett et al., "Hydrodynamic stretching of single cells for large population mechanical phenotyping," *Proc Natl Acad Sci,* vol. 109, pp. 7630-7635, 2012.
[103] B. Barazani, S. Warnat, A. Fine, and T. Hubbard, "MEMS squeezer for the measurement of single cell rupture force, stiffness change, and hysteresis," *J Micromech Microeng,* vol. 27, p. 025002, 2016.
[104] Y. Takayama et al., "Developing a MEMS device with built-in microfluidics for biophysical single cell characterization," *Micromachines,* vol. 9, p. 275, 2018.

[105] J. S. Foster et al., "Cell sorting system using microfabricated components," U.S. Patent 9 604 214 B2, Mar. 28, 2017.
[106] J. S. Foster et al., "Particle manipulation system with out-of-plane channel and focusing element," U.S. Patent 9 404 838 B2, Aug. 2, 2016.
[107] J. S. Foster, D. W. Grummitt, J. K. Spong, K. L. Turner, and J. C. Harley, "MEMS particle sorting actuator and method of manufacture," U.S. Patent 9 372 185 B2, Jun. 21, 2016.
[108] Y. Luo et al., "A constriction channel based microfluidic system enabling continuous characterization of cellular instantaneous Young's modulus," *Sens Actuators B Chem,* vol. 202, pp. 1183-1189, 2014.
[109] Z. Zhang, H. Kristiansen, and J. Liu, "A method for determining elastic properties of micron-sized polymer particles by using flat punch test," *Comput Mater Sci,* vol. 39, pp. 305-314, 2007.
[110] B. Fabry et al., "Scaling the microrheology of living cells," *Phys Rev Lett,* vol. 87, p. 148102, 2001.
[111] J. S. Foster, K. Shields, and M. R. Hoonejani, "Particle manipulation system with out-of-plane channel and variable cross section focusing element," U.S. Patent 9 962 702 B2, May 8, 2018.
[112] R. Clift, J. R. Grace, and M. E. Weber, *Bubbles, drops, and particles*: Courier Corporation, 2005.
[113] E. S. Asmolov, "The inertial lift on a spherical particle in a plane Poiseuille flow at large channel Reynolds number," *J Fluid Mech,* vol. 381, pp. 63-87, 1999.
[114] J. Zhang et al., "Fundamentals and applications of inertial microfluidics: a review," *Lab Chip,* vol. 16, pp. 10-34, 2016.
[115] D. Di Carlo, D. Irimia, R. G. Tompkins, and M. Toner, "Continuous inertial focusing, ordering, and separation of particles in microchannels," *Proc Natl Acad Sci,* vol. 104, pp. 18892-18897, 2007.
[116] J. Oakey et al., "Particle focusing in staged inertial microfluidic devices for flow cytometry," *Anal Chem,* vol. 82, pp. 3862-3867, 2010.
[117] S. Wang, X. Huang, and C. Yang, "Mixing enhancement for high viscous fluids in a microfluidic chamber," *Lab Chip,* vol. 11, pp. 2081-2087, 2011.
[118] J. D. Tice, A. D. Lyon, and R. F. Ismagilov, "Effects of viscosity on droplet formation and mixing in microfluidic channels," *Anal Chim Acta,* vol. 507, pp. 73-77, 2004.
[119] A. M. Leshansky, A. Bransky, N. Korin, and U. Dinnar, "Tunable nonlinear viscoelastic “focusing” in a microfluidic device," *Phys Rev Lett,* vol. 98, p. 234501, 2007.
[120] D. Lee, S. M. Nam, J.-a. Kim, D. Di Carlo, and W. Lee, "Active control of inertial focusing positions and particle separations enabled by velocity profile tuning with coflow systems," *Anal Chem,* vol. 90, pp. 2902-2911, 2018.
[121] A. A. S. Bhagat, S. S. Kuntaegowdanahalli, and I. Papautsky, "Inertial microfluidics for continuous particle filtration and extraction," *Microfluid Nanofluid,* vol. 7, pp. 217-226, 2009.
[122] D. Di Carlo, "Inertial microfluidics," *Lab Chip,* vol. 9, pp. 3038-3046, 2009.
[123] X. Wang, M. Zandi, C.-C. Ho, N. Kaval, and I. Papautsky, "Single stream inertial focusing in a straight microchannel," *Lab Chip,* vol. 15, pp. 1812-1821, 2015.

[124] A. E. Reece and J. Oakey, "Long-range forces affecting equilibrium inertial focusing behavior in straight high aspect ratio microfluidic channels," *Phys Fluids,* vol. 28, p. 043303, 2016.
[125] S. Kahkeshani, H. Haddadi, and D. Di Carlo, "Preferred interparticle spacings in trains of particles in inertial microchannel flows," *J Fluid Mech,* vol. 786, 2016.
[126] K. J. Humphry, P. M. Kulkarni, D. A. Weitz, J. F. Morris, and H. A. Stone, "Axial and lateral particle ordering in finite Reynolds number channel flows," *Phys Fluids,* vol. 22, p. 081703, 2010.
[127] A. J. Chung et al., "Microstructure-induced helical vortices allow single-stream and long-term inertial focusing," *Lab Chip,* vol. 13, pp. 2942-2949, 2013.
[128] G.-B. Lee, C.-C. Chang, S.-B. Huang, and R.-J. Yang, "The hydrodynamic focusing effect inside rectangular microchannels," *J Micromech Microeng,* vol. 16, p. 1024, 2006.
[129] F. M. White and I. Corfield, *Viscous fluid flow*, vol. 3, New York: McGraw-Hill, 2006.
[130] K. Monkos, "Viscosity of bovine serum albumin aqueous solutions as a function of temperature and concentration," *Int J Biol Macromol,* vol. 18, pp. 61-68, 1996.
[131] R. Hiorns, *Polymer Handbook*, 4th ed., vol. 49, New York: John Wiley and Sons, 2000.
[132] S. C. Hur, N. K. Henderson-MacLennan, E. R. McCabe, and D. Di Carlo, "Deformability-based cell classification and enrichment using inertial microfluidics," *Lab Chip,* vol. 11, pp. 912-920, 2011.
[133] E. Ozkumur et al., "Inertial focusing for tumor antigen–dependent and–independent sorting of rare circulating tumor cells," *Sci Transl Med,* vol. 5, p. 179ra47, 2013.
[134] I. Cernak, "Animal models of head trauma," *NeuroRx,* vol. 2, pp. 410-422, 2005.
[135] D. B. MacManus, J. G. Murphy, and M. D. Gilchrist, "Mechanical characterisation of brain tissue up to 35% strain at 1, 10, and 100/s using a custom-built micro-indentation apparatus," *J Mech Behav Biomed Mater,* vol. 87, pp. 256-266, 2018.
[136] J. Wu and W. Herzog, "Finite element simulation of location-and time-dependent mechanical behavior of chondrocytes in unconfined compression tests," *Ann Biomed Eng,* vol. 28, pp. 318-330, 2000.
[137] A. Saari, E. Itshayek, and P. A. Cripton, "Cervical spinal cord deformation during simulated head-first impact injuries," *J Biomech,* vol. 44, pp. 2565-2571, 2011.
[138] H. Saraf, K. Ramesh, A. Lennon, A. Merkle, and J. Roberts, "Mechanical properties of soft human tissues under dynamic loading," *J Biomech,* vol. 40, pp. 1960-1967, 2007.
[139] B. Song, W. Chen, Y. Ge, and T. Weerasooriya, "Dynamic and quasi-static compressive response of porcine muscle," *J Biomech,* vol. 40, pp. 2999-3005, 2007.
[140] J. McGuire, I. Wright, and J. Leverment, "An in vitro assessment of tissue compression damage during circular stapler approximation tests, measuring expulsion of intracellular fluid and force," *Proc Inst of Mech Eng H,* vol. 215, pp. 589-597, 2001.
[141] J.-L. Milan, J. A. Planell, and D. Lacroix, "Simulation of bone tissue formation within a porous scaffold under dynamic compression," *Biomech Model Mechanobiol,* vol. 9, pp. 583-596, 2010.

[142] R. Breuls, C. Bouten, C. Oomens, D. Bader, and F. Baaijens, "Compression induced cell damage in engineered muscle tissue: an in vitro model to study pressure ulcer aetiology," *Ann Biomed Eng,* vol. 31, pp. 1357-1364, 2003.
[143] N. Slomka, S. Or-Tzadikario, D. Sassun, and A. Gefen, "Membrane-stretch-induced cell death in deep tissue injury: computer model studies," *Cell Mol Bioeng,* vol. 2, p. 118, 2009.
[144] J. L. Walker et al., "Controlled Single-Cell Compression With a High-Throughput MEMS Actuator," *J Microelectromech Syst*, Advance online publication, DOI:10.1109/JMEMS.2020.3005514, 2020.
[145] A. A. S. Bhagat, S. S. Kuntaegowdanahalli, N. Kaval, C. J. Seliskar, and I. Papautsky, "Inertial microfluidics for sheath-less high-throughput flow cytometry," *Biomed Microdevices,* vol. 12, pp. 187-195, 2010.
[146] T. Sun and H. Morgan, "Single-cell microfluidic impedance cytometry: a review," *Microfluid Nanofluid,* vol. 8, pp. 423-443, 2010.
[147] A. A. S. Bhagat et al., "Microfluidics for cell separation," *Med Biol Eng Comput,* vol. 48, pp. 999-1014, 2010.

Appendix

A. Scanning electron microscope images

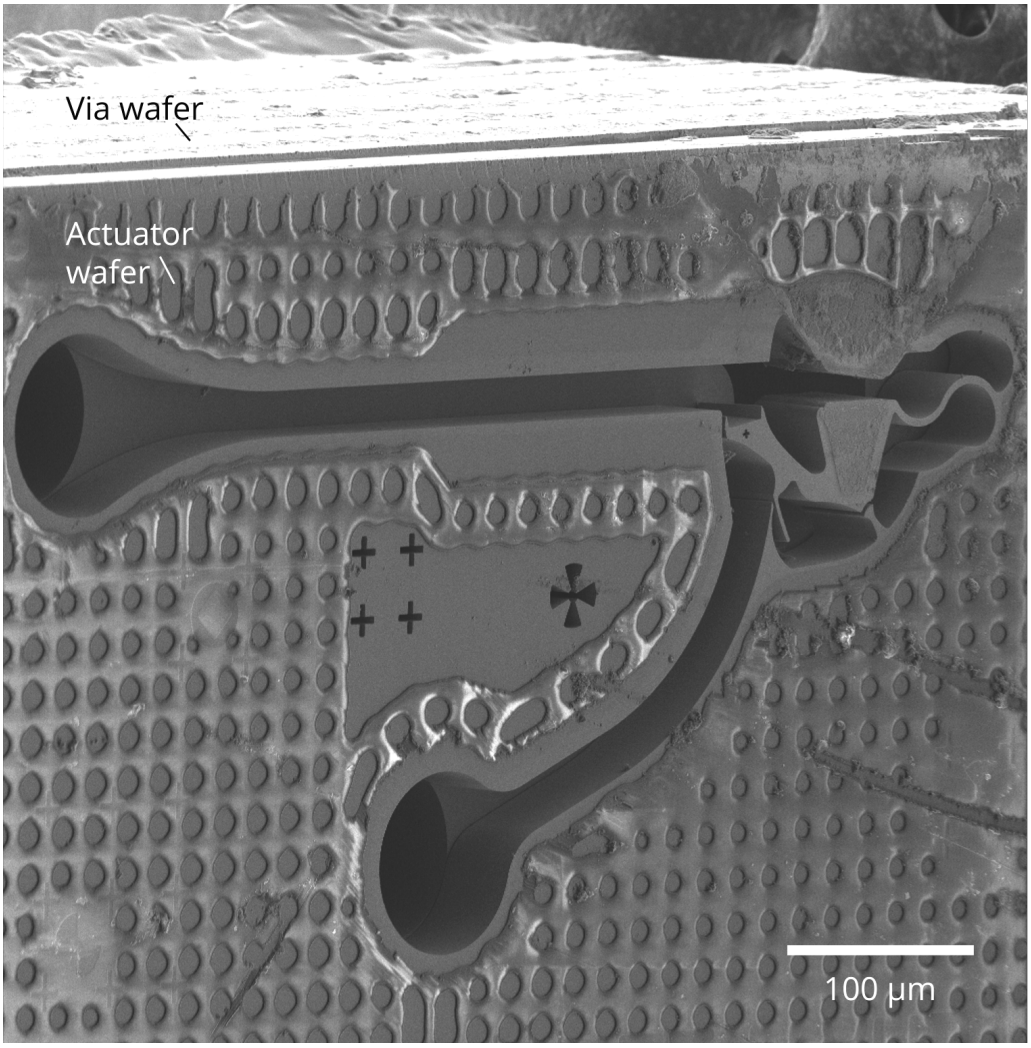

Figure A.1: Scanning electron microscope (SEM) image of µHammer with glass cover removed. Note the depth of the via wafer beneath the actuator wafer (described in Appendix B). All SEM images acquired at a 45-degree angle to highlight all three dimensions of the chip, with settings of 5.00 kV HV, 0.20 nA current, and 30 mm working distance using an Everhart-Thornley detector.

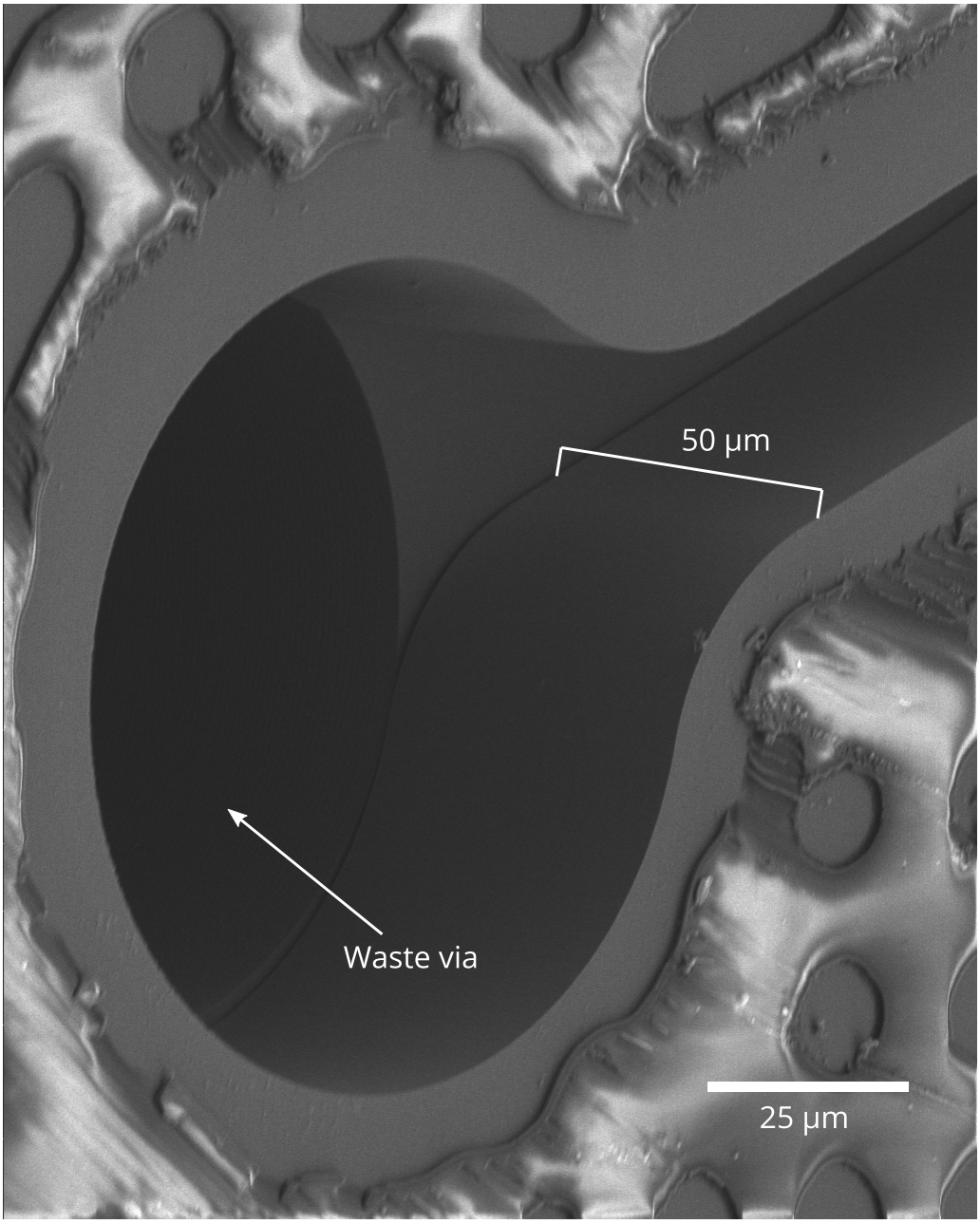

Figure A.2: SEM closeup of µHammer channel leading to waste output via. Depth of µHammer channel (50 µm) is marked. The three vias (input, waste, and hit cell output) all travel through the depth of the via wafer to interface with the macroscale interposer on the other side (Figure 5.1).

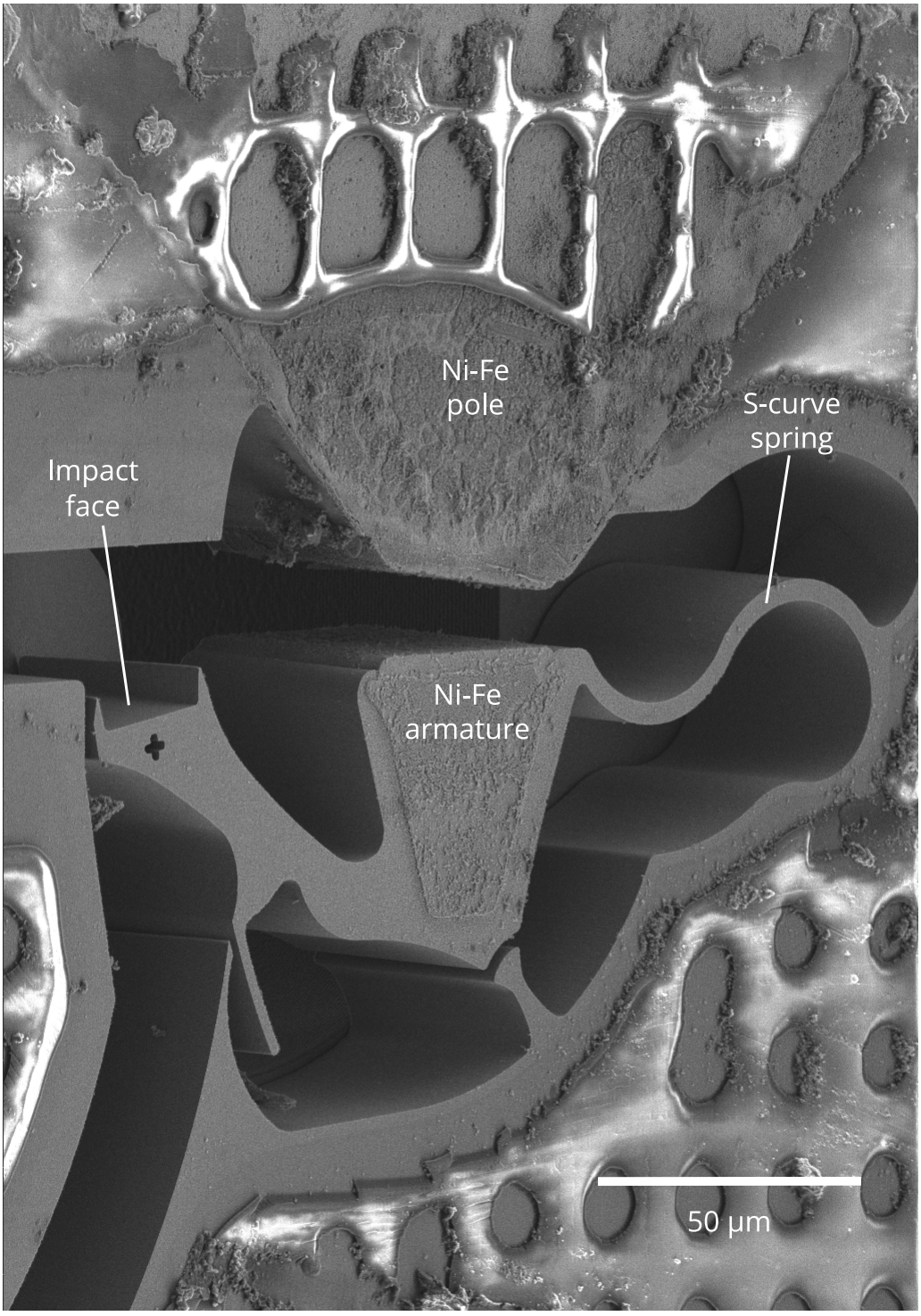

Figure A.3: SEM closeup of released µHammer impact assembly and Ni–Fe pole. Note how the impact assembly extends throughout the depth of the channel, with the Ni–Fe armature located over the output via (deep black shadow). Hit cells pass underneath the armature into the output via on their way to the output chamber of the cartridge.

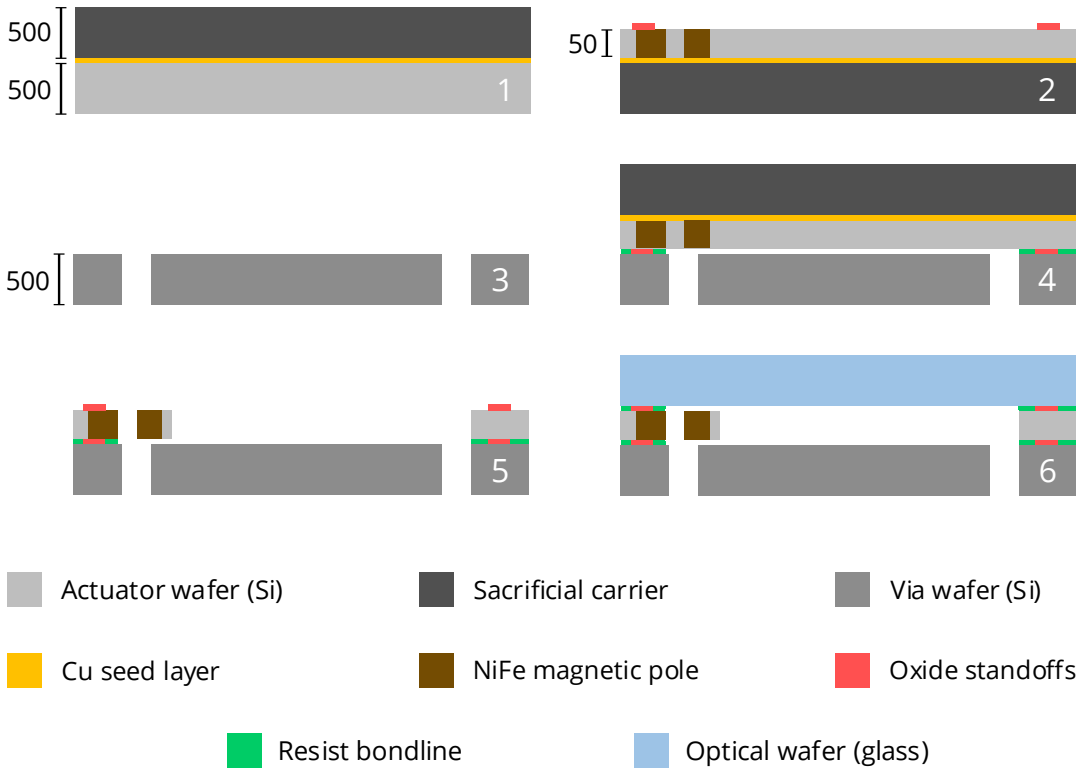

Figure A.4 : µHammer fabrication process flow. Steps 1 – 2: actuator wafer fabrication. Step 3: via wafer fabrication. Steps 4 – 6: final device assembly. 1: Deposit copper seed layer on single-crystal silicon actuator wafer, then bond it with sacrificial carrier. 2: Flip wafer and grind/polish actuator wafer layer down. Etch silicon, then electroplate Ni–Fe on exposed copper seed layer. Deposit and etch oxide standoffs. 3: Etch vias through fresh silicon via wafer. 4: Use photoresist to bond via wafer to actuator wafer. 5: Remove sacrificial carrier and copper seed layer. Etch channels through actuator wafer. Deposit and etch oxide standoffs. 6: Bond glass optical wafer with photoresist on top of actuator wafer to seal etched channels from environment. All distances in microns, images not to scale. Figure adapted from Owl biomedical.

B. Device fabrication

The device is fabricated by Innovative Micro Technology, Inc. (USA) using a 14-layer process. This process can be divided into 3 main steps: etching the silicon actuator wafer, etching the silicon via wafer, and bonding the components together (Figure A.4).

The actuator wafer begins as 500 μm of single crystal silicon. Copper is deposited onto the surface of the silicon, after which a 500-μm thick silicon wafer is bonded to the copper as a carrier wafer. The actuator wafer is then ground to a thickness of 60 μm, and subsequently planarized with chemical mechanical polishing to a thickness of 50 μm. The actuator wafer is etched via Deep Reactive Ion Etching (DRIE) with the Bosch process all the way through the silicon, exposing the copper seed layer for deposition of the 45/55 Ni–Fe poles. These are deposited using electrochemical plating in an Ni–Fe bath, after which the poles are polished down to the silicon wafer surface. Finally, a 1-μm layer of oxide is deposited on the surface and etched via Reactive Ion Etching (RIE) to form standoffs that control the thickness of the bond line to the via wafer in later steps.

The via wafer is 500-μm thick single-crystal silicon. Oxide is deposited on both sides, then RIE etched to serve as a mask for the subsequent DRIE etch through the wafer to form the vias. The oxide is removed to finish the via wafer fabrication.

To bond the 2 wafers together, photoresist is deposited and patterned on the surface of the actuator wafer. The via wafer is placed on the oxide standoffs then adhered to the actuator wafer by polymerizing the photoresist, after which the carrier silicon wafer and copper seed layer are removed from the actuator wafer. Next, the channels and μHammer features are DRIE etched all the way through the exposed actuator wafer. To finish the fabrication process, a 1-μm oxide layer is deposited as a standoff and the exposed surface of the actuator wafer is bonded to glass with photoresist, sealing the μHammer chip from the external environment.

C. μHammer durability and repeatability

During each experiment, the silicon, Ni–Fe, and overall geometric structure of the μHammer device showed no observable degradation. As the experiment progressed, the

actuation profile of the μHammer (as shown in Figure 4.2) could shift along the time axis so that full actuation occurred up to 1 μs later, likely due to the build-up of cellular debris. This occurred most often at higher temperatures (i.e. 37 °C), indicating that the accumulation of cellular debris between the impact face and the top / bottom of the channel is exacerbated by increased temperature. However, the changes in timing and velocity profile of the device that accompanied changes in the time to full actuation, t_{SC}, were negligible and thus did not affect the overall experiment under most conditions. The exception to this rule occurred when the hold time of impact was sufficiently long (on the order of 1 ms) and the experimental temperature was sufficiently high (37 °C) that the device slowed down significantly (t_{SC} increased by at least 2 μs), sometimes to the point where the device stopped actuating completely. This likely occurs due to the high number of cells being sorted into the waste chamber at these settings (~10% of the total population). Since the μHammer is not designed to gently sort cells, a significant percentage of cells passing through the 13-μm gap into the waste via (Figure 5.3a) are likely sheared open. This ultimately results in a significant buildup of cellular debris in the region where the μHammer is at rest, detrimentally affecting the μHammer's ability to actuate consistently. Future designs may be able to avoid this undesired result by providing a wider path to sort cells more gently as described in Chapter 6.

To minimize other sources of degradation of device performance, including contamination and clogging, each μHammer cartridge was used for only 1 day of experiments (typically lasting several hours) and then discarded. The cells were also filtered twice before being flowed through the device to reduce the risk of clogging. Less than 5% of devices have clogged through experiments across different cell types and average diameters. Furthermore,

the actuation profile of each device was assessed before and after each experiment to ensure proper actuation and to confirm the proper timing for that device.

D. Fine-tuning μHammer closure time

As described in Section 5.2.1b, the μHammer has a mixing apparatus in the input chamber to ensure the solution is well-mixed throughout the experiment. This apparatus is rotated like a propeller by the rotation of an external permanent magnet in the alignment stage adjacent to the input chamber. Since this rotating magnet is relatively close to the μHammer chip (within 50 mm), it subtly affects the net magnetic force applied to the released μHammer armature as the magnet rotates. The magnitude of this effect is determined by the orientation of the rotating magnet while the solenoid is activated, slightly changing the actuation velocity and ultimately the time it takes the μHammer to completely actuate (t_{SC}) by ±1 μs depending on the magnet's orientation. Since the timing of our device is sensitive to t_{SC}, my collaborators and I only mix the cells periodically (every 5 to 10 minutes) while the device is not impacting cells. Furthermore, in order to maintain a consistent magnetic field and thus t_{SC} value, we must ensure that the external mixing magnet is in the same orientation throughout the course of the experiment. We do this by placing an external bar magnet on the top edge of the alignment stage as shown in Figure A.5. This holds the mixing magnet in place while the μHammer is impacting cells. We remove this bar magnet while the mixing magnet is rotated to mix cells, and then replace it to restore the same orientation to the mixing magnet before resuming cell impact.

In addition to maintaining the same t_{SC} value throughout the course of the experiment, the bar magnet can also be used to fine-tune the closure time of the device. The orientation of the bar magnet determines the orientation of the mixing magnet, and by extension, the net

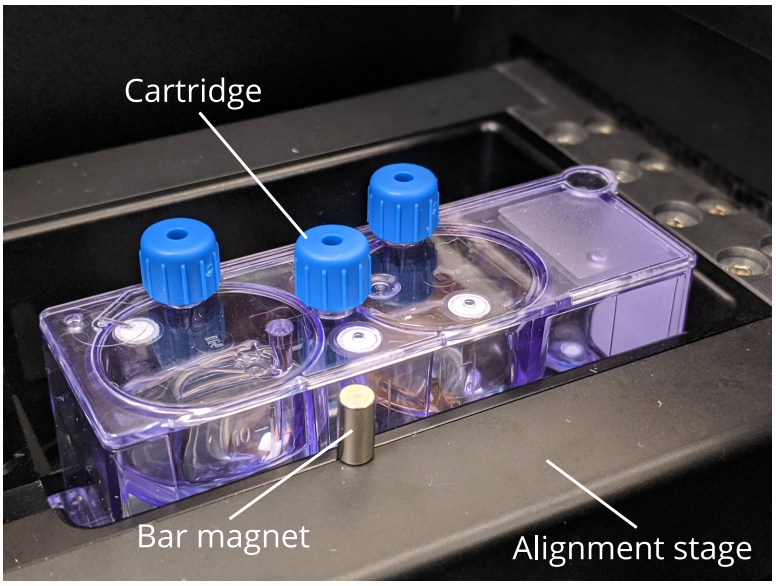

Figure A.5: µHammer cartridge loaded in the Tyto experimental system. Note the presence of the bar magnet along the edge of the alignment stage. The mixing magnet (not shown) is directly below the bar magnet inside the alignment stage.

magnetic field applied to the µHammer armature during actuation. Thus, by flipping the bar magnet, we can increase (or decrease) the t_{SC} value by up to 2 µs. This is potentially useful in cases where the device slows down over the course of an experiment as the cellular debris accumulates, allowing for the same actuation velocity and timing settings throughout the course of the experiment.

E. Statistics

All tests of statistical significance and associated *p* values in Chapter 5 were determined by one-way ANOVA with MATLAB R2015B. All linear fits and associated parameter uncertainties in Chapters 3 and 5 were determined with a Levenberg-Marquardt optimization algorithm in MATLAB R2015B.

All statistical analysis in Chapters 4 and 6 was performed with GraphPad Prism (version 8.4.1). Where indicated, Savitsky-Golay smoothing was applied using a sixth-order

polynomial. No smoothing or other statistical treatment was applied to datasets reporting quantitative values. Comparisons of 3 or more groups were performed via two-way ANOVA with Tukey's multiple comparisons test. Comparisons of two groups were performed via unpaired *t*-test, $\alpha = 0.05$.